

POLITECNICO DI TORINO

Master of Science's Degree in Biomedical Engineering



**Politecnico
di Torino**

Master of Science's Degree Thesis

**Tracking the Body Center of Mass during
simulated daily activities: a sensor fusion
approach with barometric and inertial data**

Supervisors

Prof. Andrea Cereatti

Ing. Daniele Fortunato

Ing. Paolo Tasca

Candidate

Alessandra AUDISIO

July 2024

Abstract

Monitoring the body's center of mass (BCoM) during real-world activities is vital in biomechanics and rehabilitation. It helps identify musculoskeletal disorders, assess energy use, and evaluate balance and mobility. An inertial measurement unit (IMU) can measure vertical BCoM movement by integrating accelerometer data, but this method can be inaccurate over long periods due to accelerometer biases and initial assumptions. To address these issues, this thesis integrates a barometer, traditionally used as an altimeter in avionics, into a wearable multi-sensor system that includes an IMU. The barometer is incorporated at both the hardware and firmware levels, and its readings are fused with the IMU data using sensor fusion techniques. This innovative approach aims to develop and validate methods for accurately estimating vertical displacement in individuals. Twenty healthy subjects participated in two trials mimicking daily life in a laboratory setting. Politecnico di Torino's ethical committee approved the study (Prot. 27213/2024). Tasks included Sit to Stand (StS) at normal and slower speeds to simulate mobility issues, lying on a mattress, going up and down the stairs, and squatting. Subjects wore the wearable system on their lower back. Stereophotogrammetry (SP) was used as a reference. BCoM displacement reconstruction involved two steps. First, transitions were identified through the first derivative of the barometric signal to locate the start and end of StS, lying, stairs, and squatting. Second, height changes during transitions were estimated using four methods: barometer alone (BAR), accelerometer alone (ACC), and combined barometer and accelerometer with a linear (LKF) or extended Kalman filter (EKF). Transitions are crucial as they mark points where vertical velocity is supposed to be null, facilitating the integration of accelerometer data. Height is considered constant between transitions, simplifying the process. Transitions detection was evaluated using the F1-score, sensitivity, and measuring delay relative to SP for correctly identified transitions. Height reconstruction was assessed via Root Mean Square Error (RMSE) over the entire trial and absolute deviation during transitions. An average F1-score of 90% was observed for transition detection, with a sensitivity of 99% for transitions associated with StS, slow StS, and 100% for lying. Transitions were detected with a mean delay of 12 ms. For height reconstruction, the RMSE values (average \pm standard deviation) were (8 \pm 3) cm for BAR, (19 \pm 12) cm for LKF, and (33 \pm 19) cm for both ACC and EKF. To evaluate whether the errors were influenced by transition types, techniques, tests, and subjects, reconstructed height error distributions within each group were statistically compared. Results indicated significant differences between techniques and transition types. However, no significant differences were observed between tests and subjects for each

method. The derivative method performed well on StS and lying but poorly on stairs and squats. BAR provided the most accurate reconstruction because transitions were identified with the barometric signal, making it essential to determine these integration intervals with the accelerometer to enhance sensor fusion accuracy. In conclusion, integrating the barometer and IMU shows potential for accurately measuring height changes, benefiting biomechanical analysis and energy consumption assessment, and enhancing the understanding and evaluation of human movement in real-world settings.

Acknowledgements

Ringrazio il Prof. Andrea Cereatti per avermi inserito in questo progetto così stimolante, per la sua disponibilità e i suggerimenti che han permesso di migliorare la mia formazione.

Ringrazio i miei tutor, Daniele Fortunato e Paolo Tasca, per avermi seguito in ogni passo della tesi e per essere stati presenti tutti i giorni per qualsiasi domanda o dubbio. Lavorare a stretto contatto, unendo le diverse competenze ha permesso di creare un ambiente stimolante e, non meno importante, sereno.

Ringrazio anche il “DET primo piano”, in particolare Stefano, Marco, Diletta e Rachele per aver contribuito a questo lavoro, aiutandomi, sopportandomi o semplicemente interessandosi.

Infine ringrazio Gianfranco Albis e tutti i tecnici, per avermi accolta nei loro spazi e per avermi fatta sentire parte del Dipartimento, raccontandomi le storie di decenni di esperienza.

Contents

1. Introduction	13
1.1 Aim of the thesis.....	13
1.2 Novelty of the study	13
1.3 Outline.....	14
2. Background	15
2.1 Importance of tracking the center of mass	15
2.1.1 Basic notions.....	15
2.1.2 Applications.....	17
2.2 Instrumented CoM tracking.....	21
2.2.1 Lab-based equipment.....	21
2.2.2 Wearable equipment	24
2.2.2.1 Magneto-Inertial Measurement Units	25
2.2.2.2 Barometers	30
2.3 CoM tracking with wearable devices	36
2.3.1 Activity recognition.....	36
2.3.2 Vertical displacement	39
3. Experimental setup and protocol	45
3.1 Preliminary tests	46
3.1.1 Comparison with commercial sensor.....	46
3.1.1.1 XSens	46
3.1.1.2 Panoramic Digital Health.....	48
3.1.1.3 Muse v3.....	51
3.1.2 Determination of the firmware parameters for BMP390.....	53
3.1.3 Characterization of BMP390	55
3.2 Experimental setup.....	65
3.2.1 The INDIP System.....	65
3.2.2 Vicon reference system.....	67
3.3 Experimental protocol	67
3.3.1 Minimum Sample Size and Demonstration of Achievability of Results.....	67
3.3.2 Tests.....	68

3.3.3 Request for ethical committee evaluation.....	72
4. Methods.....	74
4.1 Overview	74
4.2 Single device or double devices set-up	75
4.3 Barometric signal	78
4.4 Algorithms for the detection of transitions.....	80
4.4.1 Method based on derivatives	81
4.4.2 Manual labelling of stereophotogrammetric signal	84
4.4.3 Performance evaluation	85
4.5 Algorithms for the tracking of the vertical trajectory of CoM.....	88
4.5.1 Single-baro approach.....	89
4.5.2 Dual-baro approach	93
4.5.3 IMU-based approach	93
4.5.3 Sensor fusion approach.....	96
4.5.4.1 Kalman filter	98
4.5.4.2 Improved Kalman filter (Sabatini filter)	98
4.5.5 Performance evaluation	99
4.6 Testing procedure	102
4.6.1 Detection of transitions.....	103
4.6.2 Tracking of the vertical trajectory of CoM.....	103
5. Results	105
5.1 Detection of transitions	105
5.2 Tracking of the vertical trajectory of the CoM.....	108
5.3 Testing	121
5.3.1 Detection of transitions.....	121
5.3.2 Tracking of the vertical trajectory of CoM.....	122
6. Discussion.....	131
6.1 Method based on derivative	131
6.2 Tracking of the vertical trajectory of the CoM.....	132
7. Conclusion	135

1. Introduction

1.1 Aim of the thesis

The ability to move the Body Center of Mass (BCoM) is crucial for daily activities, and its analysis is vital in biomechanics and rehabilitation. It plays a key role in identifying musculoskeletal disorders, gauging motor energy expenditure, and assessing balance and mobility. For older adults or those with impairments, managing the BCoM during tasks like sitting, standing, or stair climbing presents significant cognitive and motor challenges.

The use of miniaturized wearable sensors, combined with advanced mathematical models, allows for the precise tracking of mobility variations in real-world settings over extended periods. However, robust algorithms that correlate sensor data with human movement biomechanics are needed to extract meaningful mobility metrics.

This study aims to develop and validate methods for accurately estimating the vertical displacement of the BCoM in healthy individuals during daily life conditions, simulated in a laboratory setting.

To this purpose, advanced wearable sensors technologies are employed, including barometric sensors and magneto-inertial units strategically placed on the feet and pelvis.

The primary goal is to prove that data from high-resolution barometric sensors, when meticulously processed, can reliably predict vertical BCoM movements, using the initial position as a baseline. Both single and dual-sensor systems provide valuable insights and the dual setup expected to effectively reduce noise in barometric signals.

The secondary goal is to evaluate the integration of magneto-inertial data with barometric readings through advanced sensor fusion algorithms and assess whether it significantly enhances estimation accuracy over using barometric data alone.

1.2 Novelty of the study

The present thesis describes a novel approach to the estimation of the BCoM of healthy subjects by analyzing signals recorded by wearable barometric and magneto-inertial sensors. The study hold two major aspects of innovation.

The first one involves the original application of barometric sensors for human movement analysis. While barometers are typically used as altimeters in avionics, this study utilizes them to track slight movements of the subjects' center of mass (CoM). Although these sensors can provide

direct altitude measurements, they are significantly affected by environmental and stochastic factors such as partial pressure changes, air movements, temperature, and humidity. These factors introduce noise and slow pressure drifts in raw barometric traces, resulting in a low signal-to-noise ratio. Also, converting pressure data to altitude can result in measurement errors that can amount to several meters, if the underlying assumptions do not accurately reflect the actual conditions. To overcome these limitations and improve the reliability of CoM displacement estimations from barometric data—potentially integrated with magneto-inertial data—specific methods must be developed to compensate for environmental influences and enhance the signal quality related to BCoM height variations. This enhancement is critical for precise movement analysis.

The second aspect of innovation pertains to the advanced application of the sensors beyond traditional uses. Wearable sensors typically monitor transitions between different states such as sitting, standing, lying down, or moving up and down stairs. This study aims to expand their application by continuously tracking BCoM height variations over time, thereby providing more comprehensive insights into an individual's motor control and energy expenditure during various movements.

1.3 Outline

The thesis is organized as follows:

Chapter 1 (current chapter) introduces the thesis topic, outlining the objectives and the innovative factors it presents. Finally, the general outline of the thesis is described.

Chapter 2 covers the mathematical and anatomical background related to the CoM, as well as exploring the various applications that leverage CoM analysis. Following this, the chapter reviews the methods used to evaluate CoM movement, encompassing both laboratory-based techniques and those utilizing wearable sensors. Special attention is given to a literature review on the use of barometric and inertial sensors for activity classification and the analysis of vertical CoM displacement.

Chapter 3 provides information regarding the preliminary tests conducted for the selection of the barometric sensor, its initial configuration at the firmware level, and subsequent characterization. Additionally, it includes a comparison of the selected barometer with other two commercially available barometers. Finally, the chapter describes both the experimental setup and the experimental protocol. The former describes the sensors and instrumentation used in the study, while the latter provides details on the subjects involved in the research and the tests performed.

It also includes information about the request for the study's evaluation by the ethics committee of the Politecnico di Torino (protocol number: 27213).

Chapter 4 focuses on the description of the developed methods and algorithms. In particular, it analyzes the processing of barometric and inertial signals. This is followed by the algorithms developed to reconstruct the vertical trajectory of the CoM. The chapter concludes with a description of the performance evaluation criteria and the statistical analysis.

Chapter 5 presents the results obtained from the implemented methods.

Chapter 6 displays the results obtained with the implemented methods.

Chapter 7 provides a critical analysis of the results presented in Chapter 6.

2. Background

2.1 Importance of tracking the center of mass

2.1.1 Basic notions

The centre of mass is a fundamental concept in physics and biomechanics that represents the average position of mass in an object or system. It is the point at which the total mass of an object or system can be considered to be concentrated, for purposes of analysis under external forces [1].

For simple rigid objects with uniform density, the centre of mass is located at the centroid. For example, the centre of mass of a uniform disc shape would be at its centre. Sometimes the centre of mass doesn't fall anywhere on the object: the centre of mass of a ring is again located at its centre, where there isn't any material (Fig.1).

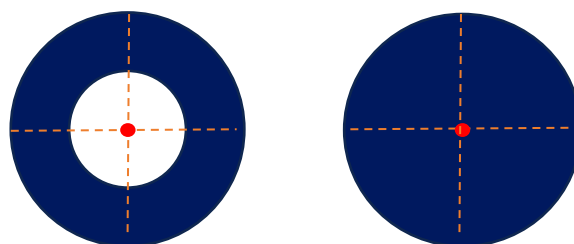


Fig. 1: Examples of CoM of a ring and of a disk, marked by a red circle, corresponding to their geometric centres.

The CoM can be defined mathematically as the average mass weighted by position of all the elements comprising the object or system.

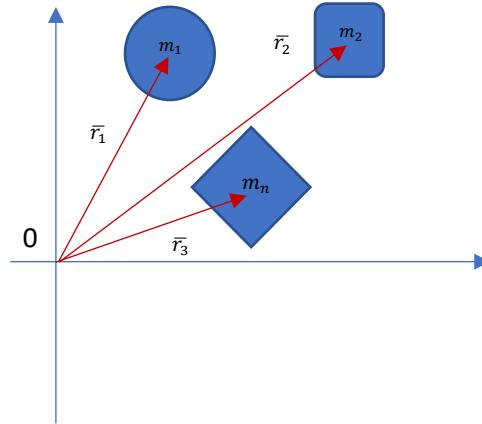


Fig. 2: Coordinate system containing m_n masses, whose relative positions in the system are indicated by the vectors \bar{r}_n .

For a system of discrete particles or objects (Fig.2), it can be calculated using (1):

$$COM = \frac{m_1 \cdot \bar{r}_1 + m_2 \cdot \bar{r}_2 + \dots + m_n \cdot \bar{r}_n}{m_1 + m_2 + \dots + m_n} \quad (1)$$

where m_1, m_2, \dots, m_n are the masses of the individual particles or objects;

$\bar{r}_1, \bar{r}_2, \dots, \bar{r}_n$ are their respective positions relative to a chosen coordinate system.

For continuous objects with a mass distribution, such as a solid body or a fluid, the CoM can be calculated through integration over the volume or mass distribution.

The CoM is also the point where the net force acting on the object can be considered to act [1]. In physics this assumption is fundamental because it streamlines the way motion is analysed. When external forces such as gravity or friction act on an object, the movement of the object can often be effectively understood by focusing on the motion of its CoM alone. This approach reduces complex systems to simpler models, making it easier to predict and analyse their behaviour under different conditions.

The anatomical definition of CoM in human physiology refers to the hypothetical point within the body where the entire mass of the body is considered to be concentrated [2]. In biomechanics and

human movement analysis, the CoM plays a crucial role in understanding posture, balance, and movement dynamics.

In biomechanical terms, the anatomical CoM is typically located around the lower end of the spine near the top of the pelvis (Fig.3), because a significant portion of the body's mass is concentrated in the trunk and lower body, particularly in the pelvis and hips. However, its precise location can vary from person to person and can shift depending on body position, movement, or changes in body composition. Understanding the anatomical location of the CoM is essential for various applications in sports science, rehabilitation, and ergonomics [3]. It provides valuable insights into human movement patterns, stability, and balance, helping researchers, clinicians, and athletes to optimize performance and prevent injuries.

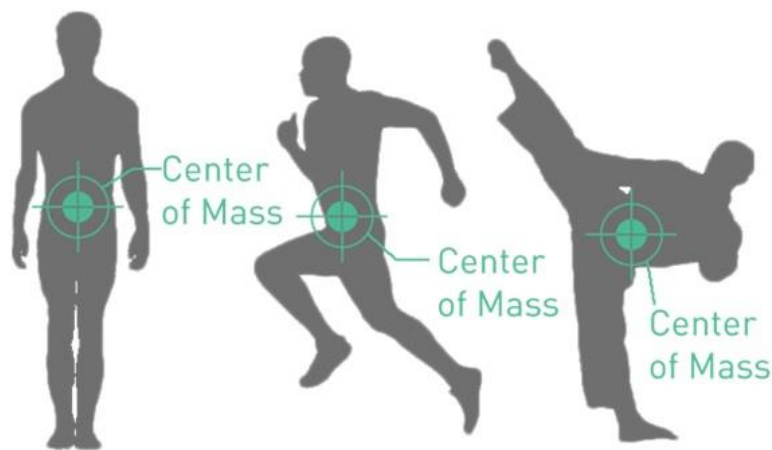


Fig. 3: Anatomical position of the center of mass, usually located around the lower end of the spine near the top of the pelvis, of a subject performing various activities [1].

2.1.2 Applications

The ability to move, specifically to shift the CoM from one point to another, is fundamental for performing daily activities. Analyzing CoM is vital in biomechanics and rehabilitation, as it aids in detecting musculoskeletal disorders, measuring motor energy expenditure, and assessing an individual's balance and mobility. In particular, its dynamic evaluation is crucial across various fields, including ergonomics, sports, and clinical practice, due to its role in quantifying risky imbalance and postural impairments [3]. In balanced conditions, postural control is maintained through both active and passive mechanisms, utilizing somatosensory feedback to ensure an upright stance. This allows for effective counteraction of both predictable and unpredictable perturbations by making real-time adjustments to CoM dynamics. As balance involves continual compensation for gravity and external disturbances, the CoM's acceleration varies constantly in

three-dimensional space to prevent falls. In static scenarios, falls occur when the CoM extends beyond the Base of Support —the area under the points of contact with the supporting surface (Fig.4) [4].

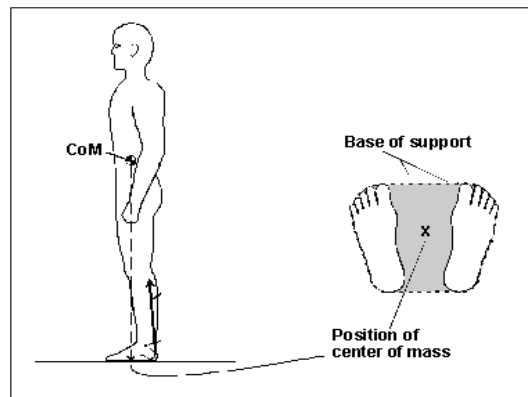


Fig. 4: The image shows a subject in static conditions, highlighting the anatomical position of the center of mass and its position within the base of support [43].

Thus, the estimation of the displacement of CoM of a subject during the execution of a motor exercise is interesting for the analysis of human movement, as it allows characterizing the overall trajectory and making comparative evaluations on motor ability.

Additionally, changes in the CoM displacement offer valuable information on the variations in potential (and kinetic, when CoM velocity is measured) energy associated with a task [5]. These assessments provide crucial insights also into functional independence and the effectiveness of rehabilitation programs for conditions like stroke, Parkinson's disease, and multiple sclerosis [6] [7]. Everyday tasks that normally require little energy (Fig.5) can become challenging for these individuals. Studies indicate that a significant portion of stroke patients experience mobility issues such as balance instability, walking difficulties, and trouble transitioning between positions like lying down, standing, and sitting [8].



Fig. 5: Sitting and standing are common everyday tasks involving a vertical displacement of the CoM [44].

As the population ages, maintaining a healthy mental and physical lifestyle becomes increasingly important for quality of life. People with motor degenerative diseases often face mobility limitations, which can exacerbate physical and mental decline associated with aging. Loss of mobility manifests in altered gait and a higher risk of falls, making systematic monitoring and evaluation of mobility essential for improving life quality for older adults and those with motor degenerative diseases [7]. Older adults often face mobility restrictions due to muscle mass loss and joint pain, which decrease strength and range of motion, limiting their ability to perform various movements. These limitations pose significant risks, as they can lead to falls that cause injuries, fractures, and even death. Falls are the leading cause of injury-related limitations in the elderly, resulting in personal, social, and economic challenges. Approximately 30% of people over 65 who live in the community fall annually, with falls accounting for 40% of injury-related deaths and 20-30% of severe injuries leading to fractures [9].

Therefore, it is essential to evaluate mobility both in clinical settings and at home to monitor and enhance the quality of life for older adults and individuals with motor degenerative diseases.

Two common tests are used by clinicians to assess motor ability: Timed Up and Go (TUG) test and the Sit to Stand (STS) test [9].

Many physically demanding tasks throughout the day begin with the individual sitting and

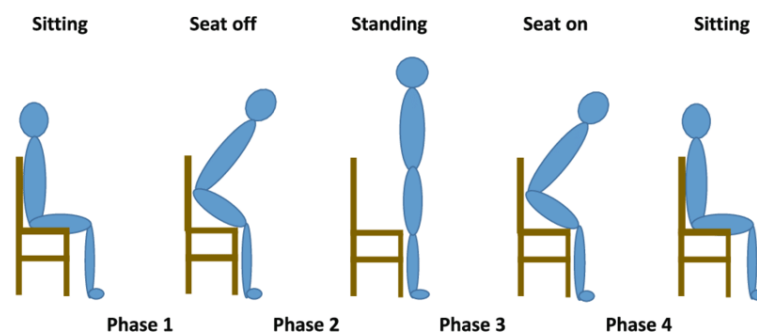


Fig. 6: Sit-to-stand and stand-to-sit movement [45].

needing to stand up to perform another activity. This lifting movement (Fig.6) is called “sit-to-stand”.

To successfully carry out this movement, the individual requires strength and body coordination. People with pathologies often struggle with balance and performing the STS movement successfully is more challenging. The STS test is commonly used to assess the level of mobility of the individual and to estimate the ability to get up from a sitting position to reach the standing position. Performing this test helps improve human movement and allows physicians to define and indicate therapy movements for each individual. This test is considered a viable method to

determine the loss of balance.

Another possibility is the five times sit-to-stand test (5STS), which has been associated with postural balance disorders and cognitive function. A recent review estimated that the average number of daily STS movements ranges from 33 to 71, with a minimum of 45 for most groups except those with conditions like congestive heart failure or those in hospital settings [10]. Individuals performing fewer than 45 daily STSs may benefit from additional intentional repetitions to address potential deficits in their daily activities.

The Timed Up and Go (TUG) test, developed in 1991 as a modified and timed version of the Get Up and Go test, enables professionals to estimate the risk of falling in older adults [9]. This test measures the time taken to perform a series of movements: getting up from a chair, walking three meters, turning around, walking back, and sitting down again (Fig.7).

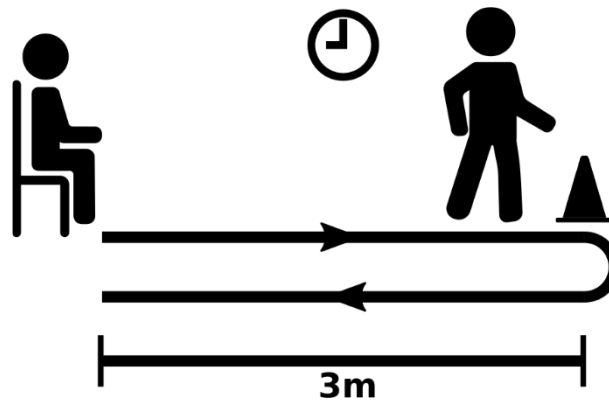


Fig. 7: Schematic overview of the TUG test, consisting of five main phases: i) getting up from a chair, ii) walking three meters, iii) turning around, iv) walking back, and v) sitting down again [46].

The test begins when the therapist says "Go" and starts the stopwatch. The time recorded is the TUG score. Typically, a practice run is followed by two timed tests, with the average time of the two tests serving as the final score. The TUG test is a comprehensive measure of functional mobility, encompassing transfer tasks (standing up and sitting down), walking, and turning, while incorporating neuromuscular components such as power, balance, and coordination [9]. A cutoff level of 13.5 seconds is generally used, with an overall prediction rate of 90% for fall risk. The test effectively distinguishes fallers from non-fallers, showing that non-fallers perform the TUG test significantly faster [9].

2.2 Instrumented CoM tracking

2.2.1 Lab-based equipment

Traditionally, the measurement and analysis of the CoM can be conducted within a controlled laboratory setting using sophisticated equipment. Among the most effective tools for this purpose are optoelectronic systems, video-based systems and force platforms.

Optoelectronic system

Optoelectronic systems, also known as stereophotogrammetry, are considered the gold standard in motion analysis due to their ability to capture detailed movements of the whole body, intricate joint kinematics, and relative motions between joints [11]. Typically, optoelectronic systems are equipped with eight to twelve cameras that are strategically placed either on laboratory walls—common in gait analysis laboratory settings—or on mobile stands, to maximize coverage of the laboratory space within the cameras' detection range (Fig.8).

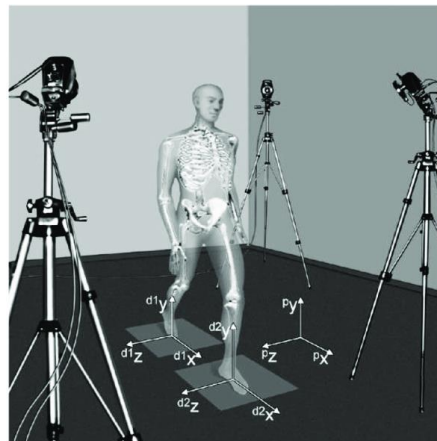


Fig. 8: Motion analysis using a stereophotogrammetric system. The cameras are positioned to cover the volume of the laboratory [47].

At the core of the stereophotogrammetric setup are markers and cameras. The markers, which can vary in shape and size according to the body segment they are attached to, are carefully placed following specific protocols [12] depending on the target body segments. Two main types of markers are typically employed: active markers, which are equipped with their own light sources powered by a device carried in a backpack, and passive markers, which are covered with a reflective material to catch the camera's light. The cameras are outfitted with a ring of infrared LEDs to consistently illuminate these passive markers, ensuring their visibility across a range of lighting conditions.

The process of motion capture with this system unfolds through several stages. Initially, camera

calibration is necessary to ensure the accuracy of the 3D trajectories reconstruction of the markers. This involves capturing the positions of markers mounted on a geometrically predefined structure. Once the cameras are calibrated, the markers are placed on the subject at protocol-defined landmark points, a procedure that can last several minutes to an hour depending on the complexity of the setup and the number of markers used.

During image acquisition, each camera captures images of the markers as clusters of white dots within its field of vision, depending on the subject's position within the lab. The system collects these 2D images and uses them to reconstruct the 3D positions of the markers. The matching and tracking stage follow, where each marker is named and associated to ensure their correct positioning in 3D space. This leads to the alignment of all markers within a shared coordinate system, which is essential for estimating local reference frames for any desired body segment.

The output of the acquisition with a stereophotogrammetry system includes the trajectories of markers located on the subject, from which further metrics such as joint kinematics, velocities, and accelerations are derived. These metrics provide crucial data that can enhance research and clinical applications, offering a comprehensive view of motion that is instrumental in advancing our understanding of human biomechanics.

Video based system

Recent advancements in markerless motion capture (MMC) technology have demonstrated significant potential for tracking the CoM in various applications, including sports and rehabilitation [13]. Studies have shown that markerless systems, such as the combination of the OpenPose software and Microsoft Kinect, can estimate CoM positions and velocities accurately when combined with advanced signal processing techniques like Kalman smoothing [14]. These systems offer the advantage of capturing natural movements without the constraints and complexity of traditional marker-based methods. MMC technology is reliable for measuring joint angles and body movements, though its application in clinical settings is still in the early stages and requires further validation across diverse patient populations [15].

In the field of rehabilitation, MMC systems have shown promise as non-invasive and cost-effective solutions for monitoring motor functions in patients with neurological disorders, post-surgical oncology patients, and children with cerebral palsy [15]. Additionally, in sports science, MMC technology has been applied to monitor athletes' CoM during dynamic activities, such as

sprinting [14].

For example, OpenPose has been used to track CoM positions and velocities during linear sprinting, demonstrating that while raw data contains significant errors, these can be mitigated with signal processing techniques [14]. A crucial aspect of MMC technology is the reconstruction of the body skeleton, which involves identifying and tracking key points on the body to create a digital representation of the subject's movement (Fig.9). This digital skeleton allows for precise calculation of the CoM and other kinematic parameters.

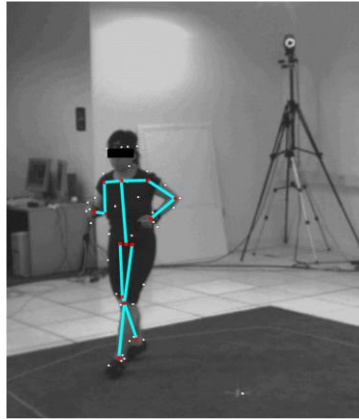


Fig. 9: Motion analysis using a markerless system. The figure highlights the subject's skeleton in blue, to identify and track key points on the body and create a digital representation of the subject's movement [48].

In conclusion, markerless motion capture systems have the potential to revolutionize motion analysis by providing accurate, non-invasive, and cost-effective data in both clinical and sports environments. However, for tracking the CoM, in relation to wearable sensors, they are confined to a restricted space and do not permit continuous monitoring.

Force platform

Tracking the CoM using a force platform is a widely used method in balance assessment and biomechanics research [13]. A force platform measures the ground reaction forces exerted by the body, providing data on the center of pressure (CoP).

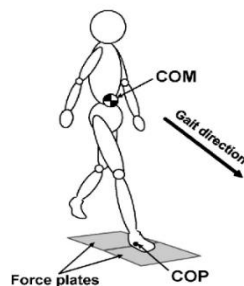


Fig. 10: Subject positioned on a force plate [49]. The CoP and CoM are highlighted.

The primary methods for CoM estimation with a force platform include integrating horizontal acceleration, filtering COP data, and using equations of motion from inverted pendulum models. These methods, while useful, vary in accuracy and complexity. For instance, the integration method struggles with precision due to difficulties in measuring horizontal forces accurately, and the COP filtering method may not fully differentiate between COP and CoM. Inverted pendulum models, whether simple or complex, offer varying degrees of accuracy based on the degrees of freedom considered and the specific motions being analyzed [13][16].

Recent advancements combine force platforms with inertial measurement units (IMUs) to enhance the accuracy of COM tracking. This hybrid approach allows for real-time estimation of COM displacement and velocity, providing valuable feedback for both clinical and research applications. Such methods are particularly beneficial for assessing balance in populations at risk of falls, such as the elderly, and for evaluating postural control in conditions like stroke and Parkinson's disease [13].

2.2.2 Wearable equipment

In clinical settings, postural impairments associated with aging or neuromuscular disorders are evaluated using kinematic and electromyographic analyses employing technologies like stereophotogrammetry and electromyography (EMG). Traditional instruments, however, face challenges such as high costs, limited working spaces, and the need for expert operation [3]. These limitations drive the development of new methods that utilize fewer sensors to ensure high accuracy and usability. The use of a single inertial sensor for postural control assessments offers quicker setup and application in diverse environments, enhancing the assessment of biomechanical risks and improving performance monitoring in sports and health care settings [3]. The use of one inertial sensor, particularly at the L5 vertebra, provides sensitive and reliable measurements for CoM assessment. Various methods have been explored for measuring CoM displacement in three-dimensional space, including the strapdown integration method and inertial sensor networks. The inertial sensor networks estimate CoM dynamics through a biomechanical model incorporating multiple sensors along the kinematic chain, offering a detailed analysis of CoM displacement across different body segments. Despite high interest in wearable sensors for dynamic CoM assessments during activities like walking, running, challenges remain in measuring CoM trajectories during static or postural tasks due to smaller oscillations and higher estimation errors [3].

2.2.2.1 Magneto-Inertial Measurement Units

The advent of miniaturized wearable Magneto-Inertial Measurement Units (MIMUs), which integrate 3D accelerometers, gyroscopes, and magnetometers, has revolutionized the functional assessment of motor functions in medicine, sports, and ergonomics. These systems, available as multisensory platforms (e.g., Dot by Movella) or single Inertial Measurement Units devices, are lightweight, compact, and cost-effective. Advances in textile technology have further enhanced these systems by enabling the integration of sensors into clothing, creating tensorized garments [17].

Wearable health systems utilize IMUs to measure, monitor, and evaluate various biomedical parameters from the human body. For gait analysis, IMUs can monitor events such as falls and track the real-time trajectory of anatomical segments, providing detailed kinematic parameters of the gait cycle [17]. These features make IMUs invaluable for patients, caregivers, and clinicians, as they offer user-friendly, outdoor-capable, and long-term monitoring solutions without complex calibration processes. Such systems can objectively and quantitatively assess gait and mobility, supporting clinical decision-making for patients with orthopaedic or neurologic impairments making it particularly suitable for home monitoring and rehabilitation scenarios.

In particular, a single IMU placed on the pelvis allows for the estimation of vertical (VT), medial-lateral (ML), and anterior-posterior (AP) displacements of the CoM through the double integration of linear acceleration derived by the IMU. Additionally, IMUs can determine the orientation of the body segment where they are placed, based on angular velocity recorded by a gyroscope [17] [18].

A MIMU includes a triaxial accelerometer, a triaxial gyroscope, and a triaxial magnetometer.

Accelerometer

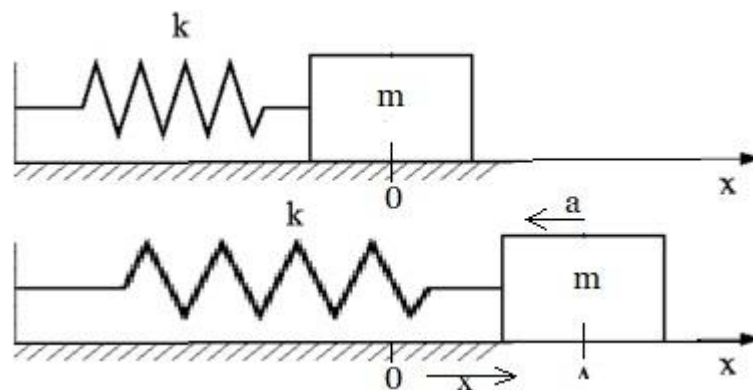


Fig. 11: Accelerometer modelled as a mass-spring system [50].

An accelerometer can be modeled as a mass-spring system (Fig.11). It measures the acceleration experienced by a mass as it moves from its resting position. The mass is subjected to an elastic force described by Hooke's law (2)

$$F = x \cdot k \quad (2)$$

where x is the displacement and k is the elastic constant of the spring.

According to Newton's second law, the inertial force is (3)

$$F = m \cdot a \quad (3)$$

Equating the elastic force to the inertial force (4):

$$m \cdot a = x \cdot k \quad (4)$$

From this, the acceleration a can be calculated, given that the mass m and the elastic constant k are known, and the internal displacement x is measurable. In MEMS accelerometers, internal displacement is typically measured through changes in capacitance between plates, which correspond to the mass-spring system's behavior (Fig.12).

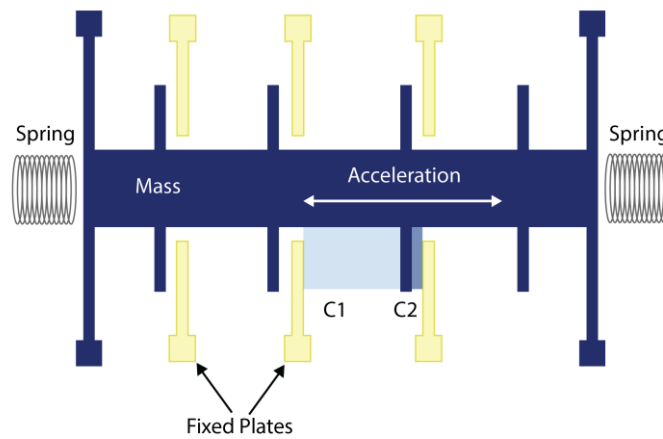


Fig. 12: MEMS accelerometers, where the displacement is typically measured through changes in capacitance between plates [51].

The sensed acceleration, a , is the vectorial sum of the linear acceleration of the body, the proper acceleration a_{proper} , and the gravity acceleration, g , (5):

$$a = a_{proper} - g \quad (5)$$

This means that accelerometers cannot directly provide displacement through double integration of the acceleration due to the gravitational component. The function of an accelerometer depends on whether it is in a static or dynamic state. In static conditions, where a_{proper} is zero, the accelerometer senses only the gravitational acceleration and can act as an inclinometer, indicating the direction of the gravity vector. In free fall, it outputs zero as both a_{proper} and g cancel each other out.

In dynamic conditions, the output reflects both gravity and the body's acceleration, making it unsuitable for determining inclination or calculating linear displacement via double integration. Therefore, it is first necessary to eliminate the contribution of gravity by transforming the acceleration into the global reference frame.

Gyroscope

Gyroscopes are devices used to measure angular velocity of an object (Fig.13).

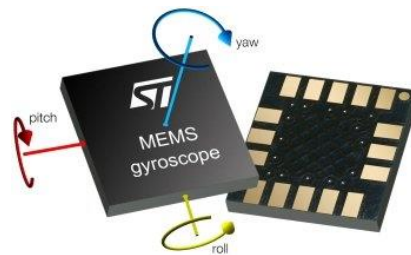


Fig. 13: MEMS gyroscope [52].

Gyroscopes manage the Coriolis effect on a vibrating framework. When an object vibrates, it tends to stay in its original vibrational plane even as its base moves. The Coriolis effect causes a secondary vibration orthogonal to the initial vibration. The Coriolis force is described by the equation (6):

$$F_{coriolis} = -2m(\omega \times v) \quad (6)$$

with m : mass;

ω : angular velocity;

v : velocity of the mass.

This effect generates a force from the vibrating object onto its base, which can be measured to gauge the rotation rate. Gyroscopes ideally respond only to rotational velocity across three axes.

By integrating the output once, angular displacement can be calculated.

However, gyroscopes can suffer from bias instabilities. The bias is the tendency of a gyroscope to output a non-zero signal when it should ideally read zero angular velocity. This constant error, or bias, affects the accuracy of the gyroscope's measurements. If it is a fixed offset that remains constant over time, it can often be corrected through calibration, while if its value is variable over time, it can cause the gyroscope drift, leading to cumulative errors in the measurement of angular displacement.

Magnetometer

The magnetometer measures the strength of the magnetic field via the Hall effect: when a current pass through a metal conductor and a magnetic field is applied perpendicular to it, a voltage difference is created across the conductor's sides due to the motion of electrons. This Hall voltage indicates the magnetic flux density.

Therefore, without magnetic interferences, such as those from ferromagnetic materials or electrical devices, the magnetometer detects only the Earth's magnetic field.

Sensor fusion enhances the performance of the accelerometer, gyroscope, and magnetometer by addressing their individual limitations to estimate the 3D orientation of a MIMU. This approach allows to remove the gravity vector from accelerometer readings, enabling the computation of linear velocity and displacement through single and double integration.

Orientation estimation involves determining the rotational relationship between the local sensor frame and the global frame. Typically, the global reference's z-axis aligns with the gravity vector, and the x-axis aligns with the Earth's magnetic north.

The accelerometer functions effectively as an inclinometer when the sensor is stationary, and the magnetometer performs well in a magnetically clean environment. They provide the initial orientation estimation of the sensor. The gyroscope's output is integrated to calculate angular displacement. However, gyroscope signals suffer from slowly varying bias, leading to unbounded drift when integrated. Sensor fusion corrects this drift by using inclination and heading data from the accelerometer and magnetometer to enhance overall accuracy.

Sensor fusion approach: the Madgwick filter

The Madgwick complementary filter [19] is a well-known algorithm for estimating the orientation of a sensor and execute the sensor fusion, specifically through the fusion of data from IMU. This filter addresses the long-term drift issues associated with gyroscopes and the sensitivity to external

disturbances of accelerometers and magnetometers.

Unlike a simple complementary filter, the Madgwick filter is nonlinear, utilizing a gradient descent approach to estimate orientation. This makes it more robust against sensor noise and inaccuracies. The filter represents orientation using quaternions, which are mathematical structures well-suited for describing 3D rotations without the singularities (gimbal lock) associated with Euler angles. A quaternion can be represented as (7):

$$q = [qw, qx, qy, qz] \quad (7)$$

qw : real part;

qx, qy, qz : imaginary parts.

The filter begins with an initial orientation estimate, usually determined by the accelerometer in a static condition, acting as an inclinometer. This initial orientation is represented as a quaternion, q .

The filter continuously receives data from the accelerometer (providing orientation relative to gravity), the gyroscope (providing angular velocity), and optionally, the magnetometer (providing orientation relative to the Earth's magnetic field).

The orientation is updated using only gyroscope data, which is quick but prone to drift over time. The gyroscope provides angular velocity, $\Omega = [\omega_x, \omega_y, \omega_z]$, which is converted into a quaternion by placing 0 as the real part $\Omega = [0, \omega_x, \omega_y, \omega_z]$.

The quaternion update can be calculated as follows (8):

$$\dot{q} = 0.5 * q \otimes \Omega \quad (8)$$

with \otimes : quaternion product;

\dot{q} : quaternion derivative;

The updated quaternion q_{new} , is then given by (9):

$$q_{new} = q + \dot{q} * \Delta t \quad (9)$$

Δt : time interval between measurements.

To correct the drift introduced by gyroscope integration, the filter employs a gradient descent algorithm to minimize the error between the gyroscope-based orientation and the orientation measured by the accelerometer and magnetometer. This error is represented by a cost function, $f(q)$. Thus, this cost function is minimized using a gradient descent algorithm, which adjusts the quaternion q to align the gyroscope-based orientation with the accelerometer-based orientation.

The cost function can be expressed as (10):

$$f(q) = q \otimes a_{measured} \otimes q^* - a_{reference} \quad (10)$$

where $a_{measured}$ is the measured acceleration;

$a_{reference}$ is the reference acceleration typically [0,0,1] representing gravity in the sensor's frame when it is at rest;

q^* is the conjugate of the quaternion.

This cost function quantifies the difference between the expected gravity vector (transformed by the current orientation) and the actual measured acceleration.

The minimum of the cost function corresponds to the situation where the error between the estimated and measured orientation is as low as possible, i.e., when the orientation estimate is closest to physical reality.

The gradient of the cost function with respect to the quaternion is calculated as (11):

$$\nabla f(q) = \left[\frac{\partial f}{\partial q_w}, \frac{\partial f}{\partial q_x}, \frac{\partial f}{\partial q_y}, \frac{\partial f}{\partial q_z} \right] \quad (11)$$

The quaternion is updated through gradient descent (12):

$$q = q - \beta * \nabla f(q) * \Delta t \quad (12)$$

with β : parameter representing the learning rate of gradient descent.

The overall equation that combines the gyroscope update and the gradient descent correction is (13):

$$q_{new} = \frac{q + (\dot{q} - \beta * \nabla f(q)) * \Delta t}{\|q + (\dot{q} - \beta * \nabla f(q)) * \Delta t\|} \quad (13)$$

Each step iteratively updates the estimated orientation to reduce error, normalizing the quaternion to maintain a unit length.

The Madgwick filter is effective because it continuously corrects for drift and sensor noise, providing a robust solution for accurate orientation estimation in IMUs.

2.2.2.2 Barometers

Pressure (P) is defined as the amount of force (F) per unit area (A) (14):

$$P = \frac{F}{A} \quad (14)$$

Atmospheric pressure results from the gravitational force acting on air molecules, decreasing with altitude due to the reduced number of air molecules at higher elevations. Air pressure is considered inversely proportional (although with a non-linear relationship) to the altitude.

Historically, barometers were used for weather forecasting and, thus, chiefly as environmental sensors. As a measurement device of ambient pressure, barometers have recently been used to measure evapotranspiration (transfer of water from land to atmosphere) in a given environment, for improving motor vehicle engine efficiency by modifying the air–fuel mixture, and for counting steps based on the slight disturbances in air pressure during body movements [20].

Thanks to the relationship between pressure and altitude, barometers are also widely used as altimeters to measure altitude [21]. Altimeters are also employed in avionics (as well as consumer electronics, such as watches) in order to provide information about how high above mean sea level is an aircraft or mountain climber located [21]. Another application is exploited by meteorologists, who typically normalize readings with the local sea pressure level in order to make predictions for the weather [21].

Since the late 1990s, the barometers have been employed for the tracking of human activities. In particular, the ubiquity of MEMS barometers in smartphones and other wearable devices makes them natural candidates as data sources for the study of human activities and for the field of human activity (and movement) recognition.

Today, barometers along with a suite of sensors like IMUs and magnetometers are used—individually or through sensor fusion—to track a wide range of human activities. However, such use of a barometer is a recent phenomenon. In the last two decades, barometers were found to improve some activity class recognition that involves change in height, such as falls or vertical movements. In some applications, as recognizing vertical displacement activity, the accelerometer has been replaced by or at least given less importance than barometers, which are more energy efficient, require less signal processing, and yield less noisy signals than IMU signals [21]. Anyway, there are several sources interfering with the change of elevation sensed by a barometric pressure, such as temperature and weather changes, or even sudden air flow [14].

A MEMS pressure sensors can be classified according to their sensing methods, that could be piezoresistive or capacitive [21].

Output voltage of the Wheatstone bridge with input voltage (V) can be written as (15):

$$V_{out} = V^+ - V^- = \left(\frac{R_3}{R_1+R_3}\right)V - \left(\frac{R_4}{R_2+R_4}\right)V = \left(\frac{R_3R_2 - R_1R_4}{(R_1+R_3)(R_2+R_4)}\right)V \quad (15)$$

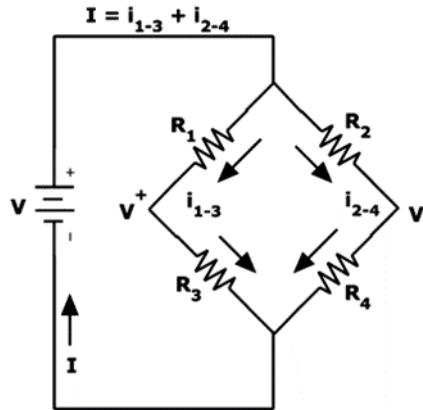


Fig. 15: Piezoresistive pressure sensor with a current and a voltage supplied to the two input terminals of the Wheatstone bridge. The resulting output voltage is $V_{out} = V^+ - V^-$.

Often, the input voltage source is replaced with a current source (I), then (16,17):

$$I = i_{1-3} + i_{2-4} = \frac{V}{R_1+R_3} + \frac{V}{R_2+R_4} = \frac{R_1+R_2+R_3+R_4}{(R_1+R_3)(R_2+R_4)} V \quad (16)$$

$$V_{out} = \frac{R_3R_2 - R_1R_4}{R_1 + R_2 + R_3 + R_4} I \quad (17)$$

The strategic placement of the piezoresistors at areas of high stress on the diaphragm is crucial for enhancing the sensor's sensitivity through maximizing the piezoresistive effect.

Capacitive Pressure Sensors

Capacitive sensors consist of a flexible diaphragm and a stationary backplate forming a parallel plate capacitor (Fig.16).

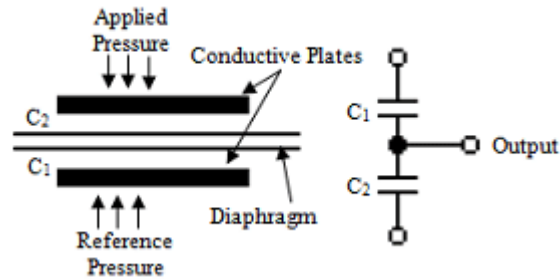


Fig. 16: Capacitive pressure sensor with flexible diaphragm and stationary backplate forming a parallel plate capacitor [54].

As diaphragm flexes in response to the external applied pressure, the distance in between plates changes and produces a variable capacitance.

When pressure is applied to the diaphragm, it deforms and moves closer or further away from the backplate. This movement changes the distance between the two plates of the capacitor. The capacitance of a parallel plate capacitor is given by the formula (18):

$$C = \frac{eA}{d} \quad (18)$$

where C : is the capacitance;

e : is the permittivity of the material between the plates;

A : is the area of the plates;

d : is the distance between the plates.

The change in capacitance is measured and converted into an electrical signal, which can be correlated to the amount of pressure applied. The smaller the distance d , the higher the capacitance, and vice versa. Also in this case, the design of the diaphragm and the material properties influence the sensitivity and resolution of the sensor. A thinner diaphragm or one made of a material with a high degree of flexibility will be more sensitive to changes in pressure. Capacitive pressure sensors are known for their high accuracy and sensitivity. They are less affected by environmental factors such as temperature and humidity compared to other types of sensors. They also benefit from having no mechanical wear components, which contributes to their long-term stability and reliability.

From pressure to altitude

The signal acquired by the barometer provides atmospheric pressure data in Pascal (Pa). When the barometer is used as an altimeter, the conversion of data from Pa to meters (m) is required. Pressure decreases exponentially with height, and for a given height z , the atmospheric pressure $P(z)$ is defined by the following formula [21] (19):

$$P(z) = P_0 * e^{-\left(\frac{z}{H}\right)} \quad (19)$$

Where:

$H = \frac{k*T}{m*g}$, pressure scale height;

P_0 : reference pressure (Pa);

$P(z)$: atmospheric pressure of a given altitude;

k (Boltzmann's Constant) = $1.38 \cdot 10^{-23} \text{ m}^2 \cdot \text{kg} \cdot \text{sec}^{-2} \cdot \text{K}^{-1}$;

T : Temperature expressed in K;

m (Average mass of atoms) = $4.76 \cdot 10^{-26} \text{ kg}$;

(22% of O_2 and 78% of N_2) $\Rightarrow (0.22 \cdot 2 \cdot 2.67 \cdot 10^{-26} \text{ Kg} + 0.78 \cdot 2 \cdot 2.3 \cdot 10^{-26} \text{ Kg})$

g (Acceleration of gravity) = 9.81 m/sec^2 ;

The following formula is used to rearrange air pressure into altitude (20):

$$\ln(P(z)) = \ln(P_0 * e^{-\left(\frac{z}{H}\right)}) \quad \text{because : } \ln(x*y) = \ln(x) + \ln(y)$$

$$\ln(P(z)) = \ln(P_0) + \ln(e^{-\left(\frac{z}{H}\right)}) \quad \text{because : } \ln(e^x) = x * \ln(e) = x * 1 = x$$

$$\ln(P(z)) - \ln(P_0) = -\frac{z}{H} \quad \text{because : } \ln(x) - \ln(y) = \ln(x/y)$$

$$z(\text{in meters}) = H * \ln(P_0) - H * \ln(P(z)) = H * \ln\left(\frac{P_0}{P(z)}\right) \quad (20)$$

In the present study the previous formula is used, where P_0 is set as the reference pressure that depends on the specific application, and the temperature could change during the trial. The

obtained altitude z is the distance between the points characterized by the pressure $P(z)$ and P_0 .

2.3 CoM tracking with wearable devices

2.3.1 Activity recognition

Recent studies have increasingly utilized barometric sensors, either alone or combined with inertial measurement units, to investigate vertical displacements and human activities recognition (HAR). Although there is a growing need to assess subjects in home environments, much of this research is still conducted in controlled settings. Sensor fusion methods combine data from different sources to enhance performance beyond what each source could achieve independently. Designing systems based on sensor fusion requires complementary sensors to mitigate the limitations of individual sensors with the strengths of others, such as combining a barometric altimeter with an Inertial Measurement Unit containing a tri-axial gyroscope and accelerometer.

One of the key areas of interest is the sit-to-stand transition, which is crucial for evaluating rehabilitative progress and assessing motor abilities. Numerous studies have focused on the detection capabilities of STS transitions. For instance, Massè et al. conducted two notable studies on post-stroke patients using a combination of a barometer and an inertial sensor placed on the trunk.

In the first study [6], a logistic regression classifier was used to detect and classify sit-to-stand and stand-to-sit transitions in 12 stroke patients, performing daily activities. The results showed that including the barometric data improved the overall correct classification rate (CCR) to 90.6%, significantly outperforming the use of inertial sensors alone, that achieved an overall CRR of 75.4%. The aim of the second study [22] was to improve the recognition of daily activities and body elevation in mobility-impaired stroke patients, in particular to classify activities such as sitting, standing, walking, lying, and estimate body elevation during activities like stair climbing. An event-driven activity classifier based on a hierarchical fuzzy inference system (H-FIS) was developed to process the data from 12 stroke patients. The results indicated that the classifier achieved a CCR of 90.4% for posture/activity detection, with significant improvements in recognizing standing activities compared to previous methods.

The barometric signal processing in these studies involved converting the barometric data to height using the barometric formula, followed by signal enhancement through sinusoidal modelling. The integration of the barometric sensor significantly improved performances.

Moncada-Torres et al. [23] investigated the optimal placement and selection of wearable sensors for classifying 16 activities of daily living (ADL) using a custom-made inertial measurement unit enhanced with a barometric pressure sensor. Subjects wore sensors on the wrists, ankles, and trunk. The study found that wrist-worn modules provided the highest classification accuracy, which was significantly improved by including altitude information from the barometer. The research highlighted that gyroscopes did not contribute significantly to classification accuracy under their scheme, suggesting potential for energy savings in long-term monitoring. The study achieved an overall classification accuracy of almost 93% through k-nearest neighbors (kNN) as classification method.

Additionally, Xie et al. [24] aimed to improve human activity recognition (HAR) using a combination of inertial sensors and barometers, employing a multi-layer classification strategy where activities were initially divided into dynamic and static categories. It was used a machine learning classifier, specifically Support Vector Machines (SVM) for pre-classification and Random Forests for detailed activity classification. The method further refined results using additional parameters and previous recognition data. This approach achieved an average recognition accuracy exceeding 96% for eight activities, including sitting, standing, lying, walking, downstairs, upstairs, running, and fall detection, demonstrating high robustness and effectiveness.

Makma et al. [25] proposed the use of relative barometric pressure sensors to enhance the accuracy of human activity detection based on a tri-axial accelerometer. In the experiment, 12 subjects wore a device with a tri-axial accelerometer and a barometric pressure sensor on their waists while performing activities like sitting, standing, walking, and lying. An additional barometric pressure sensor was placed on the wall as a reference. Activity classification was compared across three datasets: 1) acceleration data, 2) acceleration with on-body barometric pressure data, and 3) acceleration with both on-body and reference barometric pressure data. Three classifiers—KNN, Decision Tree, and Random Forest—were evaluated. The highest classification accuracy of 90.4% was achieved using the Random Forest algorithm with the combined dataset of acceleration and both barometric pressure data.

In efforts to differentiate between subjects at risk of falls and those who are not, Ejupi et al. [26] focused on developing a wavelet-based algorithm for detecting and assessing the quality of sit-to-stand movements in older people, aiming to identify fall risk. Using a wearable pendant device equipped with an accelerometer and a barometric air pressure sensor, the study evaluated 119 participants performing daily activities and standardized tests. The algorithm detected sit-to-stand movements with 93.1% sensitivity and a false positive rate of 2.9%, distinguishing between fallers

and non-fallers based on maximum acceleration, velocity, and power during the sit-to-stand movement. The wavelet transform's main advantage is its ability to identify patterns similar to the 'mother wavelet,' providing a signal representation with excellent localization in both time and frequency.

Sun et al. [27] proposed a wearable fall detection system using barometric pressure sensors and machine learning to address the challenge of detecting falls from different heights. The study involved 10 subjects simulating falls and non-fall activities. The system utilized various classifiers, including Decision Tree, k-nearest neighbors (kNN), and support-vector machine (SVM), achieving the highest accuracy of 94.3% with the linear SVM classifier. The system showed promise in accurately detecting falls and reducing false alarms compared to traditional IMU-based systems.

Pierleoni et al. [28] developed a waist-mounted fall detection system for elderly people using an Altitude and Heading Reference System (AHRS) combined with a barometric sensor. The device, integrating a 3-axis accelerometer, gyroscope, magnetometer, and barometer, provided accurate posture and altitude estimations. Tested with various fall scenarios and daily activities, the system achieved 100% sensitivity. The algorithm effectively detected falls, including those ending in a sitting position, highlighting the importance of combining multiple sensor types and efficient data fusion algorithms.

In recent years advanced versions of the TUG test, known as the instrumented TUG (iTUG), have been developed and rigorously tested in elderly populations, both with and without specific medical conditions [29]. Research has demonstrated that the iTUG, when equipped with portable inertial sensors, can effectively identify specific walking impairments in individuals with Parkinson's disease, correlating gait deficits with the severity of the condition. Previous studies have explored various aspects of the iTUG, including different technologies for enhancing TUG tools, the use of iTUG in mobile platforms, and advancements in assessing fall risks.

The primary methods for precisely and objectively measuring gait patterns are wearable inertial measurement units (IMUs) and stationary camera-based optical motion capture systems. Unlike traditional stopwatch methods, these instrumented approaches allow for detailed analysis of TUG tasks, including movements like sitting to standing, initial walking, turning, returning, and sitting back down. The iTUG provides additional performance metrics, objective assessments, and automated data management, offering significant improvements over traditional stopwatch-based TUG tests. This method supports extensive and easier long-term monitoring and shows promise for self-administration in home settings for the elderly. However, challenges such as the cost of

acquiring medically certified equipment and the need for specialized training for staff remain barriers to widespread adoption. Additionally, some kinematic metrics, like angular velocity, are not yet widely understood by healthcare professionals. Nevertheless, there is growing interest among physiotherapists, geriatricians, and other medical experts in leveraging the iTUG to enhance clinical management and intervention strategies for older patients [29].

2.3.2 Vertical displacement

Besides HAR, barometers can also be utilized to estimate vertical displacement of the sensor.

As previously mentioned, fluctuations in pressure can be unrelated to altitude, caused by unpredictable atmospheric conditions outdoors or actions like opening/closing windows or doors indoors, that make barometric altimeters inherently noisy and inaccurate.

To address these challenges, Sabatini et al. [30] employed a two-step filtering approach. Firstly, a filtering module utilizing a quaternion-based Extended Kalman Filter (EKF) estimates the altitude of the body frame using inertial sensors. This allowed the sensed specific force to be rotated into the navigation frame and compensated for gravity, yielding vertical linear acceleration. Then, a complementary filter, driven by the vertical linear acceleration and measured pressure altitude, produced estimates of height and vertical velocity.

The complementary filter is implanted as suggested in [31] (21):

$$C_{x_k} = \begin{bmatrix} x_{a_k} \\ \dot{x}_{a_k} \end{bmatrix} = \begin{bmatrix} 1 & T_s \\ 0 & 1 \end{bmatrix} = C_{x_{k-1}} + \begin{bmatrix} 1 & T_s/2 \\ 0 & 1 \end{bmatrix} K_c \cdot T_s \Delta x_{k-1} + \begin{bmatrix} T_s/2 \\ 1 \end{bmatrix} \Delta v_{k-1} \quad (21)$$

where C_{x_k} includes the vertical position and the vertical velocity;

$$\Delta x_k = x_{p_k} - x_{a_k};$$

$$\Delta v_k = T_s \ddot{x}_{a_k};$$

x_{p_k} : is the pressure altitude measured by the barometric altimeter at time $t_k = kT_s$;

\ddot{x}_{a_k} : is the vertical linear acceleration at the same time instant, after gravity compensation;

K_c , the gain of the complementary filter, is given by (22):

$$K_c = - \begin{bmatrix} \sqrt{2\sigma_w/\sigma_v} \\ \sigma_w/\sigma_v \end{bmatrix} \quad (22)$$

σ_w : standard deviation of the noise in linear acceleration $\ddot{x}_{a k}$;

σ_v : standard deviation of the noise in pressure altitude $x_{p k}$.

To address the noise and environmental influences on barometric measurements, filtering techniques were developed to condition the measured pressure altitude by removing short-term correlations caused by environmental pressure changes. The data were processed using two methods: Method A employed a 4-point moving average filter, while Method B used a 4-point moving average filter cascaded with a whitening filter (designed with a DC gain of 0.21, one pole at 1 Hz, and one zero approximately two octaves down). The experimental validation involved several tests subjecting the baro-IMU to various motion conditions. Specifically, the no-motion condition, where the sensor remained at rest to assess the effects of short-term correlated pressure fluctuations on height and vertical velocity estimation; free-fall motion, where the baro-IMU was dropped from a known height to evaluate the accuracy of tracking vertical velocity and height during free-fall; forced circular motion, characterized by uniform circular motion to test the method's performance under controlled rotational movements; and squatting, where subjects performed squatting movements to simulate typical vertical human motions and assess the method's practical applicability.

Root Mean Square (RMS) values of the differences between estimated and reference time functions were computed for each motion condition when reference data were available.

With parameter tuning, it was found that $\sigma_w=15$ mg, $\sigma_v= 30$ cm for Method A, and $\sigma_v= 15$ cm for Method B. The standard deviation of the noise σ_v for the barometer was chosen based on the filtering applied. Both σ_v and σ_w were obtained from measuring the standard deviation of the noise for the barometer and the accelerometer, respectively.

The results show a RMSE, expressed as mean value (m) \pm standard deviation (m) across 10 trials, for the no-motion condition equal to $0,4 \pm 0,15$ (Method A) and $0,08 \pm 0,03$ (Method B) while the free fall motion achieved a value equal to $0,07 \pm 0,03$ (Method A) and $0,05 \pm 0,02$ (Method B).

The last test executed was the squatting, that produced an RMSE equal to $0,86 \pm 0,39$ and $0,5 \pm 0,11$ for Method A and B, respectively. The results (height RMSE in the range 5–68 cm) indicate that the sensor fusion method, particularly with the whitening filter, significantly improves the accuracy and reliability of vertical displacement and velocity tracking in various motion conditions.

Many applications that utilize the barometer are directed towards aerospace vehicle navigation information. For instance, Yu et al. [31] proposed a multi-sensor fusion algorithm for positioning and navigation in low-speed rotorcraft used for atmospheric detection tasks. The algorithm

integrates data from an Inertial Measurement Unit (IMU), Global Positioning System (GPS), and barometric sensors, based on the Federated Kalman Filter. Results from experiments demonstrate that the fusion algorithm provides velocity and spatial position estimates closer to the actual values compared to those obtained from a single sensor.

Ensuring accurate, real-time, and consistent altitude data is crucial for the safe operation of rotorcraft. While GPS provides vertical altitude readings, its update frequency is limited; barometers offer quick altitude updates but are affected by airflow variations. Accelerometers deliver fast vertical acceleration data but accumulate errors over time. By integrating the capabilities of these sensors, sensor fusion offers a solution that combines high refresh rates with stable and precise vertical height measurements.

The fusion process for vertical height entails two stages: initially, the Kalman Filter combines accelerometer and barometer measurements to derive the initial altitude, denoted as h_0 . The second stage employs a least-squares weighted estimation method to fuse the initial altitude estimation with GPS altitude measurements. This approach compensates for the slow update rate of GPS and the environmental susceptibility of barometric measurements. The resulting RMSE for vertical height is 3.12 meters.

Another paper that exploits the fusion of inertial module, GPS and barometer to enhance the accuracy of vehicle navigation is proposed by Sokolovic et al. [32]. The integration approach was facilitated through the use of an extended Kalman filter (EKF), which was applied to mitigate the errors inherent in each individual sensor system and improve overall system accuracy. The EKF also included control signals with an adaptive function to dynamically adjust to varying sensor noise characteristics. Experimental analysis of the integrated navigation system's performance demonstrates that it consistently delivers continuous and dependable navigation solutions especially in environments where GPS data may be intermittently unavailable.

In the work by Pierleoni et al. [33], due to GPS signal limitations indoors, only an inertial module and barometer were used, excluding GPS data. To accurately extract the relevant acceleration component, orientation estimations provided by the Attitude and Heading Reference System were utilized. Specifically, Madgwick's sensor fusion algorithm was employed to derive quaternion representations of the device orientation, crucial for precise movement analysis.

The accelerometer vector, E_a , comprised both static (gravity) and dynamic (motion-induced) accelerations when the device was in motion (23):

$$E_a = E_d + E_g \quad (23)$$

Only the dynamic acceleration component, E_d , and particularly the component perpendicular to the Earth's surface (E_{dz}), was considered for the estimation of vertical displacement through double integration. This method primarily counters low-frequency noise, necessitating accurate orientation estimation to effectively isolate gravity from the acceleration vector.

Data from the accelerometer and barometer were fused using a complementary filter in a two-input system. One input contained information with high-frequency noise, subjected to low-pass filtering, while the other input, with low-frequency noise, underwent high-pass filtering. This configuration ensured that when the low-pass and high-pass filters are mathematical complements, the output effectively reconstructs the variable being estimated, subtracting the sensor noise. Assuming that $x_1 = z + n_1$ and $x_2 = z + n_2$ represent two measurements of the same signal z , where n_1 and n_2 denote the respective noise measurements, and z is the estimated signal- if n_1 predominantly consist of low-frequency noise, and n_2 predominantly high-frequency noise- the output z is expressed as (24):

$$Z(s) = G_1(s)X_1(s) + G_2(s)X_2(s) \quad (24)$$

where $G_1(s)$ represents the transfer function of a high-pass filter and $G_2(s) = 1 - G_1(s)$ denotes a low-pass filter. For altitude estimation, a complementary filter is utilized to merge altitude data from the altimeter sensor H_{baro} and vertical displacement derived from AHRS E_{dz} (25):

$$H(s) = \frac{1}{s^2} G_1(s) E_{dz}(s) + G_2(s) H_{baro}(s) \quad (25)$$

Kalman filter

The Kalman filter is an efficient and versatile algorithm for estimating the state of a linear dynamic system in the presence of noise [34]. To understand the Kalman filter, it is necessary to introduce some elements.

In particular, the state model encapsulates a mathematical representation that delineates the system's evolution over time. This can be expressed through the equation (26):

$$\mathbf{x}_{k+1} = \mathbf{A} * \mathbf{x}_k + \mathbf{B} * \mathbf{u}_k + \mathbf{w}_k \quad (26)$$

with, x_{k+1} : subsequent state

A: state transition matrix

B: control input matrix

u_k : control input vector

w_k : process noise

For systems that encompass parameters such as height, velocity, and acceleration, the state vector x is defined as (27):

$$\mathbf{x} = \begin{bmatrix} \text{height} \\ \text{velocity} \\ \text{acceleration} \end{bmatrix} = \begin{bmatrix} x \\ \dot{x} \\ \ddot{x} \end{bmatrix} \quad (27)$$

The state transition matrix, A , describes as the state evolves over time. For a system influenced by velocity v and acceleration a , the motion equations are (28,29,30):

$$x = x_0 + v * t + \frac{1}{2} * a * t^2 \quad (28)$$

$$v = v_0 + a * t \quad (30)$$

$$a = a \quad (31)$$

Consequently, matrix A is defined as (32):

$$\mathbf{A} = \begin{bmatrix} 1 & \Delta t & 0.5\Delta t^2 \\ 0 & 1 & \Delta t \\ 0 & 0 & 1 \end{bmatrix} \quad (32)$$

Δt : time between measurements

The control matrix B in a Kalman filter models how external controls or forces influence the system. In many systems, in addition to the natural evolution of the state (described by the transition matrix A), there are external controls or external forces that can change the state. These inputs are represented by matrix B and a control vector u . If acceleration is the sole external control affecting the system, B could be (33):

$$\mathbf{B} = \begin{bmatrix} 0.5\Delta t^2 \\ \Delta t \\ 1 \end{bmatrix} \quad (33)$$

This matrix maps how the control input influences the state. In this case, the control input directly affects acceleration, has a proportional impact on velocity change, and a quadratic impact on altitude alteration.

It is necessary to specify how the measurements are related to the state. For example, if the measurement is altitude detected by a barometer, it would be expressed as (34):

$$z_k = H * x_k + v_k \quad (34)$$

z_k : measurement

H : measurement matrix, which connects the state to the measurements (35)

$$H = \begin{vmatrix} 1 & 0 & 0 \\ 0 & 0 & 1 \end{vmatrix} \quad (35)$$

v_k : measurement noise

Understanding the characteristics of the process noise w_k and measurement noise v_k is also crucial. These are typically modelled as independent, normally distributed white Gaussian noises. The process begins with an initial estimation of the system state x_0 and its uncertainty, P_0 .

The Kalman filter operates in two phases: the prediction phase (based on the state model) and the measurement update phase (based on the measurements) (36,37,38,29,40).

Prediction phase

$$x_k = A * x_{k-1} + B * u_{k-1} \quad (36)$$

$$P_k = A * P_{k-1} * A^T + Q \quad (37)$$

Update phase

$$K_k = P_k * H^T * (H * P_k * H^T + R)^{-1} \quad (38)$$

$$x_k = x_k + K_k * (z_k - H * x_k) \quad (39)$$

$$P_k = (I - K_k * H) * P_k \quad (40)$$

with, K_k : Kalman gain, which minimizes the covariance

Q : covariance of the process noise

R : covariance of the measurement noise

I : identity matrix.

The Kalman gain matrix K is central to understanding how the Kalman filter optimizes state estimation. When the covariance of the measurement error, R , is minimal, suggesting near-zero values, the current measurement z_k is deemed highly reliable, diminishing the reliance on the predicted measurement $H \cdot x_k$. Conversely, when the covariance of the estimation error, P_k ,

approaches zero, the reliability of the current measurement decreases, enhancing the stability of the predicted measurement. Defining the noise covariances R and Q is crucial for the filter's performance. If these parameters are not predefined, tuning is required, typically performed off-line and possibly using another Kalman filter for optimization. The covariance R can be determined from off-line measurements to capture variance accurately, whereas Q often embodies a less deterministic nature.

The Kalman filter operates through a feedback control mechanism, continuously adjusting its estimates based on new noisy measurements. This process involves two primary sets of equations: the time update equations and the measurement update equations. The time update equations, or predictive equations, project the current state and covariance forward in time, providing prior estimates for the next step. The measurement update equations, or corrective equations, integrate new measurements to refine these estimates, resulting in improved posterior estimates. The temporal update equations can also be considered as predictive equations, while the measurement update equations can be considered as corrective equations.

The Kalman filter adeptly addresses the challenge of estimating the state of a linear, discrete-time controlled process subject to stochastic disturbances. However, in scenarios involving nonlinear processes or nonlinear relationships between measurements and the state, standard Kalman filtering may not suffice. In these cases, the Extended Kalman Filter (EKF) is employed, which adapts to nonlinearities by linearizing around the current estimates. This extension is pivotal in applications where nonlinear dynamics are prominent, making the EKF a versatile tool in advanced Kalman filtering applications.

3. Experimental setup and protocol

The objective of reconstructing the vertical trajectory of the center of mass of a subject during simulated daily activities in the laboratory is pursued through the use of barometric and inertial sensors. Specifically, the inertial module used is the one included in the INDIP wearable multi-sensor system (which will be described in detail in paragraph 3.2.1). The barometer BMP390 from Bosch has been specifically integrated in the INDIP system at both hardware and firmware levels. The Bosch barometer, encapsulated into the INDIP system within a custom plastic case (INDIP-

baro), was compared with commercial devices. Subsequently, its parameters were defined at the firmware level and, finally, it was characterized.

3.1 Preliminary tests

Algorithms for motion analysis strongly rely on the metrological accuracy of the recorded data. Therefore, preliminary tests to identify the optimal experimental setup and characterize its metrological performance were conducted before moving to the implementation of the algorithms.

3.1.1 Comparison with commercial sensor

Pressure sensors are embedded in a number of commercial devices. To evaluate the advantage of using a low-level system instead of a high-level commercial product, the performance of Bosch's BMP390 barometer was compared with those of three commercial products: MTw sensor by Movella, a wristband by Panoramic Digital Health, and the new Muse sensor by 221e.

3.1.2 XSens

The MTw by Xsens [35] is a compact and highly advanced wireless inertial measurement unit designed to capture and transmit accurate motion tracking data. It features a suite of sensors, including 3D accelerometers, gyroscopes, magnetometers, and a barometer. The device uses a wireless network protocol to transmit data to a receiving station or computer, enabling real-time monitoring and analysis of motion data without the encumbrance of wires.

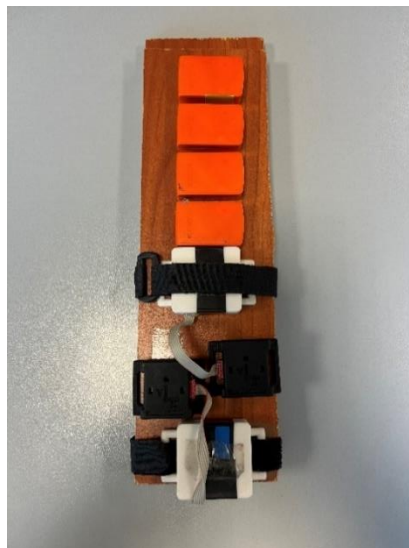


Fig. 317: Four Xsens sensors and two INDIP-BMP390 sensors were used to compare the performances. Sensors were mounted and fixed on a wooden beam, representing a rigid body, to analyze them under similar conditions.

Being a commercial product, MTws are smaller than the INDIP system, resulting in a more compact system compared to the separate IMU and barometer configuration of INDIP. For the comparison, which aimed particularly at evaluating the performance of the two barometers, four Xsens sensors and two INDIP-BMP390 sensors were used. These sensors were fixed to a wooden beam (Fig.39), to analyze performance under similar conditions.

The barometric MTw sensors sample at a frequency of 50Hz. The selected BMP390 configuration samples pressure at 25Hz, but is upsampled on board to 100Hz to match the sampling frequency of inertial data, resulting in four repeated samples every 40 ms. To compare performance, missing values in the Xsens data were removed, and samples were duplicated to also achieve a sampling frequency of 100Hz (Fig.40).

The preliminary tests involved performing three turns in place, walking down a flight of stairs, walking a few meters, and then ascending the same stairs. The initial three turns were conducted to manually synchronize the recordings of the different sensors using the vertical angular velocity signals.

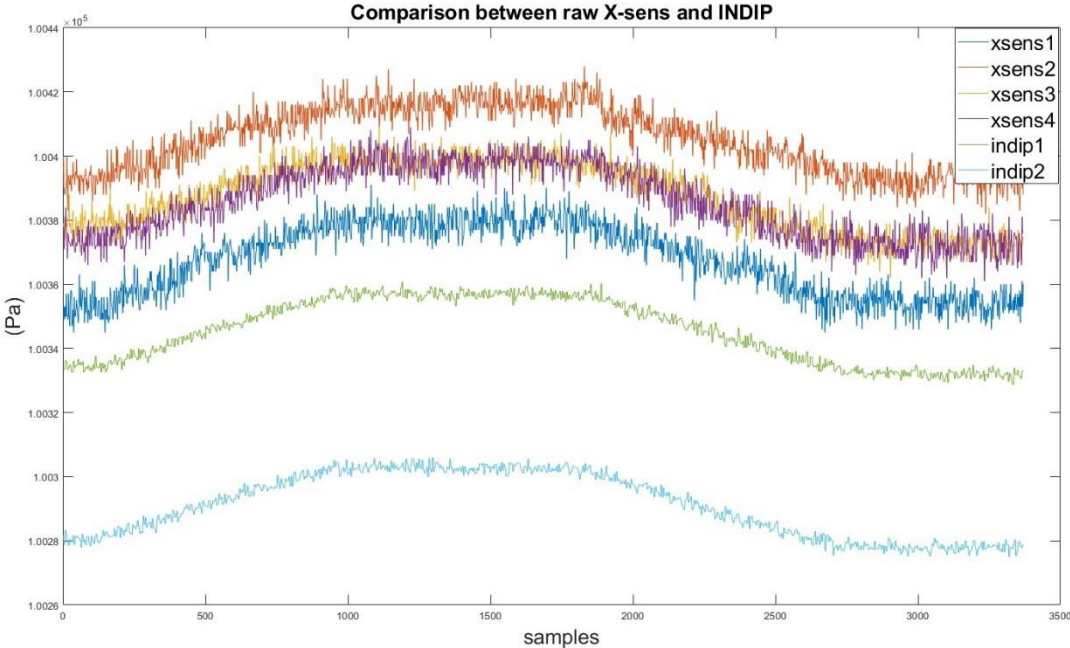


Fig. 40: Raw barometric signals from four MTw sensors and two INDIP-baro sensors.

The average Pearson correlation coefficient between the pressure signals recorded by the six sensors for all tests was 0.9211. The delay associated to the maximum cross-correlation was 0 for all the cases, meaning that the signals are in phase i.e., the sensors have similar dynamic responses. Variance was calculated on sections of the raw signals associated to constant heights, resulting in an average variance of 11.82 Pa for MTw sensors and 1.96 Pa for INDIP sensors.

To focus on the behavior of the signals during transitions, the average pressure measured by the four MTw sensors was low-pass filtered at a cutoff frequency of approximately 1Hz and compared to that of the signals recorded by the two INDIP-baro systems.

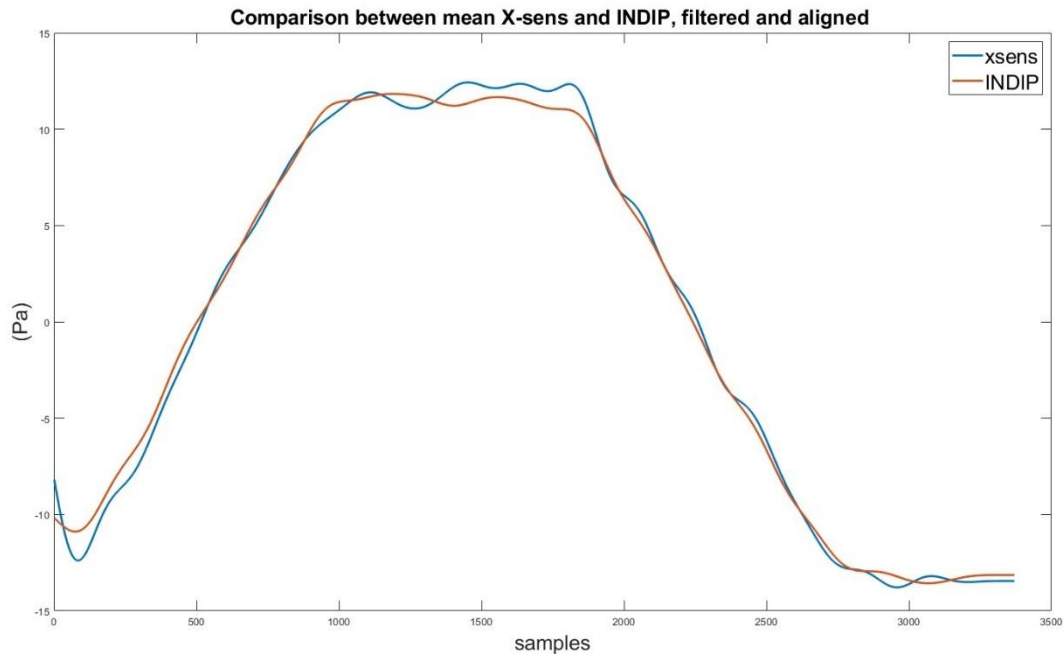


Fig. 41: The pressure signals were averaged according to sensor group (MTw or INDIP-baro) and subsequently filtered with a low-pass filter at a cutoff frequency of about 1Hz.

Finally, the Pearson correlation coefficient was recalculated, yielding an average value of 0.997 for all tests.

In conclusion, signals from INDIP and Xsens were strongly correlated and provided similar information about environmental pressure changes, although the raw signals from the INDIP system showed much smaller variance. From these preliminary tests, it appeared clear that filtering the signals may not be enough to allow the identification of individual steps taken for neither of the two sensors.

Given the great similarity between the signals recorded by INDIP-baro and MTw sensors, the two setups can be used interchangeably based on necessity and convenience.

3.1.1.2 Panoramic Digital Health

Pressure signals recorded by the integrated INDIP system with the BOSCH BMP390 barometer were compared to those recorded by a sensing wristband provided by Panoramic Digital Health

(PDH). The PDH wristband is designed to measure behaviors and functions significantly impacting patients with chronic health conditions. It can estimate sleep and activity levels, and when used in conjunction with beacon data, it provides deeper insights into patients' lives.

The PDH wristband includes a 3D accelerometer, gyroscope, magnetometer, and a barometer (specifically the LPS27HHW model from STMicroelectronics [36]). The comparison focused on the performance of the two barometers, evaluated during controlled laboratory trials performed by one young healthy participant. A trial involved a sequence of the following actions: sit-to-stand, walking, lying down, walking, and stand-to-sit. The trial was repeated six times.

To compare the pressure measurements of the two system in the same experimental condition, both the PDH wristband and the INDIP-barometer were positioned on the pelvis using a Velcro strap, and equipped with a marker for tracking vertical trajectory using the stereophotogrammetric system (Fig.42).

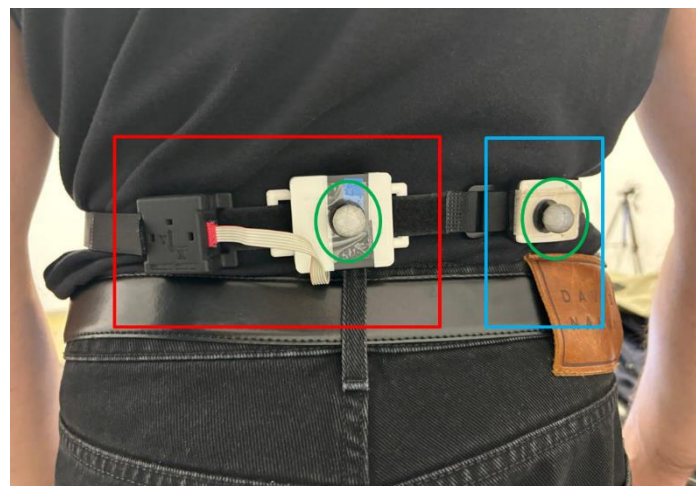


Fig. 42: PDH wristband (blue) and INDIP-barometer (red) were positioned on the pelvis at the same height to compare their performances under simulated daily activities.

The PDH inertial sensor samples at a frequency of 50 Hz, while its barometer samples at 13 Hz. To facilitate comparison, the sampling rates were first aligned to those of the INDIP system (100 Hz for the accelerometer, gyroscope, and magnetometer, and 25 Hz for the barometer). Temporal alignment of the sensors was manually achieved by performing three initial rotations.

Both barometric signals were converted to height according to (20), and low-pass filtered with a cutoff frequency of approximately 1 Hz. After removing the linear trend, the signals were aligned with the subject's known initial pelvic height.

The following images show the comparison between the signals of the two sensors and the stereophotogrammetric system (Fig.43, Fig.44, Fig.45).

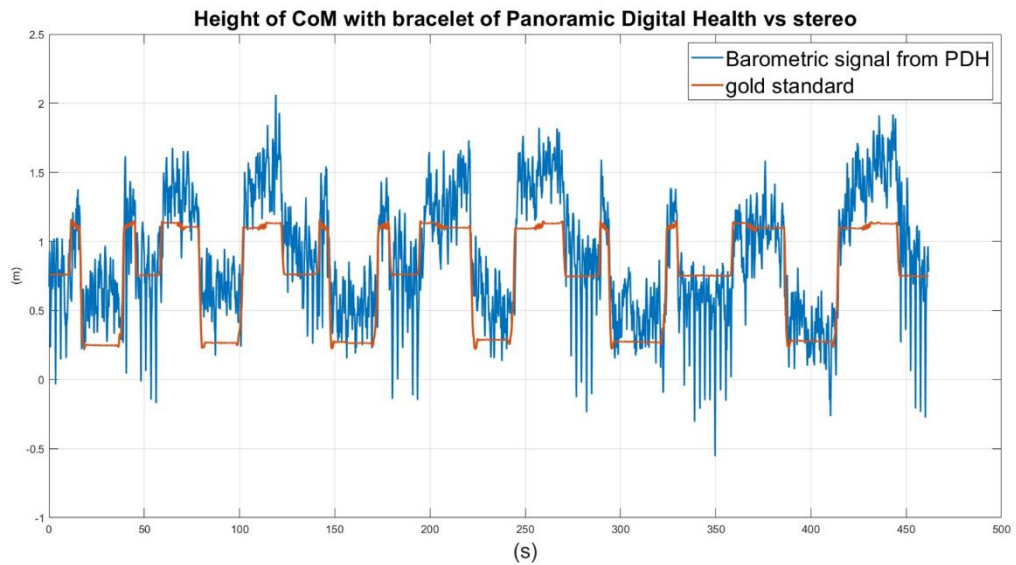


Fig. 43: Comparison of CoM displacement between reference (stereophotogrammetric signal) and PHD sensor. The barometric signal was converted to height, low pass filtered with a cutoff frequency of approximately 1 Hz, detrended, and aligned with the initial pelvic height of the subject.

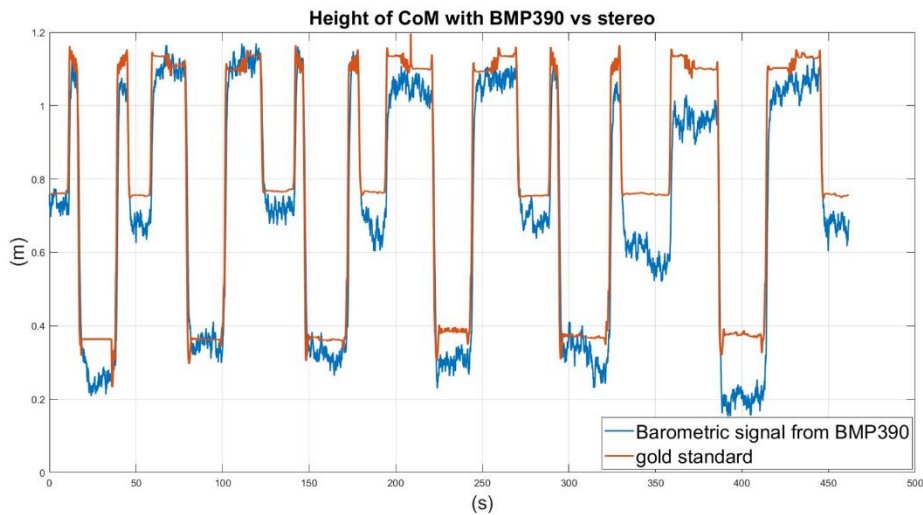


Fig. 44: Comparison of CoM displacement between reference (stereophotogrammetric signal) and INDIP-barometer. The barometric signal was converted to height, low-pass filtered with a cutoff frequency of approximately 1 Hz, detrended, and aligned with the initial pelvic height of the subject sensor.

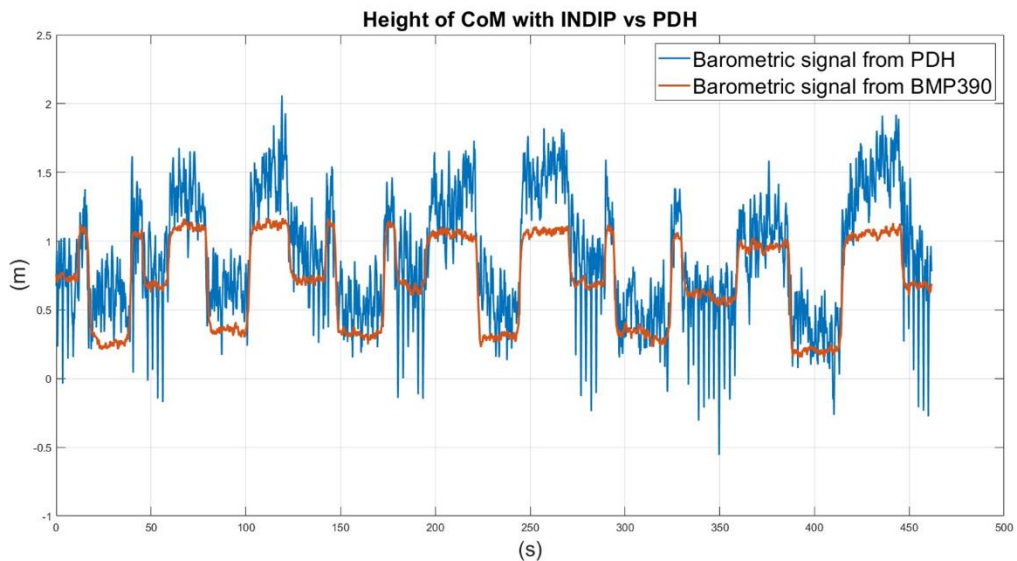


Fig. 45: Comparison of CoM displacement between INDIP-barometer and PHD sensor.

Performance evaluations were conducted by comparing the heights obtained from the barometers to the reference, the stereophotogrammetric signal. The results are presented in table 7

Mean value	Max error (cm)	mean error (cm)	RMSE (cm)	MAPE(%)	Pearson coefficient
BMP390	48,33	-7,23	8,55	13,52	0,93
PDH	130,41	13,63	25,45	48,83	0,57

Tab. 7: Performances of height reconstruction with BMP390 and LPS27HHW barometers relative to the gold standard.

3.1.1.3 Muse v3

MUSE, a product of the company 221e, is a low-power, miniaturized, wireless multi-sensor logger that integrates state-of-the-art sensing technology into a compact, robust, customizable, and user-friendly platform [37]. It includes inertial and environmental sensors, on-board flash storage, wireless connectivity, automated on/off functions, and a regulated rechargeable power supply. This design ensures a versatile system for data acquisition across multiple applications. Fully certified and safe, MUSE serves as a production and professional research platform for wearable and connected industrial use cases.

MUSE has been employed in a range of wearable and IoT devices developed by global enterprises, innovative startups, and leading researchers worldwide. Its capabilities include measuring acceleration, angular rates, 3D rotation, magnetic fields, temperature, humidity, proximity, ambient light, ambient pressure, and signal intensity.

Notably, the pressure sensor incorporated in the MUSE v3 is the LPS22HH from STMicroelectronics [38]. The temperature and ambient pressure are sampled at a fixed rate of 25 Hz, while the inertial unit has a sample frequency of 100Hz. The dedicated software samples inertial, temperature and barometric data at a frequency of 100Hz.

The sensors were mounted on a rigid axis for the execution of the preliminary test (Fig.46). The test involved raising and lowering the sensors to known heights; they were left in static conditions for approximately 25 seconds before the next raising or lowering.

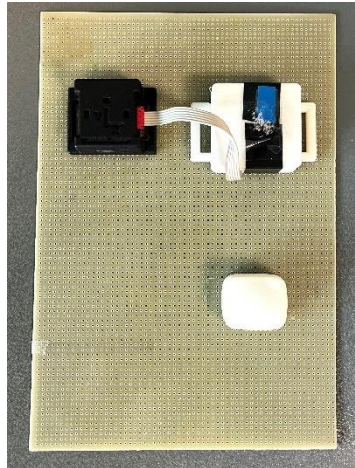


Fig. 46: Muse and INDIP sensors mounted and fixed on a fixed axis, to execute the comparison.

The barometric signals were converted into altitude, with the barometric formula. The BMP390 barometer is configured with pressure oversampling (x16), temperature oversampling (x2), and low-pass filtering (IIR coefficient=15). To compare the signals, the barometric data from the MUSE was filtered using a filter equivalent to the one present on board the BMP390. The data from different sensors are aligned through the initial execution of 3 rotation.

The following plot highlights the signals acquired from both sensors and the reference displacement (Fig.47).

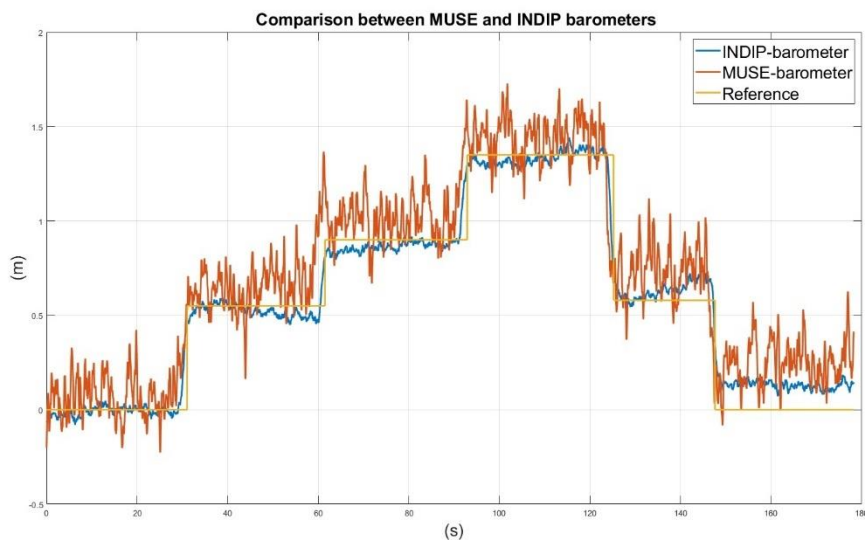


Fig. 47: The image highlights the signals from BMP390 barometer, integrated in the INDIP system, and LPS22HH barometer, integrated in the Muse. The test involved raising and lowering the sensors to known heights (yellow signal).

The standard deviation calculated on static condition, when the barometers are positioned on the ground, are 10.8 cm for the Muse barometer and 2.3 cm for INDIP barometer.

3.1.3 Determination of the firmware parameters for BMP390

The INDIP system has been integrated with the BMP390 sensor, which provides accurate measurements of both pressure and temperature. Notably, the pressure measurement is compensated with the temperature measurement to ensure precision.

The BMP390 sensor [39], a piezoresistive pressure sensor, supports oversampling of pressure and temperature measurements by an oversampling factor, ranging from 0 to 32. Moreover, the sensor’s firmware incorporates an Infinite Impulse Response (IIR) digital filter designed to mitigate short-term disturbances in the output data caused by environmental factors such as door slamming or air movement around the sensor. This filtering process effectively narrows the bandwidth of the output signal, with filter coefficients adjustable from 0 (off) to 127. The filtered output data is computed using the following formula (41):

$$data_{filtered} = \frac{data_{filtered_{old}} * filter_{coefficient} + data_{ADC}}{filter_{coefficient} + 1} \quad (41)$$

where $data_{filtered_{old}}$ is the signal from the previous acquisition while $data_{ADC}$ is the data obtained from the ADC prior to IIR filtering.

Fig. 24 illustrates the sensor measurement cycle, which includes the processes of measuring temperature and pressure with potential oversampling. .

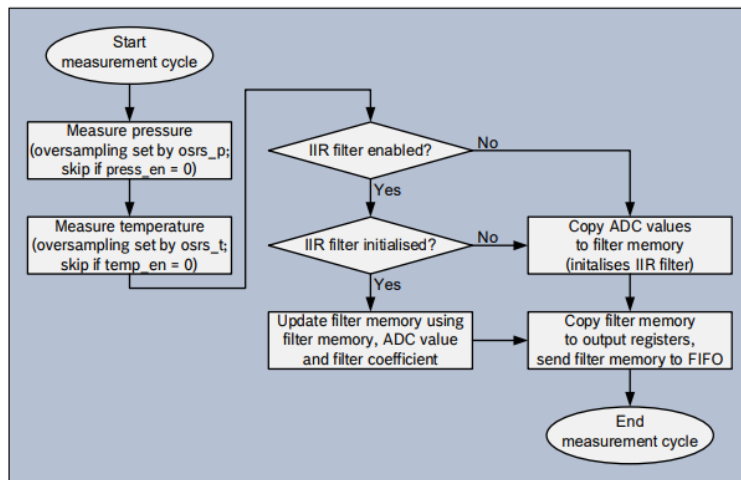


Fig. 218: Overview of the measurement cycle, which includes the processes of measuring temperature and pressure with potential oversampling. Following the measurement phase, the data undergoes filtering using the IIR filter.

In the context of the BMP390 sensor configuration, pressure measurement can either be executed or bypassed; when bypassed, the sensor exclusively detects temperature. When pressure measurement is executed, multiple oversampling options are available. Each oversampling setting reduces noise and increases the resolution of the output data by 1 bit. The pressure oversampling settings (*osr_p*) are specified in the "OSR[2:0]" register. Tab.1 presents the pressure oversampling options, highlighting the configuration utilized in this study.

Oversampling setting	<i>osr_p</i>	Pressure oversampling	Typical pressure resolution	Recommended temperature oversampling
Ultra low power	000	×1	16 bit / 2.64 Pa	×1
Low power	001	×2	17 bit / 1.32 Pa	×1
Standard resolution	010	×4	18 bit / 0.66 Pa	×1
High resolution	011	×8	19 bit / 0.33 Pa	×1
Ultra high resolution	100	×16	20 bit / 0.17 Pa	×2
Highest resolution	101	×32	21 bit / 0.085 Pa	×2

Tab. 1: Oversampling settings for the pressure measurement. The setting highlighted in red is the one chosen for the present study.

Similarly, temperature measurement can either be executed or avoided; in the latter case, the sensor can provide pressure readings more rapidly. When temperature measurement is executed, multiple oversampling options are available, each reducing noise and increasing the resolution of the output data by 1 bit. The temperature oversampling settings (*osr_t*) are specified in the "OSR[5:3]" register. The table below presents the temperature oversampling options, highlighting the configuration utilized. It is advisable to select the *osr_t* value based on the set value of *osr_p*, as indicated in the previous table. Oversampling temperature beyond x2 is possible, but it will not significantly enhance the accuracy of the pressure output, as the noise in the compensated pressure value is more influenced by the raw pressure noise than the raw temperature noise.

<i>osr_t</i>	Temperature oversampling	Typical temperature resolution
000	×1	16 bit / 0.0050 °C
001	×2	17 bit / 0.0025 °C
010	×4	18 bit / 0.0012 °C
011	×8	19 bit / 0.0006 °C
100	×16	20 bit / 0.0003 °C
101	×32	21 bit / 0.00015 °C

Tab. 2: Oversampling settings for the temperature measurement. The setting highlighted in red is the one chosen for the present study.

Regarding data sampling frequency, the maximum sampling rate is 200Hz, and it depends on the settings for temperature and pressure oversampling. Tab.3 outlines the typical and maximum measurement times based on the oversampling settings. The settings selected for this study provide a sampling frequency of 25Hz. Given that the INDIP system samples at 100Hz, there will be four identical samples in the pressure and temperature signals.

Oversampling setting	Pressure oversampling	Temperature oversampling	Measurement time[ms]		Measurement rate [Hz]	
			Typ	Max	Typ	Min
Ultra low power	×1	×1	4.82	5.70	207.08	175.39
Low power	×2	×1	6.84	7.96	146.00	125.56
Standard resolution	×4	×1	10.88	12.48	91.83	80.07
High resolution	×8	×1	18.69	21.53	52.71	46.42
Ultra high resolution	×16	×2	37.14	41.89	26.91	23.86
highest resolution	×32	×2	69.46	78.09	14.39	12.80

Tab. 3: The table highlights the range of the measurement frequency related to the pressure and temperature oversampling.

Other configurations, in addition to the final one indicated in this paragraph, have also been analyzed, as will be demonstrated in the following sections.

3.1.3 Characterization of BMP390

In the initial phase of this work, tests were conducted to understand the functioning of the barometric sensor and to characterize it. The tests were performed using the sensor's configuration denoted in the datasheet as “Indoor Navigation” [39], with the following settings (Tab.4):

Sampling frequency f_s	25 Hz
Pressure oversampling factor	x 16
Temperature oversampling factor	x 2
IIR filter coefficient	15

Tab. 4: BMP390 set up for preliminary tests.

This configuration was chosen because it is recommended in the datasheet for using the sensor as an altimeter, which aligns with the objectives of this thesis. The tests conducted can be categorized into three groups.

Static tests - Test 1 and Test 2

Initially, two tests (*Test 1* and *Test 2*) were conducted to evaluate the pressure values recorded by the sensors in static conditions and to identify any trends over time. The physical setup for both tests is illustrated in Fig.25: two sensors (indicated as #72 and #102) for each test were positioned at a constant height of 58 cm above the floor and maintained at this height for the entire duration of the acquisition, which lasted ten minutes.



Fig. 219: Set up for *Test 1* and *Test 2*. The sensors are positioned at constant height, in static condition.

Tests 1 and *2* were performed consecutively on the same day, with negligible variations in atmospheric conditions. Specifically, in *Test 1*, four repetitions were performed, during which the two sensors were turned off and then turned back on between each repetition. Prior to signal acquisition, the sensors were allowed to stabilize in place for approximately ten minutes.

In contrast, during *Test 2*, the two sensors remained powered on between successive acquisitions. This approach was used to evaluate any potential differences in sensor performance and stability when continuously powered. The signals recorded by the sensors during one of these repetitions are shown in figure 26.

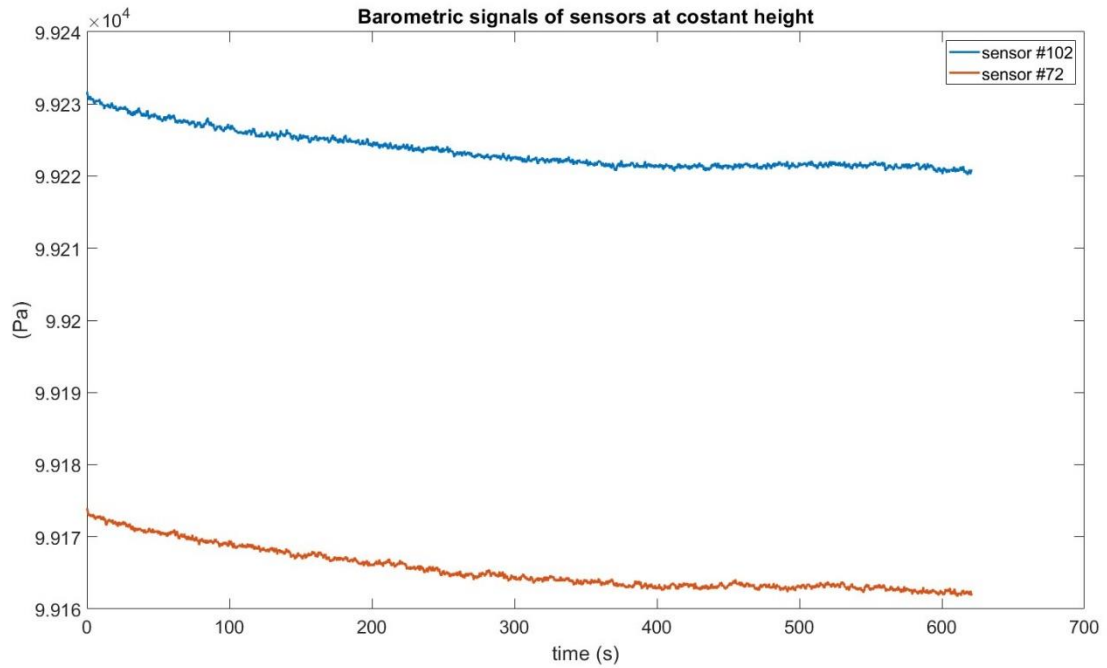


Fig. 26: The image shows the barometric signals of the two sensors acquired during a repetition of Test 2, in static condition.

Tab.5 contains the mean values and standard deviations of the barometric signals for each repetition relative to *Test 1*. Furthermore, the table includes the differences between the mean values of the two sensors across all repetitions. The same values are reported for *Test 2* (Tab.6).

Pa	Mean value sensor #72	Mean value sensor #102	Standard deviation sensor #72	Standard deviation sensor #102	Difference between the mean values
Repetition 1	99051,53	98992,89	5,84	6,31	58,64
Repetition 2	99009,87	98950,07	3,14	3,62	59,81
Repetition 3	98988,38	98928,46	2,65	2,99	59,92
Repetition 4	98969,37	98910,03	0,95	0,71	59,33

Tab. 5: Mean values, standard deviations of the barometric signals and differences between the mean values of the two sensors across all repetitions relative to Test1.

Pa	Mean value sensor #72	Mean value sensor #102	Standard deviation sensor #72	Standard deviation sensor #102	Difference between the mean values
Repetition 1	99223,55	99165,45	2,92	2,62	58,10
Repetition 2	99209,43	99150,61	2,68	3,28	58,83
Repetition 3	99203,15	99143,91	1,96	1,84	59,24
Repetition 4	99197,01	99137,83	3,59	4,04	59,17

Tab.6: Mean values, standard deviations of the barometric signals and differences between the mean values of the two sensors across all repetitions relative to Test2.

To compare the values reported in the tables for the two conditions analyzed in *Test 1* and *Test 2*, a scatter plot is provided (Fig.27), illustrating the mean values and corresponding standard deviations for each repetition. It can be observed that the difference between the mean values of the sensors placed at the same height consistently approximates 60 Pa, for each repetition of both tests. For pressure values around 99000 Pa, which correspond to atmospheric pressures observed in the tests, a difference of 60 Pa translates to approximately 5.3 meters. In Test 2, with the sensors left turned on between transitions, the mean pressure values of the four repetitions are more similar one to each other than in Test 1.

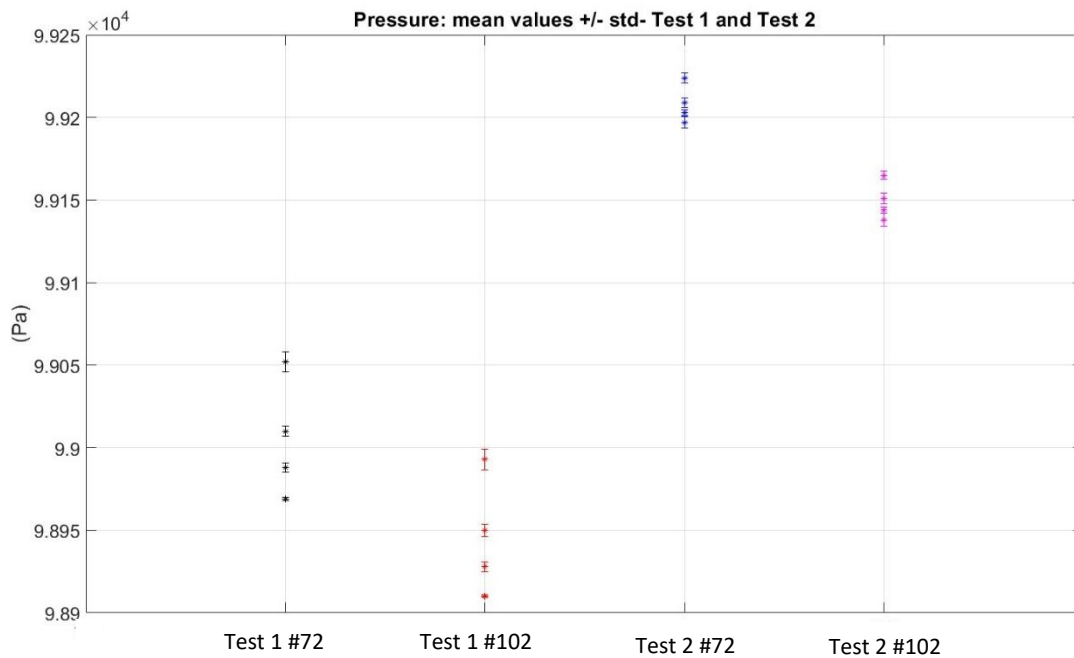


Fig.27: Scatter plot of (mean values \pm standard deviations) of barometric signals in static condition during repetitions of Test 1 and Test 2. Each test is repeated four times and is represented on the graph by a point, indicating the average pressure value, and by an error bar, which represents the standard deviation of the pressure values during the test.

Test 3

Temperature variations and the presence of airflow on the sensor are additional factors influencing atmospheric pressure. To evaluate the impact of these elements, *Test 3* was conducted. During this test, the sensors were placed at a constant height on a cart, which was maintained throughout the data acquisition period, while the temperature varied.



Fig.28: Set up used for Test 3. The sensors were placed at a constant height on a cart, subjected to temperature variations.

In the first repetition (Fig. 29), the temperature decreased as the sensors were moved into an air-conditioned room. For the second and third repetitions (Fig. 30 and Fig. 31), the temperature increased due to the heat emitted by a hairdryer, which also exposed the sensors to moving air. Despite the temperature changes, the sensor pressure readings remained stable.

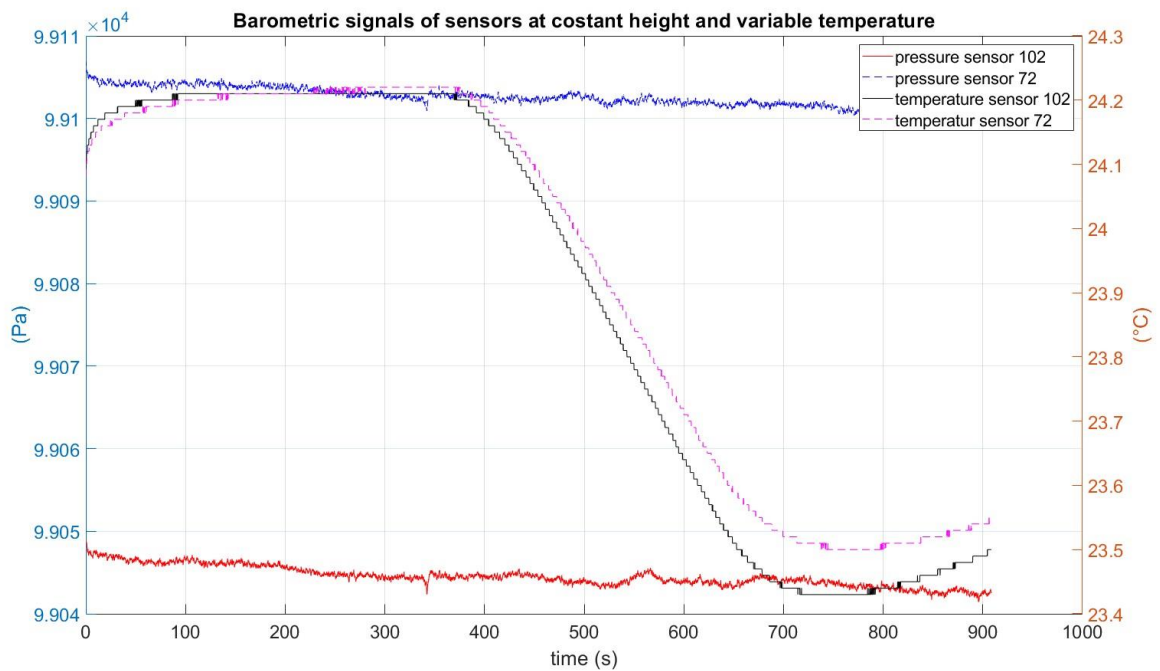


Fig.29: Barometric and temperature signals during the exposition of decreasing temperature.

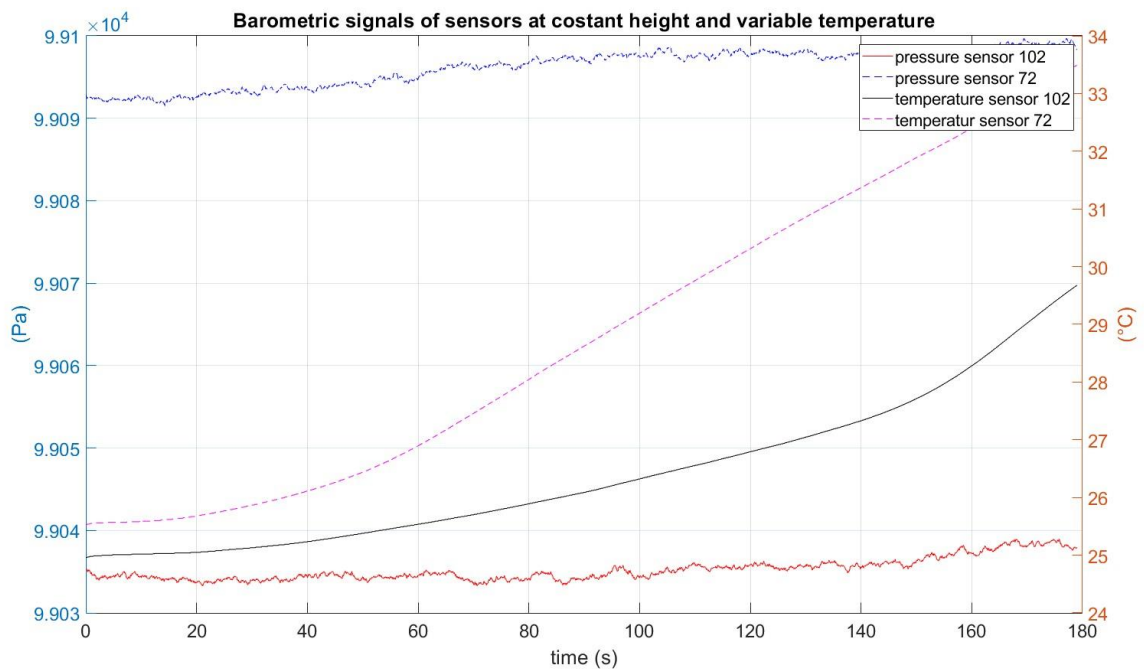


Fig.30: Barometric and temperature signals during the exposition of increasing temperature.

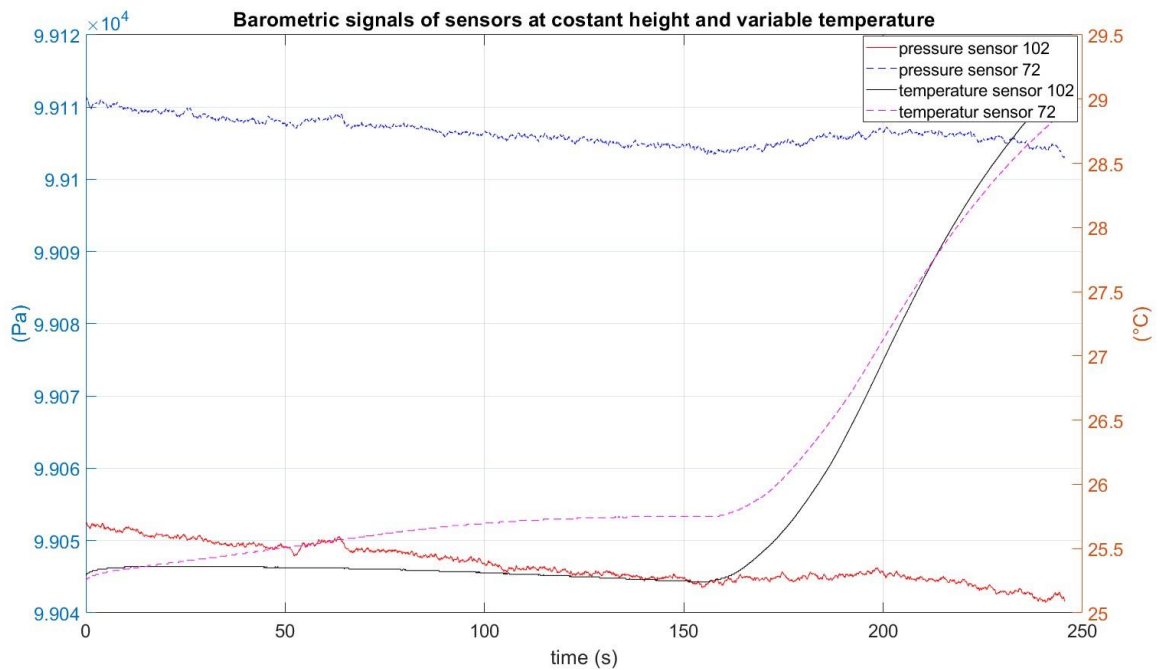


Fig.31: Barometric and temperature signals during the exposition of increasing temperature.

Test 4

Test 4 considers the use of the barometer as an altimeter, i.e., the function for which it is used in this work. The objective was to observe the altitudes estimated by the barometers with respect to

the reference heights and their minimal achievable resolution using both sensors. Due to the unavailability of a statimeter, a measuring instrument used to measure height, stacked boxes, each with a constant height of approximately 4.25 cm, were used to position the barometer at increasing heights. Two sensors were used: one barometer was kept stationary on the floor, while the other was first brought to the ground and then moved to increasing heights at constant intervals (0 cm, 4 cm, 0 cm, 8 cm, 0 cm, 12 cm, and so on), as marked by a stopwatch. The final height reached was approximately 60 cm, corresponding to 14 stacked boxes.

The experimental setup, as described, is shown in Fig.32. The actual movement of the sensor relative to the floor is indicated in blue (Fig.33).



Fig. 32: Experimental set up for Test 4.

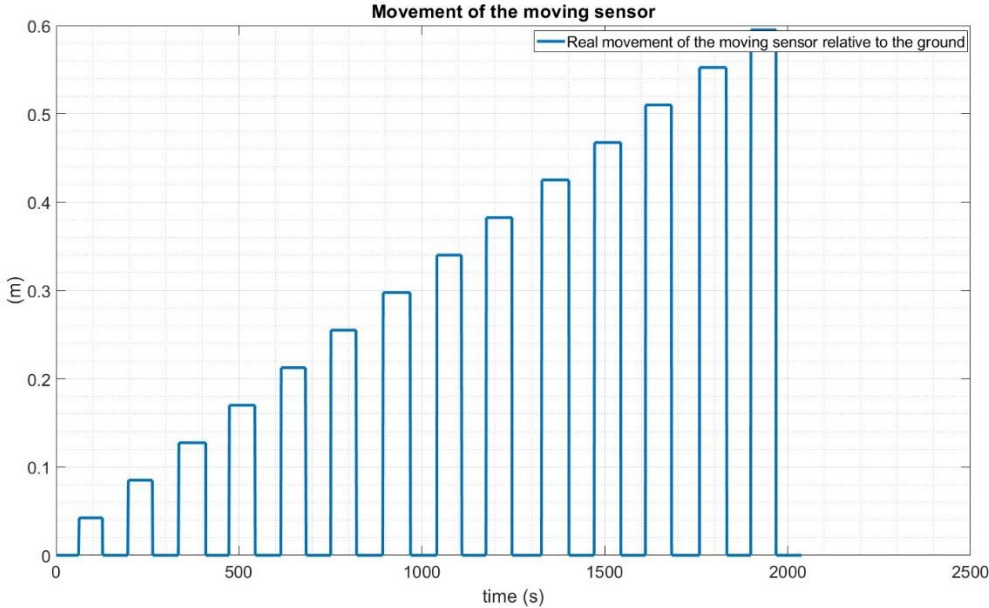


Fig. 33: The signal corresponds to the true vertical displacement of the sensor that is positioned at increasing height relative to the ground, used as reference.

The signals of the two barometers are presented in Fig. 34. As highlighted through *Tests 1* and *2*, it is observed that when the two sensors are positioned at the same height, that is, at the beginning of the Test 4 when both are at floor level, the pressure values differ by approximately 60 Pa.

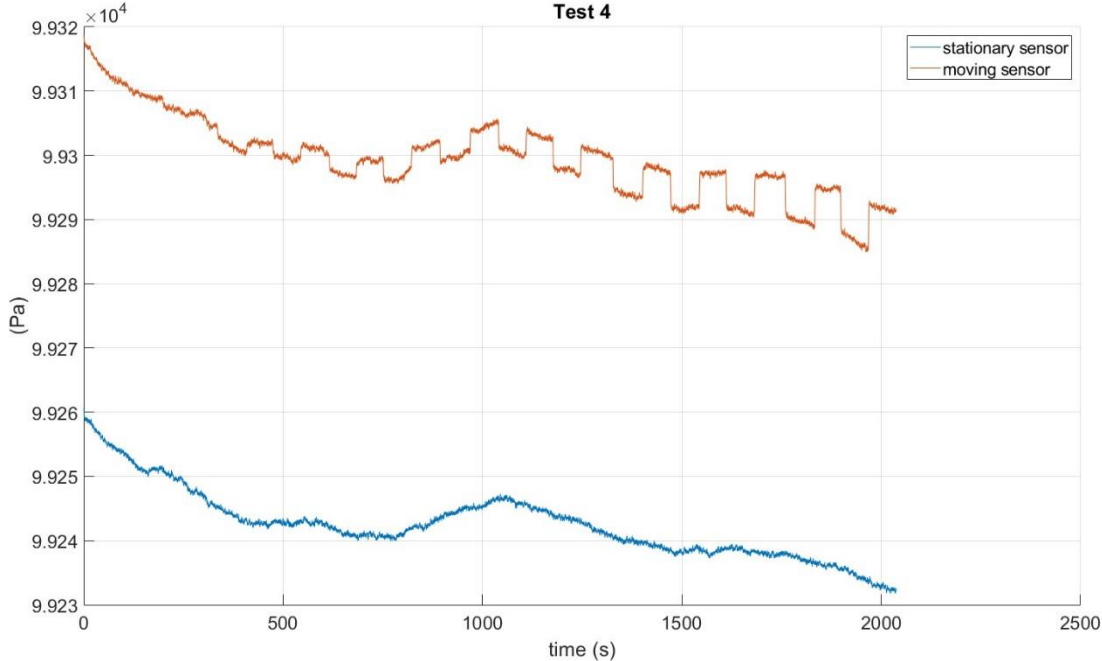


Fig. 34: The red signal corresponds to the pressure sensor that is moving, positioned at increasing height. The blue signal corresponds to the stationary barometer, located to the ground.

The barometric formula was first used to convert the barometric data into height, after aligning the signals by removing the 60 Pa difference. To estimate height relative to the ground from the sensors' readings, two approaches were followed: a single sensor setup and a dual sensors setup. In the dual sensors setup, the raw barometric signal of the moving sensor is transformed into height (Fig.35), using the pressure perceived by the stationary sensor on the floor as the reference pressure (P_0 in the barometric formula, paragraph 2.2.2.2). By calculating the average values of the raw barometric signal when the moving sensor was stationary at a constant height, it was possible to compare the height differences perceived by the two barometers (signal in red) against the reference height difference (signal in yellow) as shown in Fig.35.

Fig.36 illustrates the same information but reports only the height mean values at each step.

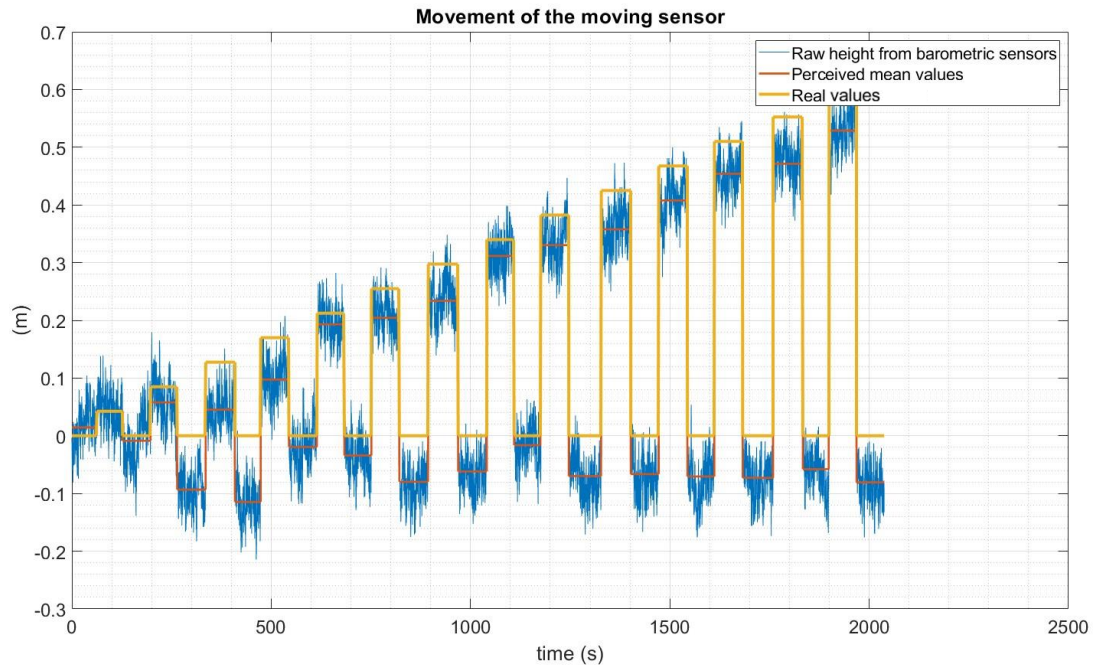


Fig. 35: Height relative to the ground estimated by the moving sensor relative to the barometer located at the ground in static condition, obtained through the barometric formula. The red signal represents the mean values of the dual sensors setup signal when both sensors are at constant height. The yellow signal is the reference signal.

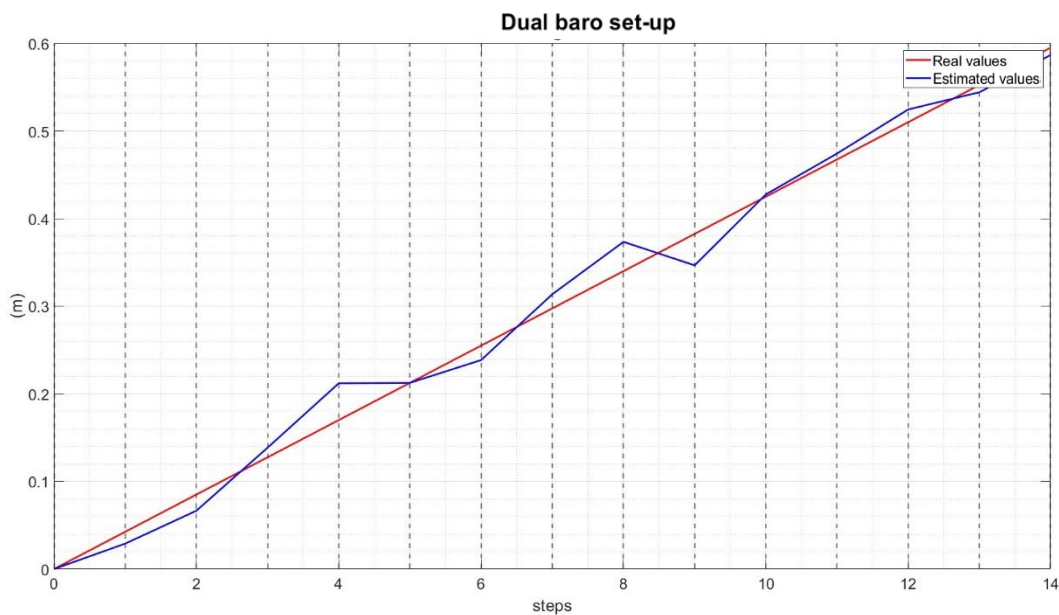


Fig. 36: The plot highlights the height differences of the barometer (blue signals) between one step and the following.

The same procedure was followed using the single sensor setup, with the pressure at the beginning of the trial from the moving sensor serving as the reference pressure (P_0 in the barometric formula, paragraph 2.2.2.2). Fig.37 again displays the movement of the sensor and the perceived height differences. Fig.38 illustrates the same information but reports only the height mean values at each

step. The signal is affected by an increasing trend, which negatively impacts performance compared to the dual sensor setup results.

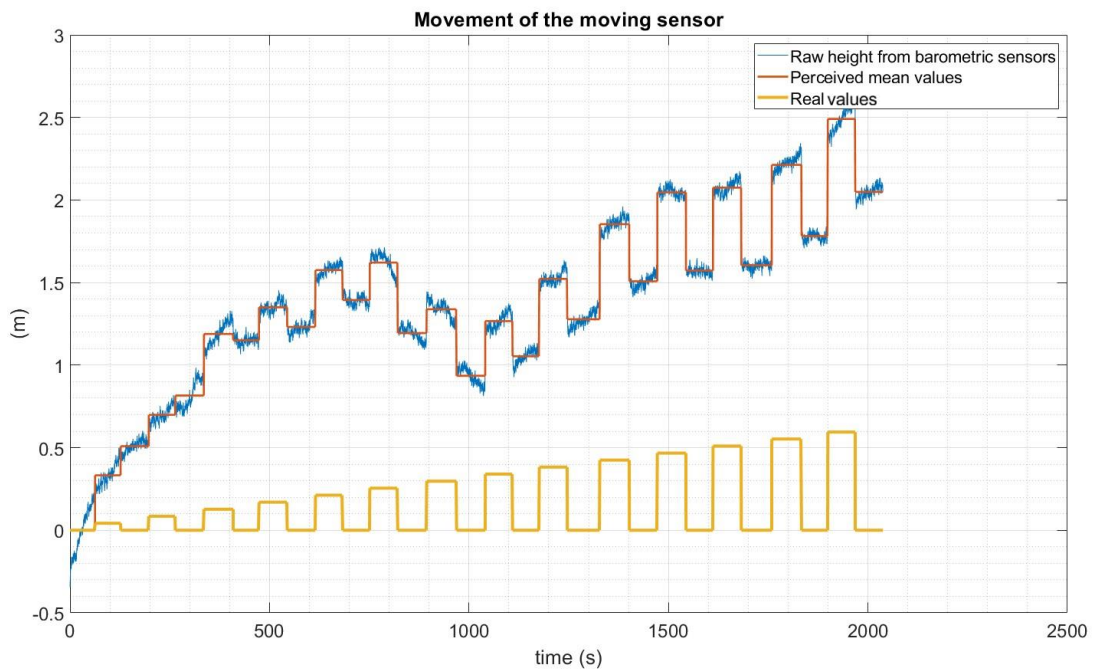


Fig. 320: The image shows the height of the moving sensor relative to the ground, obtained through the barometric formula with the single sensor set up. The red signal represents the mean values of the barometric signal when the sensor is at constant height. The yellow signal is the reference signal, that highlights the real movement executed.

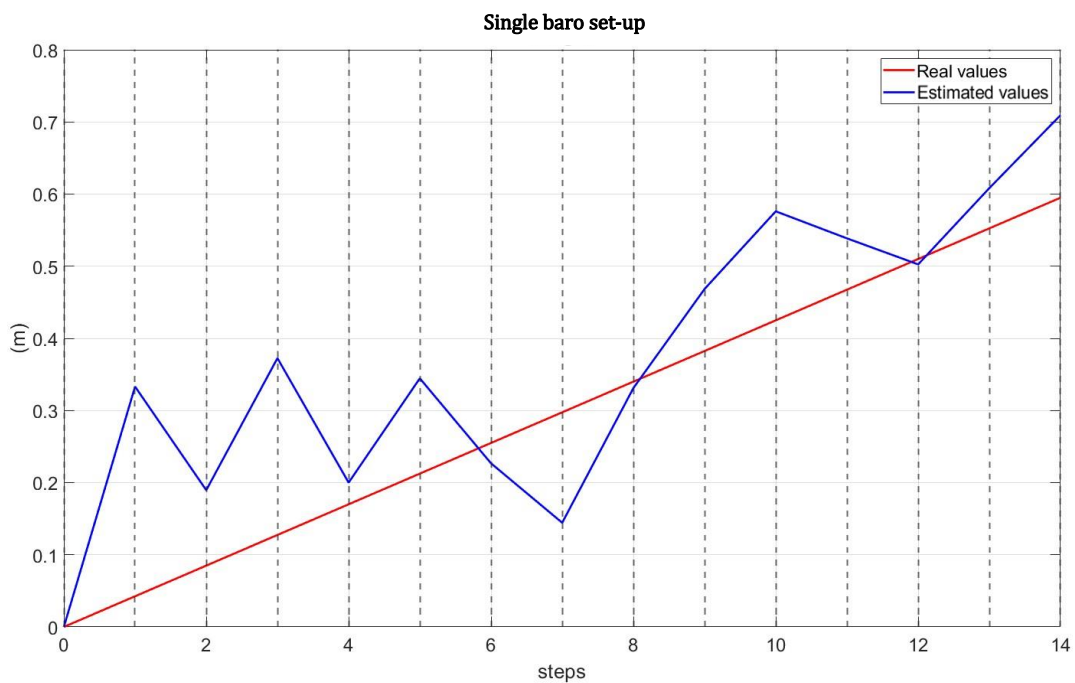


Fig. 321: Relative height at each level with respect to the previous level. Since the inter-levels step was approximately of 4 cm, the reference label (red line) is a line with constant slope.

In both setups, height differences of approximately 4 cm were detected. Both the configurations provided a direct assessment of the vertical movement performed by the moving sensor with respect to the sea level (single-sensor setup) or the stationary sensor (dual-sensor setup). Such test demonstrated that the dual-sensor setup is reliable in quantifying relative height, as it effectively eliminates common sources of interference.

3.2 Experimental setup

The recording systems utilized for the study include the wearable multi-sensor system INDIP and the stereophotogrammetric system Vicon.

3.2.1 The INDIP System

The INertial module with DIstance Sensors and Pressure insoles (INDIP) is a multi-sensor wearable system that combines multiple MIMUs with other wearable sensors (pressure insoles, time-of-flight distance sensors, barometers) for human motion analysis purposes. It was designed by Università degli Studi di Sassari and it was originally designed as a validation tool for other devices used in gait analysis as part of the European Project, Mobilise-D. By leveraging the redundancy of information from different sensing principles and incorporating cutting-edge technologies and algorithms, the INDIP system has the potential to serve as a benchmark ("best available" reference) for real-world movement assessment applications [40]. The INDIP system is modular, meaning that the number and type of sensors included in the setup can change depending on the application.

The complete INDIP setup includes various inertial, pressure, and distance wearable sensors, which can be used individually or simultaneously (Fig. 48). In particular seven MIMUs, placed on the head, wrists, lower back, and feet, attached using Velcro bands to prevent slippage and motion artifacts; two pressure insoles (one for each foot) placed within the participant's shoes, where each insole contains 16 pressure sensors, providing detailed mapping of foot-to-ground contact and protected by rubber insoles to avoid damage to the sensing components; two IR distance sensors attached to the shanks with Velcro.

In the present study, the setup included only magneto-inertial modules of the INDIP system and pressure sensors of the selected model (BMP390L), specifically integrated into the INDIP system at both firmware and hardware levels

The INDIP system samples at a frequency of 100 Hz, while the barometer at a frequency of 25Hz. Thus, in the barometric signal there are four identical samples. Prior to each recording session,

MIMUs must be individually connected via USB to a computer to synchronize their timestamps with the current date. This process, facilitated by a custom graphical user interface (GUI) developed in Matlab, is essential to ensure that the timestamps from different sensors are aligned and free from delays.

After synchronization, the MIMUs are positioned on the participant's body and connected via Bluetooth Low Energy (BLE) to a custom app also developed in Matlab. This app allows the user to initiate data acquisition from all connected sensors. Once the acquisition begins, the participant is free to move. While the MIMUs may disconnect from the computer if the participant moves out of range, they continue recording data offline. At the end of the recording session, the sensors can be reconnected to the app via BLE to stop data acquisition, and then connected via USB to the GUI to download the recorded data.

Each magneto-inertial module included a 3D accelerometer (range: ± 16 g), a 3D gyroscope (range: ± 2000 °/s), and a 3D magnetometer (range: ± 50 Gauss). Magneto-inertial modules also serve as recording units, as they contain the CPU (ARM® 32-bit Cortex®-M4), a Bluetooth module for wireless communication, and a 128 MB flash memory for data storage, allowing for up to twelve hours of data logging. Additionally, the system supports synchronization with third-party devices via an external trigger.

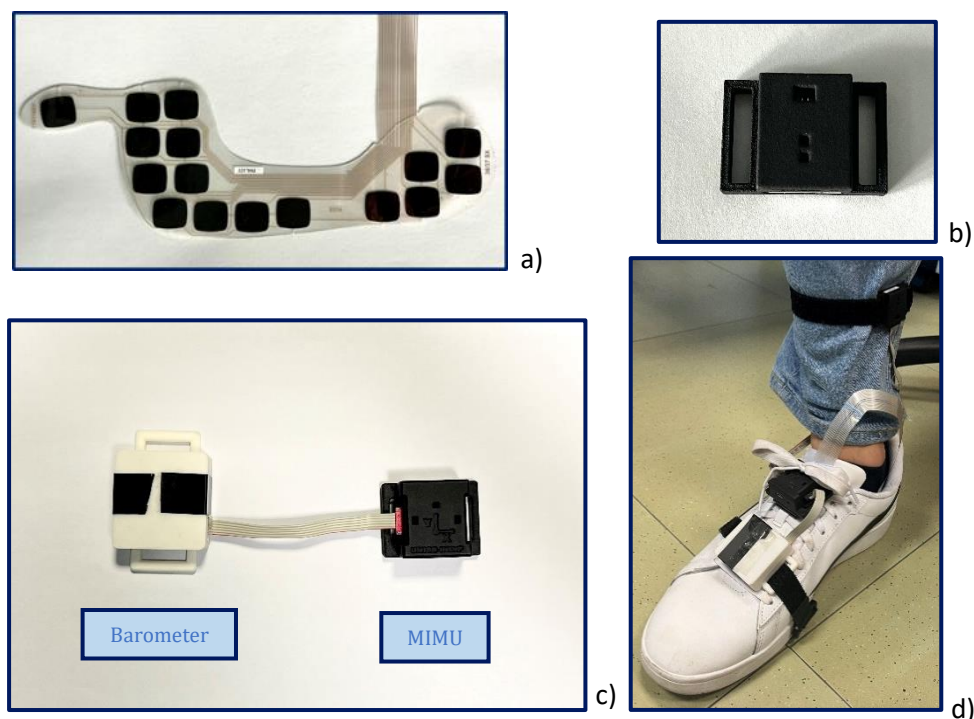


Fig. 48: INDIP System with a) pressure insoles with 16 force resistive sensing elements, b) time-of-flight distance sensors, c) MIMU connected to the BMP390 pressure sensor; d) complete setup worn on the lower limb for gait analysis. The configuration used in this study includes only the INDIP system equipped with a magneto-inertial module and barometer (c).

The MIMU and barometric sensors enclosures are connected via a six-pin stripe cable approximately 6 cm in length (Fig.48).

3.2.2 Vicon reference system

Vicon Nexus® is a CE-marked stereophotogrammetric motion capture platform. The system comprises a personal computer, a connectivity unit, 14 Vero infrared-sensitive cameras, 3 Bonita visible-light-sensitive cameras, passive infrared-reflective markers to be attached to the subject, proprietary software for reconstructing marker positions within the acquisition space and applying biomechanical models provided with the system. From this reconstruction, kinematic parameters of motion, such as joint angles, angular velocities, and angular accelerations, can be obtained. The active components of the device do not come into contact with the subject, who only wears passive spherical reflective markers, each weighing 1-2 grams. The frame rate of the infrared-sensitive cameras is set to 100 Hz, which is sufficiently high to capture the detailed movements considered in the study.

3.3 Experimental protocol

3.3.1 Minimum Sample Size and Demonstration of Achievability of Results

Determining the minimum sample size in a study is crucial to ensure that the results are statistically significant and reliable. A statistical power analysis was conducted to define the minimum number of subjects (n) required, following the procedure proposed in [41] (42,43,44,45):

$$n = 1 + \frac{2(z_{\alpha} + z_{\beta})^2 * k}{l_n^2(C_0) * (k - 1)} \quad (42)$$

$$C_0 = \frac{1 + k\theta_0}{1 + k\theta_1} \quad (43)$$

$$\theta_0 = \frac{R_0}{1 - R_0} \quad (44)$$

$$\theta_1 = \frac{R_1}{1 - R_1} \quad (45)$$

where $\alpha = 0.05$ is the significance level;

$\beta = 0.9$ is the power of the analysis;

$z_{\alpha} = 1.96$ is the critical value for α assuming a standard normal distribution;

$z_{\beta} = 1.64$ is the critical value for $1-\beta$, assuming a standard normal distribution;

$k = 2$ is the number of measurements (tests for each subject);

$R_0 = 0.7$ is the minimum acceptable value of the intra-class correlation coefficient (ICC);

$R_1 = 0.94$ is the expected ICC value.

The power analysis showed that the minimum number of subjects needed for an $ICC > 0.94$ is 20, with a number of tests per subject equal to 2 (k).

3.3.2 Tests

Tests were conducted within the BIOMed Movement Analysis Room at the interdepartmental center PoliToBIOMed Lab of the Polytechnic University of Turin, Corso Castelfidardo 30/a, Turin, Italy.

The need to use this space for acquisitions is due to the presence of Vicon Nexus® systems within the specified laboratory.

The necessary equipment for this work included two INDIP devices (two to be attached to the subject), the VICON stereophotogrammetric system connected to the respective desktop computer, a laptop with software installed for communication with INDIP, two portable scales, a couch, and two chairs. The stereophotogrammetric system and INDIP systems were synchronized through the use of a third INDIP, synchronized with both.

The twenty volunteers signed an informed consent form indicating their willingness to participate in the study voluntarily, having been informed about the study procedures and objectives, and authorizing the researchers to use the recorded signals, stored in a completely anonymized form (see paragraph 3.3.3).

The volunteers wore the two INDIP systems. One device was attached on the lower back at the level of the fifth lumbar vertebra of the subject (approximately close to the CoM) using a waistband, and the other to the left foot using a snap clip and a velcro strap. At the time of attachment, the operators ensured that neither the clip nor the velcro caused discomfort, inconvenience, or pain to the participant.

A marker was attached to the case of each barometric sensor. Additionally, a third reference marker was attached at the sternum level. The use of markers is due to the need to accurately

measure the vertical trajectory performed by the pelvis and foot during the experiments to compare it with that estimated by the INDIP devices. Specifically, to directly compare the estimates of the wearable sensors with those of stereophotogrammetry, the markers are firmly attached to the case of each barometer using double-sided tape. The presence of the third marker attached to the sternum of the participant is related to the need for the VICON cameras to have at least three points to reconstruct the planes on which the markers lie.

The INDIP system positioned on the pelvis is attached to a rigid support containing 4 markers at its corners, allowing for the verification of the estimated orientation's accuracy. In total, 7 markers were used.

The complete setup is shown in the following images (Fig.49).

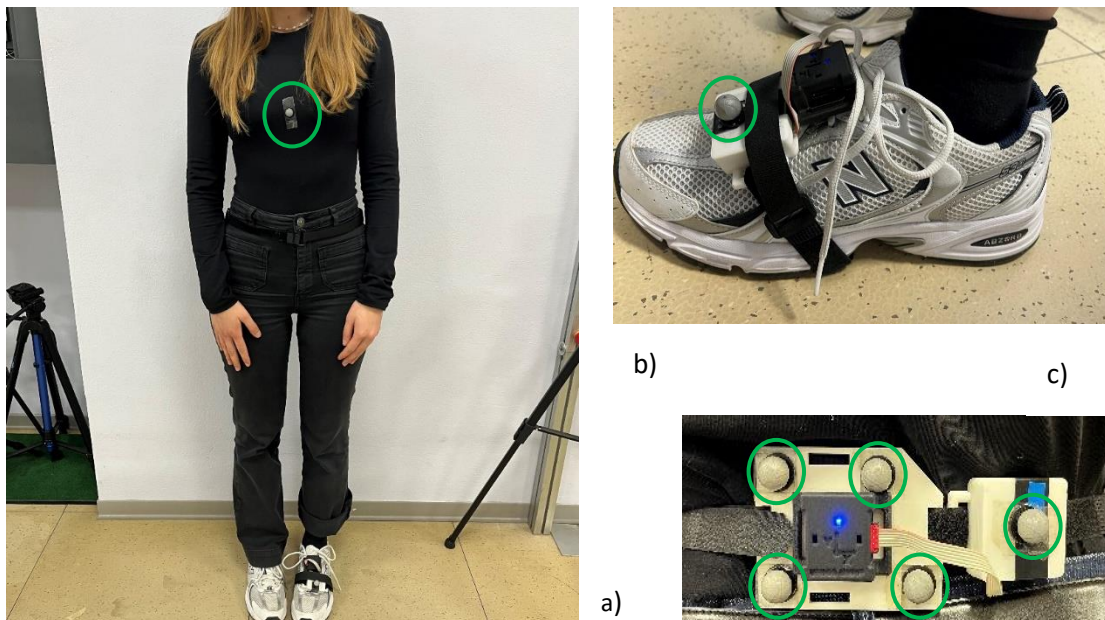


Fig. 49: INDIP systems and markers (green circled) worn by the subjects; a) subject frontal view, with highlighted the marker located on the sternum, and used as reference; b) focus on left foot, with the MIMU module (fixed with a snap clip) connected to the barometer (fixed with a velcro strap); c) INDIP system located on the pelvis with rigid support containing 4 markers at its corner.

Each subject performed four tests. Specifically, two tests involved performing actions commonly carried out in daily life, thereby simulating everyday conditions in the laboratory.

These activities required the vertical displacement of the subject's center of mass. Therefore, the purpose of these two tests is to validate the algorithm for reconstructing the CoM's vertical movement.

The other two tests conducted were the Sit-to-Stand and the Timed Up and Go tests. These were performed to evaluate the system's ability to extract clinically relevant parameters.

Below is the description of the tests conducted.

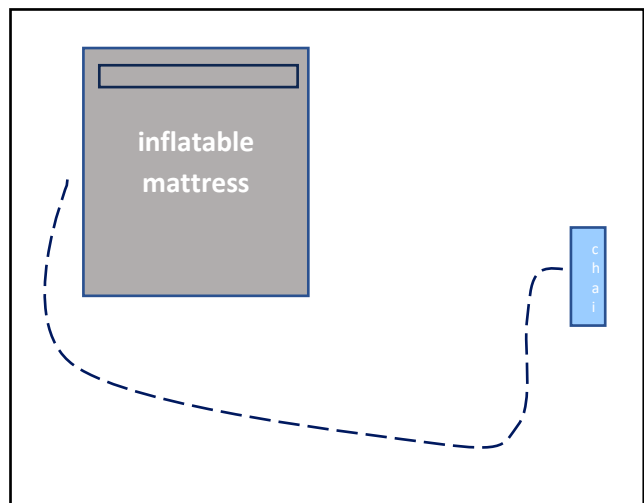
Test 1

The first test involved performing the following sequence of actions twice:

1. sitting on a chair (10s)
2. walking
3. lying down on a bed (15s)
4. walking
5. sitting on a chair (10s)
6. standing (5s)
7. walking
8. standing (5s)
9. lying down on a bed (15s)
10. standing (5s)
11. walking
12. standing (5s)
13. sitting on a chair (10s).



A)



B)

Fig. 50: Experimental set up used in Test 1 to evaluate the CoM's reconstruction of the vertical displacement. The set up includes the presence of a chair and a bed (inflatable mattress) to simulate everyday life transitions from a bed and a chair. The image shows A) the photo of the experimental setup conducted in the laboratory and B) its reconstruction to highlight the path taken by the subjects.

In the second repetition, the participants were asked to move slowly during the sit-to-stand and stand-to-sit transitions, using the side handles of the chair to support themselves, to evaluate the algorithm's ability to manage different types of sit-to-stand movements. Performing this movement slowly aimed to emulate the clinical conditions of elderly subjects or those with

pathologies, who can no longer perform these transitions smoothly. The experimental set up, as well as the walked circuit, are shown in Fig.50.

Test 2

The second test involved performing the following sequence of actions twice:

1. sitting on a chair (10s)
2. walking
3. climbing up and down the steps in succession
4. walking
5. squatting
6. walking
7. sitting on a chair (10s)
8. standing (5s)
9. walking
10. standing (5s)
11. climbing steps with a 5-second pause on each step
12. standing (5s)
13. walking
14. squatting
15. standing (5s)
16. walking
17. standing (5s)
18. sitting on a chair (10s)

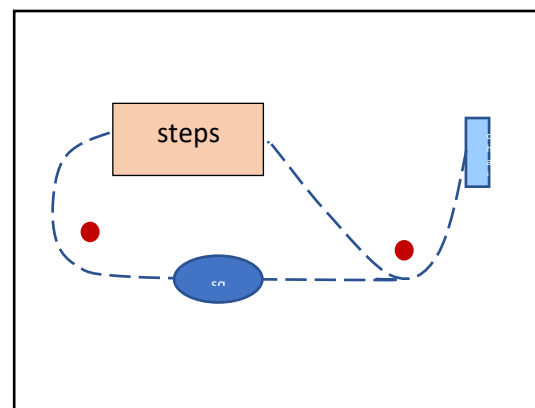


Fig. 51: Experimental set up used in Test 2 to evaluate the CoM's reconstruction of the vertical displacement. The set up includes the presence of a chair and steps to simulate everyday life transitions from chair or climbing up/down the stairs. The test also involves the execution of squat. The image shows A) the photo of the experimental setup conducted in the laboratory and B) its reconstruction to highlight the path taken by the subjects.

The squat was included to simulate everyday actions [26] where the center of mass is significantly lowered, such as picking up an object from the ground. The experimental set up is shown in Fig.51.

Tests 1 and 2 were designed in a way to obtain multiple recordings of the target actions (sitting, standing, laying, etc...), in order to observe the sensors' behavior over extended periods of time.

StS and TUG tests

Finally, two tests aimed at assessing the ability of the system to gain clinically-relevant data were performed:

- STS test: each subject performed 10 sit-to-stand transitions in succession holding their arms crossed.
- TUG test: each volunteer, starting seated in a chair, walked 3 meters in a straight line, turned, walked another 3 meters, and sat down again. the task was executed twice.

3.3.3 Request for ethical committee evaluation

The work proposed in this study was positively evaluated, upon prior request, by the Research Ethics Committee of the Polytechnic University of Turin, with protocol number 27213.

In the request document, the measures aimed at ensuring the safety of subjects, operators, and bystanders are highlighted.

The sample population is determined based on the following inclusion and exclusion criteria.

Exclusion Criteria:

- Being enrolled in the bachelor's or master's degree program in Biomedical Engineering;
- Age below 18 or above 65 years;
- Belonging to one of the classes defined as "vulnerable" under Regulation 2017/745;
- Presence of known pathologies that may render the subject incompatible with the study, such as ambulatory and/or motor disorders.

Inclusion Criteria:

- Willingness to participate in the study voluntarily;
- Absence of ambulatory problems and generally good physical health.

The inclusion and exclusion criteria were verified verbally during the first contact with the potential participant, before providing them any documents or recording any personal data. If the candidate met one or more of the exclusion criteria listed above, the potential participant was not enrolled. Vice versa, if a potential participant satisfied the inclusion and exclusion criteria, they were provided with the information sheet, and, if they were interested in participating in the study, they were given the Information Notice pursuant to Article 13 of the General Data Protection Regulation (EU) 679/2016.

The experimental protocol was divided into three phases, repeated for each volunteer:

1. Acquisition of informed consent and explanation of the study protocol;
2. Attachment of the two INDIP devices and their respective passive markers;
3. Execution of motor tasks.

In the first phase, volunteers were required to present the signed copy of the informed consent, previously provided to them during enrollment along with the information sheet. The researcher ensured to reiterate the key points of the study protocol and asked the volunteers if they had any questions before beginning. The subject was required to provide personally identifiable information, specifically their first and last name, as well as anthropometric data, namely weight and height. The personally identifiable information was collected through the informed consent form, will remain in paper form, and will be kept by the study supervisor. Anthropometric data and acquired signals were saved using a randomly generated alphanumeric code, which will not allow for any personal data of the participant to be traced.

4. Methods

4.1 Overview

As defined in the previous chapters, the objective of the present study is to develop a method for the reconstruction of the vertical trajectory of the BCoM of healthy subjects during the execution of simulated daily activities in a controlled environment. The developed algorithm was based on data recorded by body-mounted IMUs and barometers.

The main steps of the algorithm are summarized in Fig.52:

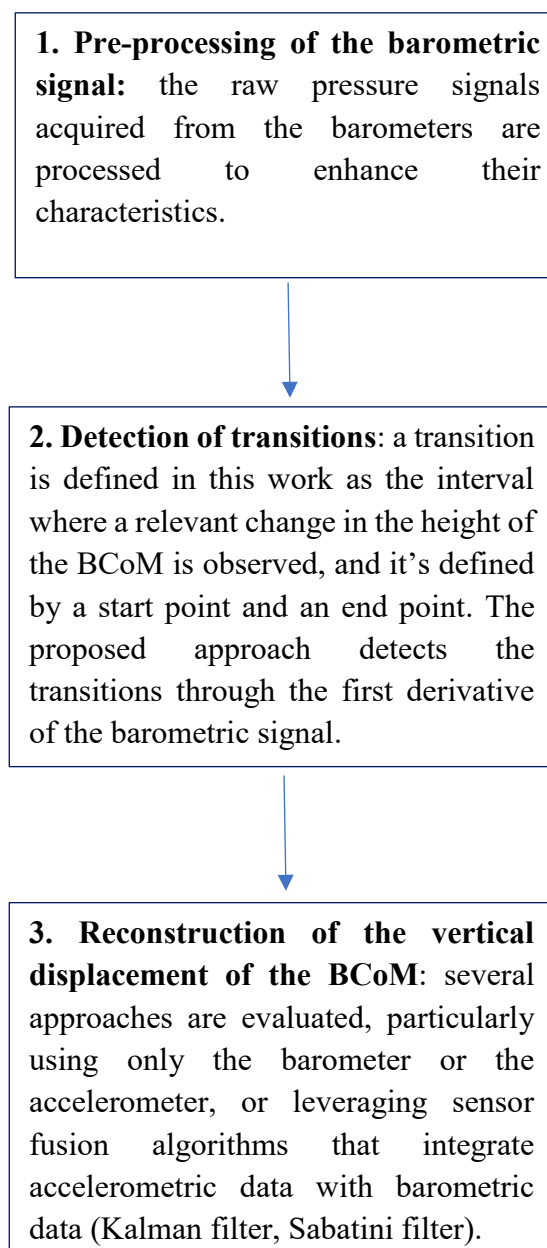


Fig.52: Description of the developed pipeline for reconstructing the vertical displacement of the BCoM using inertial and barometric sensors.

The algorithm for reconstructing the BCoM trajectory is based on three steps executed sequentially. The first step involves processing the barometric signal to convert it into height. The second step entails searching for transitions, while the third involves the actual reconstruction of vertical displacement.

4.2 Single device or double devices set-up

The experimental setup described in Chapter 3 included two INDIP-baro configurations positioned on the pelvis and on the left foot, each of them consisting of an inertial module and a barometer. Depending on the application, data recorded by only one (single-device setup) or both the configurations (double-device setup) can be used to extract information on the vertical displacement of the BCoM.

If the single-device setup is used, only data recorded by the IMU and the barometer placed on the pelvis are considered. In this case, during the conversion from Pascals to meters using the barometric formula (*paragraph 3.3.3*), the reference pressure P_0 is the pressure corresponding to the first sample of the barometer on the pelvis. This allows for the determination of the BCoM height during the trial relative to its initial position.

The initial condition, i.e., the initial height of the BCoM, is known: thus, the absolute height of the pelvis relative to the floor is obtained.

This configuration provides direct information on the vertical displacement of the pelvis relative to the floor; however, it is affected by common-mode interference such as drift and noise due to air movements or doors/windows opening and closing. Therefore, dedicated signal processing is required to mitigate these interfering elements.

If the dual-device setup is used, data recorded by both the INDIP-baro configurations positioned on the subject is used, specifically the one on the pelvis and the one on the foot. In this case, during the conversion from Pascals to meters of the pressure recorded by the barometer mounted on the lower back, the reference pressure P_0 is the pressure recorded by the barometer on the foot. Thus, unlike the single sensor setup, this value is not constant but varies along the trail, allowing for the determination of the BCoM height relative to the foot during the execution of movements. The information obtained with the two setups can coincide when the subject's foot remains fixed to the floor, a condition not met in the trials conducted during the experimental phase and in general not representative of daily life situations. Consequently, the dual sensor setup does not provide direct information on the absolute vertical displacement of the pelvis. However, the advantage is that it allows for the removal of interfering elements common to both barometers,

such as time-induced drift and noise due to air movements.

In conclusion, the two setups provide different but complementary information. The single-device setup allows for obtaining the absolute vertical displacement of the pelvis, while the dual-device setup enables noise removal. In this work, the vertical displacement of the BCoM is reconstructed using the single-device setup because it provides an absolute measure of the displacement and offers a simpler setup in terms of usability, making it easier to export the method to a home environment. Additionally, preliminary performance results were satisfactory for the purposes of this work.

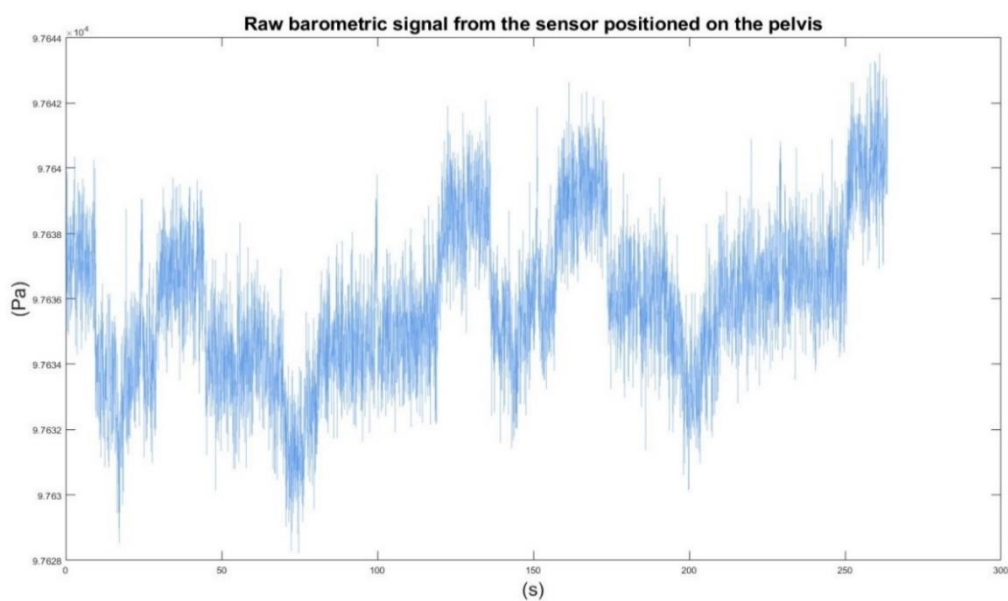


Fig. 53: Raw barometric signal acquired from the barometer located on the pelvis, during the execution of a trial.

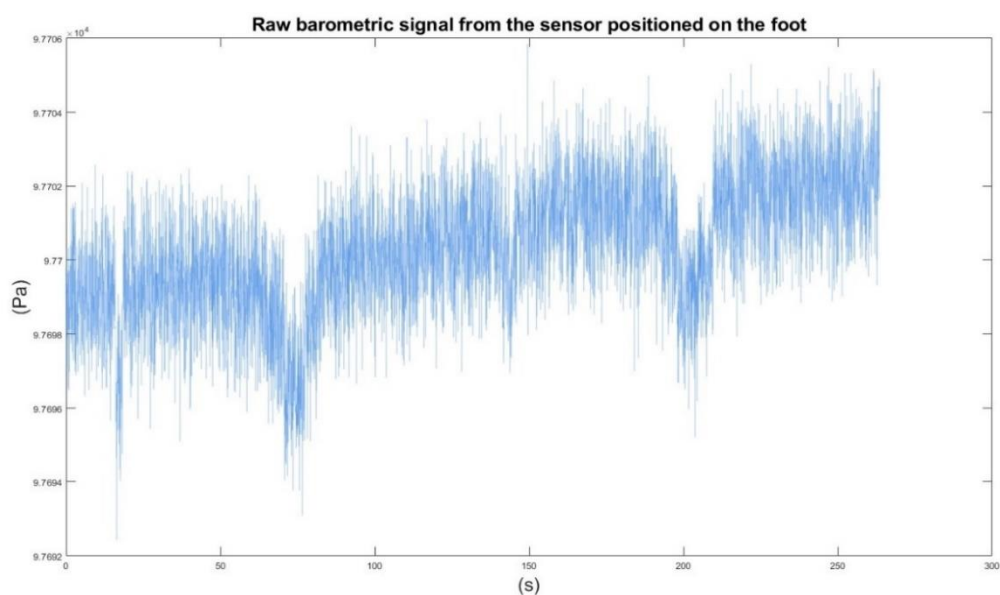


Fig. 54: Raw barometric signal acquired from the barometer located on the foot, during the execution of a trial.

Fig.53 and Fig.54 show an example of the barometric signals extracted from the pelvis and the foot during the execution of a trial acquired in the experimental phase. A common trend is observed in both signals.

Subsequently, the images (Fig. 55 and Fig. 56) show the vertical displacement of the pelvis, in meters, obtained using respectively the single sensor setup and the dual sensor setup as described before. In the latter, the removal of the trend is noticeable.

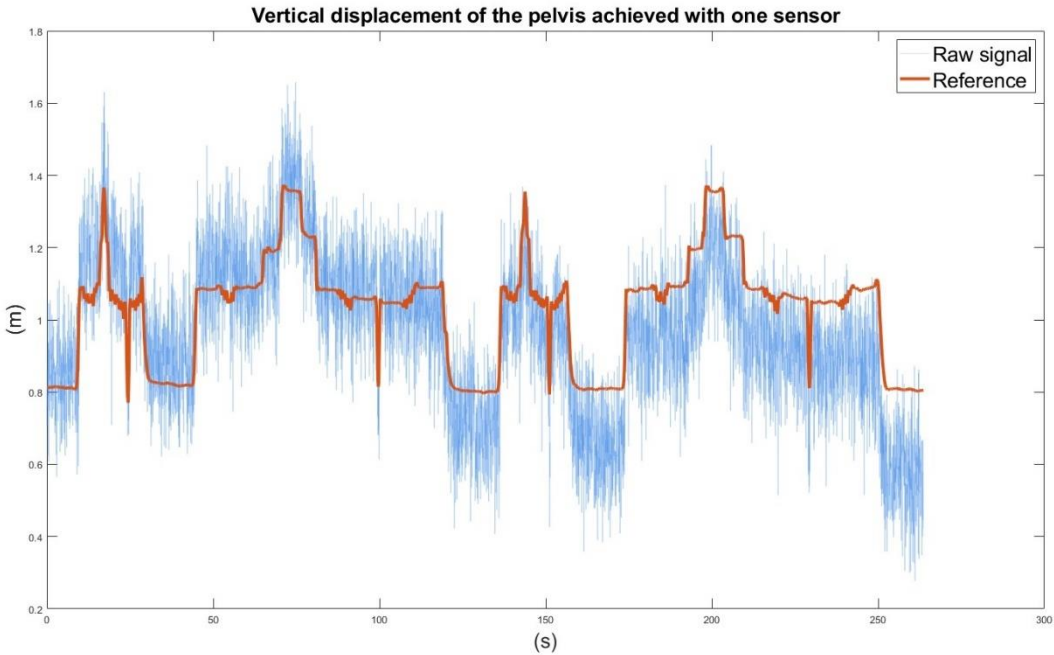


Fig. 55: Vertical displacement of the BCoM through the single sensor set up.

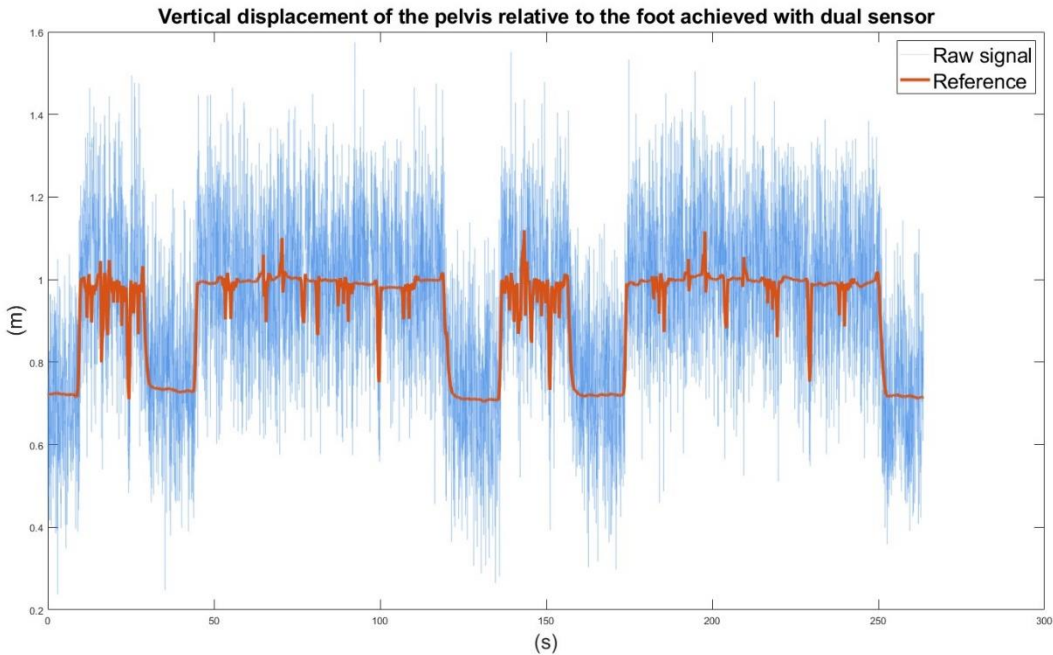


Fig. 56: Vertical displacement of the BCoM through the double sensor set up.

4.3 Barometric signal

The experimental acquisitions were performed with the firmware set to the following configurations (Tab.8):

Sampling frequency f_s	25 Hz
Pressure oversampling	x 16
Temperature oversampling	x 2
IIR filter	/

Tab 8: Firmware setting of BMP390 barometer by Bosch used for experimental acquisitions.

It was decided to remove the onboard low pass filtering in order to implement it manually in Matlab. This approach ensures that the data processing can be reproduced with barometric signals from different pressure sensors.

The barometric signal from the sensor positioned on the pelvis is converted into height using the barometric formula, with the reference pressure P_0 being the pressure of the same sensor at the start of the trial. This provides the height of the pelvis relative to its initial position.

To reduce the presence of the trend in the signal, the Matlab function `detrend` ($detrend(x, n)$) is used, where x is the signal and n indicates the the n th-degree polynomial trend removed. Here, n is set to 2.

The signal is successively filtered replicating the same low pass filtering proposed in the BMP390 datasheet by Bosch, to reconstruct the CoM vertical displacement.

Filter response in the time domain (formula provided in the sensor manual, [39]) (46):

$$y[n] = \frac{y[n-1]*k+x[n]}{k+1} \quad (46)$$

with $k=15$ to reproduce the Indoor Navigation configuration proposed in the datasheet.

Filter response in the Z-transform domain (47,48):

$$Y(Z) = Y(Z) * Z^{-1} * \left(\frac{k}{k+1}\right) + \frac{X(Z)}{k+1} \quad (47)$$

$$H(Z) = \frac{Y(Z)}{X(Z)} = \frac{\frac{1}{1+k}}{1 - \frac{k}{k+1} * Z^{-1}} \quad (48)$$

corresponding to an IIR, all-pole filter with one pole.

Filter response in the frequency domain ($Z \rightarrow e^{j\omega T}$) (49):

$$H(e^{j\omega T}) = \frac{Y(Z)}{X(Z)} = \frac{\frac{1}{1+k}}{1 - \frac{k}{k+1} * e^{-j\omega T}} \quad (49)$$

with j : imaginary unit, ω : angular frequency (rad/s), T : sampling time (0.01s).

Magnitude of the frequency response (50):

$$|H(e^{j\omega T})| = \frac{\frac{1}{1+k}}{\left|1 - \frac{k}{k+1} * e^{-j\omega T}\right|} \quad (50)$$

The cutoff frequency $\omega_{cut-off}$, is sought such that $|H(e^{j\omega T})| = \frac{\sqrt{2}}{2} = -3$ dB. Substituting into the above equation, $f_{cut-off} = 1.016$ Hz.

The filter was constructed in Matlab with parameters $b=1$ and $a=[16,-15]$, and its characteristics were visualized using the *freqz* function (Fig.57).

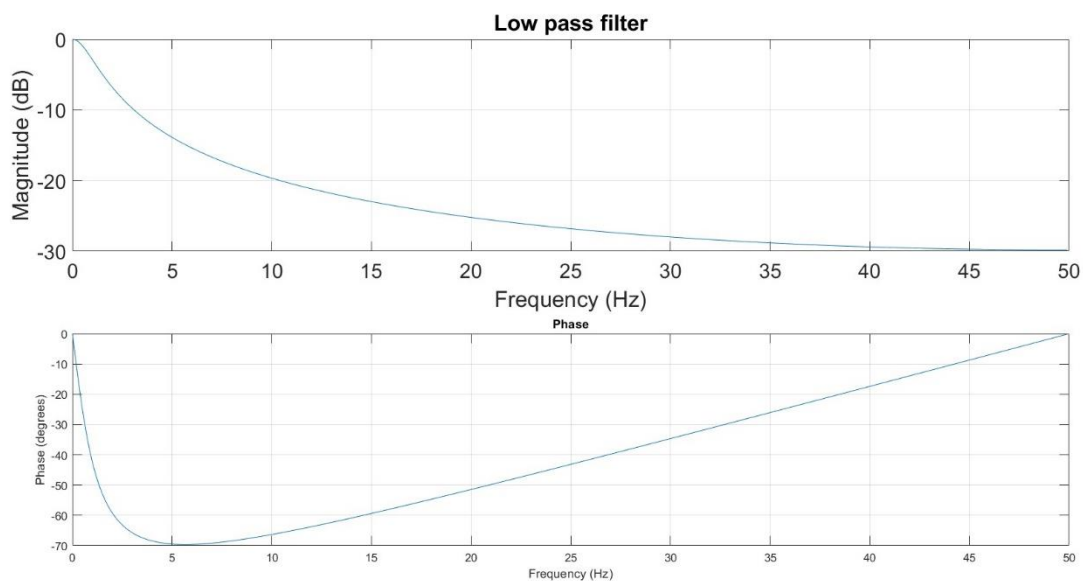


Fig.57: Magnitude and phase of the low-pass filter proposed in the sensor datasheet and reproduced in the data processing.

The following image (Fig.58) shows the original raw signal compared to the processed signal, where the trend has been removed and low-pass filtering has been applied using the previously described filter.

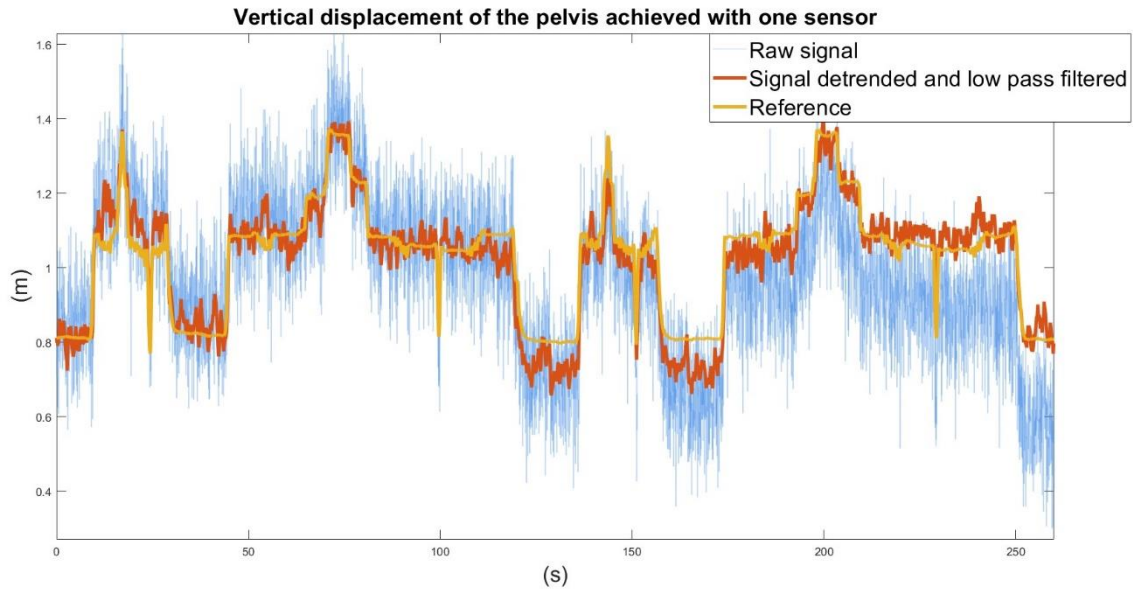


Fig.58: Raw barometric signal compared to the processed one, through the detrending and low pass filtering.

4.4 Algorithms for the detection of transitions

The algorithm for reconstructing the vertical displacement of the CoM assumes that the height of the pelvis remains constant, except during transitions.

In this study, a transition is defined as the time interval during which the CoM experiences vertical displacement, either increasing or decreasing its initial height. Each transition is marked by a start point and an end point, which delineate the period of displacement.

Before and after each transition, the height of the CoM is assumed to be constant.

Specifically, the transitions performed in the acquired experimental trials include sit to stand, at both normal and slow speed, stepping up and down stairs, squats, stand to sit at both normal and slow speed, laying down, and getting up from bed. Sit to stand and stand to sit movements were analyzed under different conditions to evaluate the algorithm's ability to generalize across various motor conditions and to simulate motor difficulties typical of elderly or pathological subjects.

4.4.1 Method based on derivatives

The proposed method for transition detection is based on the first derivative of the barometric signal converted to altitude.

Specifically, the points where the first derivative of a function $f(x)$ equals zero, namely the solutions to the equation $f'(x) = 0$ are candidates for the function's local maxima, minima, i.e., the extremal points, or horizontal inflection points.

To determine whether the points x that nullify the first derivative are maxima, minima or horizontal inflection points, it is necessary to examine the sign of the first derivative. In intervals where the first derivative is positive, the function $f(x)$ is monotonically increasing, whereas in intervals where the first derivative is negative, the function $f(x)$ is monotonically decreasing. Any sign changes in the first derivative at the points where it equals zero determine the nature of these points. For example, $f'(x_1) = 0$:

- If the derivative $f'(x)$ is positive to the left of $x = x_1$ and negative to the right, then $f(x)$ increases to the left of $x = x_1$ and decreases to the right. Consequently, $x = x_1$ is a relative maximum point for the function $f(x)$.
- If the derivative $f'(x)$ is negative to the left of $x = x_1$ and positive to the right, then $f(x)$ decreases to the left of $x = x_1$ and increases to the right. Consequently, $x = x_1$ is a relative minimum point for the function $f(x)$.
- If the derivative $f'(x)$ is negative both to the right and left of $x = x_1$, or positive both to the right and left, then there are no sign changes. Consequently, the function does not exhibit monotonic variations and is classified as a horizontal inflection point.

The peaks of the first derivative correspond to the inflection points of the signal $f(x)$. If $f(x)$ corresponds to the height and $f'(x)$ is the velocity, the inflection points represent the points where, from a biomechanical viewpoint, the acceleration of the transition changes its versus. For example, during the act of sitting, it corresponds to the moment when the subject begins to brake the movement. A positive peak in $f'(x)$ corresponds to the inflection point of a monotonically increasing transition while a negative peak in $f'(x)$ corresponds to the inflection point of a monotonically decreasing transition. The inflection points are the points of interest for the transition identification algorithm because they allow for the identification of transitions in the vertical displacement of the CoM.

$f(x)$: processed height

$f(x)'$: first derivative of the processed height, i. e., velocity

$f(x)' = 0$, maximum, minimum or horizontal inflection points of the height

Sign of $f(x)'$: $\begin{cases} f(x)' > 0, & f(x) \text{ monotonically increasing, transition where height increases} \\ f(x)' < 0, & f(x) \text{ monotonically decreasing, transition where height decreases} \end{cases}$

Peaks of $f(x)'$: inflection points of the height, centre of the corresponding transition

Starting from the barometric signal converted into height, *raw_altitude*, the derivative method exploits two signals:

- *moving_average*: *raw_altitude* filtered with a low-pass filter with a cutoff frequency of 1Hz, replicating the Indoor Navigation configuration proposed by the sensor's datasheet (paragraph 4.3), and further filtered with a moving average filter (window of 200 samples).
- *x_filt*: *raw_altitude* filtered with a low-pass filter with a cutoff frequency of 0.5Hz.

The first derivative of both signals is calculated and further filtered to better highlight the peaks, which are the points of interest to identify transitions.

Using the *findpeaks* function, the peaks (both positive and negative, to identify rising and falling transitions) of the first derivative of the *moving_average* signal are detected, with conditions *MinPeakHeight*=0.0005 and *MinPeakDistance*=400 samples. The value of *MinPeakHeight* was chosen through data tuning using the grid search method, evaluating the sensitivity and precision of the identified transitions.

The *moving_average* signal is highly filtered, which results in a good noise reduction with better transition highlighting but, at the same time, poor temporal reliability. For this reason, once the peaks of the first derivative of the *moving_average* are identified, the focus shifts to finding the corresponding peaks in the first derivative of the *x_filt* signal. This approach enhances temporal resolution. Fig.59 shows the positive and negative peaks of the first derivative signal of the height and the corresponding increasing and decreasing transition in the height.

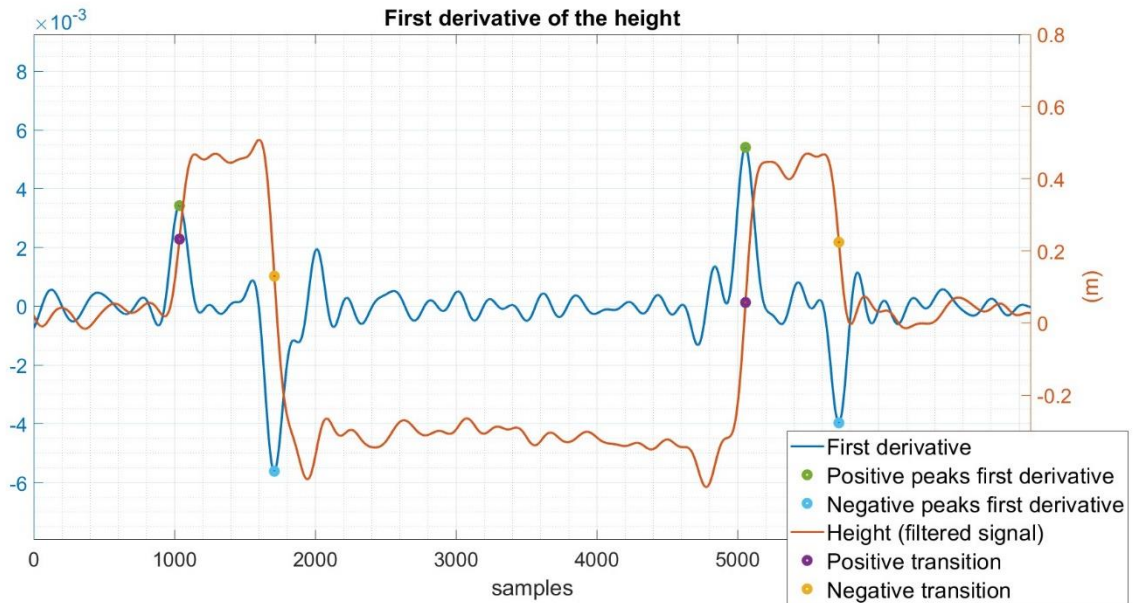


Fig. 59: The figure shows the filtered barometric signal (x_{filt}) and its first derivative. The positive peaks, highlighted in green, and the negative peaks, highlighted in blue, of the first derivative are shown. These peaks correspond to the monotonically increasing transitions (circled in purple) and monotonically decreasing transitions (circled in yellow) of the height, respectively.

In this way, transitions are identified: to define them, it is necessary to find the start and end instants. Analytically, a transition is preceded by a minimum point and followed by a maximum point, where the first derivative of the signal is zero. The start and end points of the transition are therefore identified using the zero-crossing technique, identifying the zero crossings of the first derivative of x_{filt} (Fig.60).

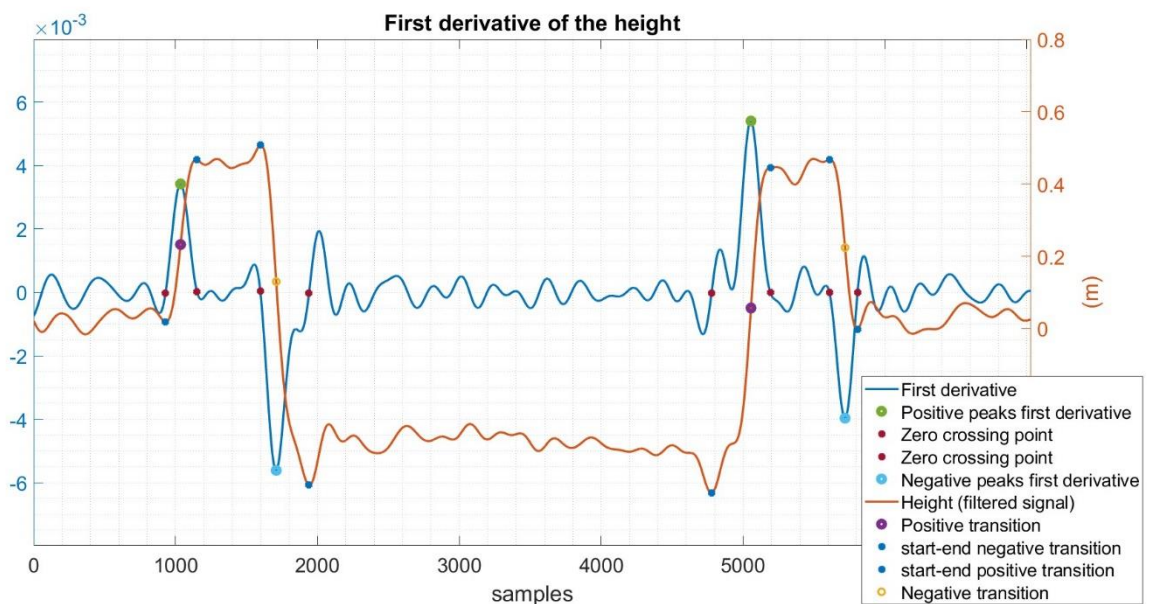


Fig.60: Following the identification of the transitions through the detection of peaks in the first derivative signal, the start and end instants of the transitions are determined using the zero-crossing technique. The zero crossing points are highlighted both in the first derivative signal and in the height signal, as starting and ending points of the transitions.

Finally, a last check is performed to remove transitions erroneously identified and caused by noise (Fig.61).

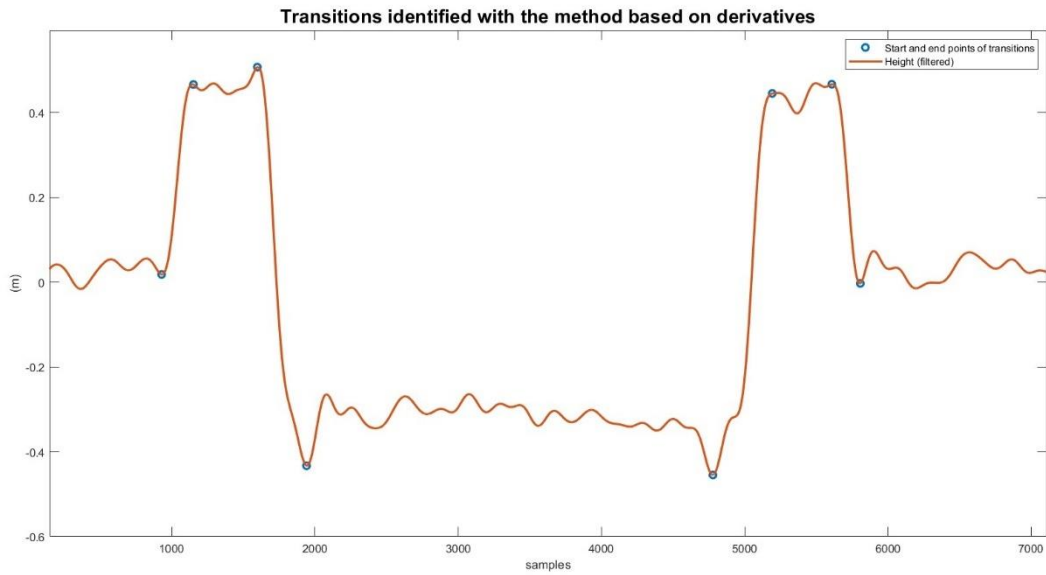


Fig. 61: Final start and end points of transitions identified through the first derivative method.

Using a height threshold of 10 cm, chosen again with the grid search method, transitions where the absolute height difference between the start and end of the transition does not exceed this value are removed. 10 cm is a good compromise between the noise in the barometric signal and the smallest transition that needs to be observed, which is 15 cm for the step.

Due to the diversity of transitions performed, especially the steps associated with a small displacement of the BCoM, the choice of the *MinPeakHeight* threshold is very impactful. Choosing a threshold with a low value facilitates the recognition of transitions, but may result in noise detection and an increase in false positives or extra events. An extra event, in the context of the study, could indicate that the patient is performing more physical activity than they actually are. Conversely, a higher threshold increases precision at the expense of sensitivity, resulting in an increase in missed events. In this case, the patient seems to be performing less physical activity than they actually are.

4.4.2 Manual labelling of stereophotogrammetric signal

To compare the points representing transitions identified using the derivative method, the vertical component of the stereophotogrammetric signal of the pelvis, which is used as a reference for the vertical displacement of the BCoM, is manually labeled. The manual labeling is performed by

indicating the start and end moments of each transition through observation of the signal itself (Fig.62). This approach allows for the evaluation of the performance of the derivative method.

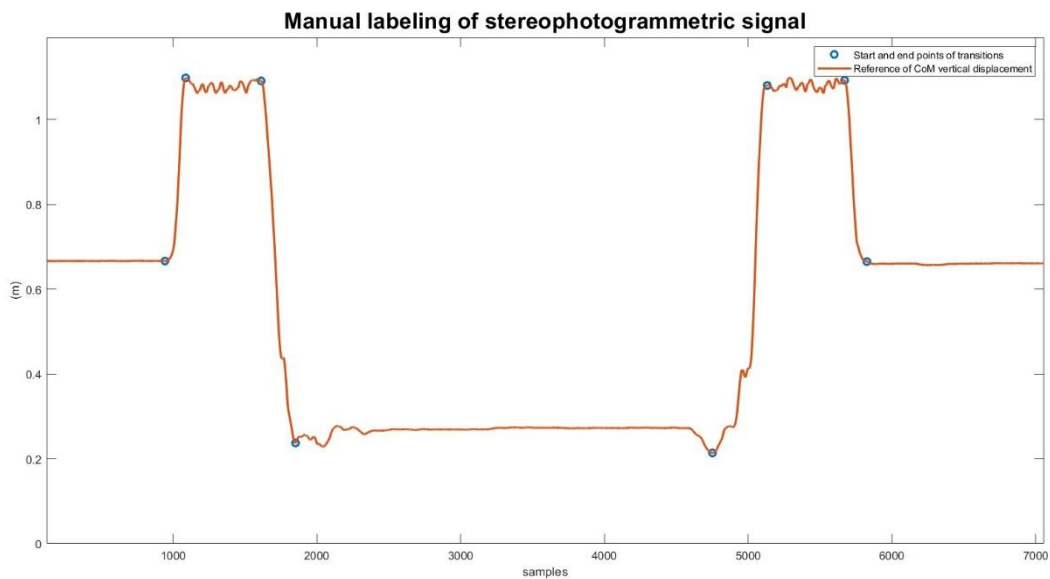


Fig. 62: Manual labeling of stereophotogrammetric signal, by identifying the start and end points of each transition.

4.4.3 Performance evaluation

The points identified using the derivative method are compared with the manually labeled points from the stereophotogrammetric signal. The evaluation of the automatic method is developed by analyzing both the accuracy of transition detection and then the temporal correctness of the correctly identified transitions.

Evaluation of transition detection

The automatically detected points are categorized as follows:

- True Positives (TP), which are the correctly identified points;
- False Positives (FP), which are the incorrectly identified points that do not correspond to a transition.

Additionally, it is possible to identify False Negatives (FN), which are points that the derivative method failed to detect but correspond to a transition.

The number of manually labeled reference points is given by the sum of TP and FN, while the number of automatically detected points is given by the sum of TP and FP.

To evaluate the performance of the proposed method, the following parameters are used (51,52,53):

- 1) $Sensitivity = \frac{TP}{TP+FN} * 100$ (51), representing the number of correctly identified relevant instances divided by the total number of relevant instances that exist;
- 2) $Precision = \frac{TP}{TP+FP} * 100$ (52), representing the number of correctly identified relevant instances divided by the total number of instances identified;
- 3) $F1\ score = \frac{2 * Precision * Sensitivity}{Precision + Sensitivity} * 100$ (53), representing the harmonic mean of precision and recall, providing a balance between these two metrics.

A transition is considered correctly identified if both the start and end times are accurately detected. The true positive transitions are classified based on the type of transition (for Test1: StS, slow StS, laying, and for Test2: StS, squat, and step). For each type of transitions is indicated the sensitivity of transition detection, to highlight the recognition percentage of each group. This classification helps to determine whether the proposed method based on derivatives performs better on specific types of transitions or can generalize and work equally well regardless of the type.

Evaluation of temporal correctness

For the true positive transitions identified, where both the start and end points of the transition are correctly detected, additional parameters are extracted to evaluate the temporal accuracy:

- *Range 10 – 90%*: it is a parameter used to evaluate the duration of a transition by focusing only on its central portion. This means excluding the initial and final phases of the transition and concentrating on the period where the majority of the change occurs. Specifically, it measures the time taken for the transition to progress from 10% to 90% of its total completion, referencing the initial and final heights of the transition in question (Fig.63). By comparing the "10-90% range" values obtained from stereophotogrammetric data (considered as gold standard) with those from the barometric signal, the accuracy of the derivative method in detecting the actual duration of transitions is assessed.

If $h_{end\ stereo}$ is the height reached at the end of a transition and $h_{start\ stereo}$ is the height at the beginning of transition for the reference signal (54,55,56):

$$\Delta_{reference} = h_{end\ stereo} - h_{start\ stereo} \quad (54)$$

$$h_{10\% \ stereo} = \Delta_{reference} \times \frac{1}{10} + h_{start\ stereo} \quad (55)$$

$$h_{90\% \ stereo} = \Delta_{reference} \times \frac{9}{10} + h_{start\ stereo} \quad (56)$$

The samples $t_{10\%stereo}$ and $t_{90\%stereo}$ are found, where the reference height during the transition reaches the values $h_{10\%stereo}$ and $h_{90\%stereo}$ (57).

$$range_{10-90\%stereo} = t_{90\%stereo} - t_{10\%stereo} \quad (57)$$

Similarly, for the barometer (58,59,60,61):

$$\Delta_{baro} = h_{endbaro} - h_{startbaro} \quad (58)$$

$$h_{10\%baro} = \Delta_{baro} \times \frac{1}{10} + h_{startbaro} \quad (59)$$

$$h_{90\%baro} = \Delta_{baro} \times \frac{9}{10} + h_{startbaro} \quad (60)$$

$$range_{10-90\%baro} = t_{90\%baro} - t_{10\%baro} \quad (61)$$

The difference between $range_{10-90\%stereo}$ and $range_{10-90\%baro}$ for each transition provides an indication of the accuracy of the automatic transition's temporal duration.

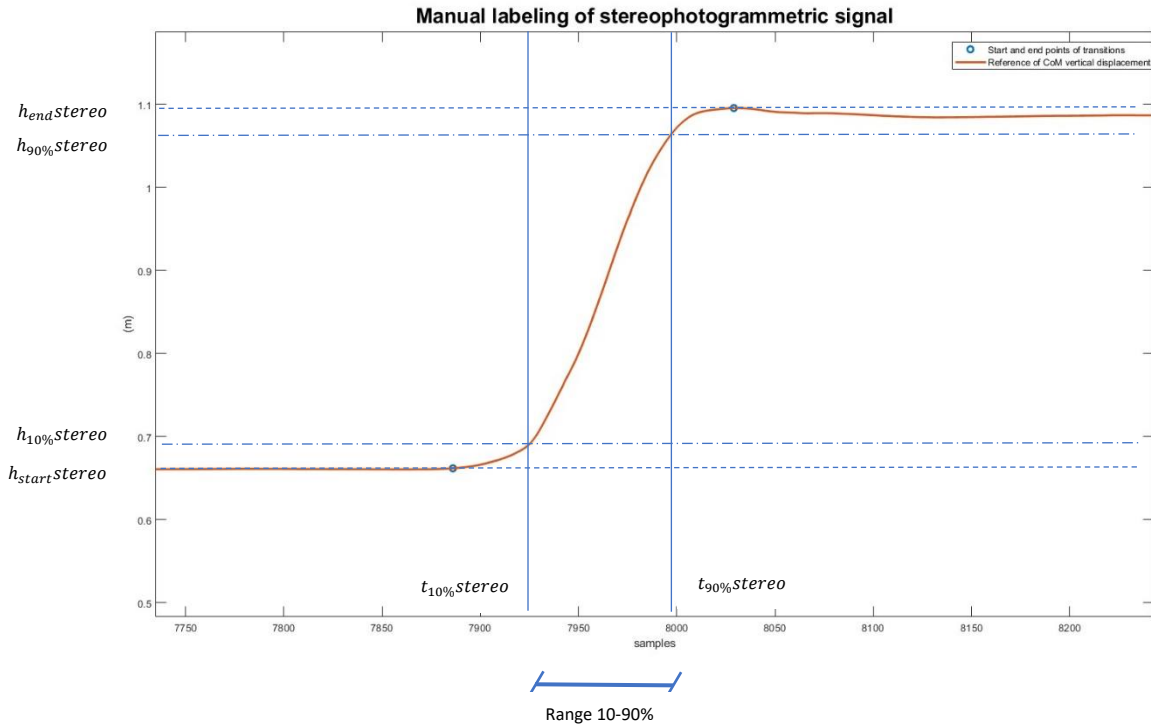


Fig.63: Graphical representation of the 10-90% range for a transition of the stereophotogrammetric signal.

- **50% Range:** it generally refers to the point in time at which half of the transition is completed, with reference to the initial and final heights of the transition in question. By comparing the temporal points where the 50% of a transition is completed, obtained from the stereophotogrammetric data and the barometric data, information on the delay with

which the transition is identified can be obtained (Fig.64) (62,63,64,65).

$$\Delta_{reference} = h_{endstereo} - h_{startstereo} \quad (62)$$

$$h_{50\%stereo} = \Delta_{reference} \times \frac{5}{10} + h_{startstereo} \quad (63)$$

$$\Delta_{baro} = h_{endbaro} - h_{startbaro} \quad (64)$$

$$h_{50\%baro} = \Delta_{baro} \times \frac{5}{10} + h_{startbaro} \quad (65)$$

The samples $t_{50\%stereo}$ and $t_{50\%baro}$ are found, where the reference height and the barometric height during the transition reaches the values $h_{50\%stereo}$ and $h_{50\%baro}$ (66).

$$delay = h_{50\%stereo} - h_{50\%baro} \quad (66)$$

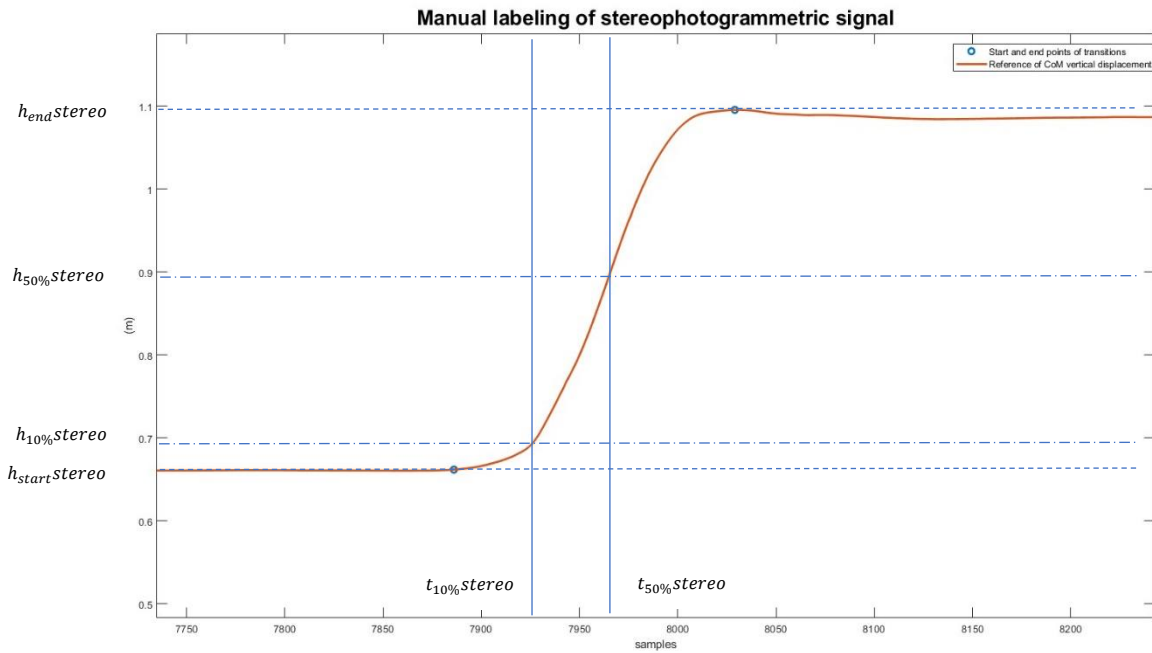


Fig.64: Graphical representation of the point where the 50% of a transition of the stereophotogrammetric signal is completed.

4.5 Algorithms for the tracking of the vertical trajectory of CoM

Following the identification of the transition start and end moments, it is possible to reconstruct the vertical displacement of the Center of Mass. Various approaches are evaluated, including the use of a single barometric sensor placed on the pelvis, the single accelerometer of the IMU located

on the pelvis or the integration of barometric data with accelerometric data from the inertial unit. Outside of the moments when transitions occur, the height is assumed to be constant.

4.5.1 Single-baro approach

To reconstruct the trajectory using a single barometric sensor placed on the pelvis, various methods leveraging different signal characteristics have been explored to determine the most effective tracking approach.

Approach 1

The first approach involves converting the raw barometric signal into altitude (paragraph 3.3.3), using as reference pressure P_0 the one measured at the beginning of the trial from the barometer on the pelvis. Two signals are utilized:

- 1) *baro_detrend*: the raw barometric signal in meters is detrended to remove any long-term drift (Matlab function *detrend(x, n)* with $n=2$).
- 2) *baro_detrend_filt*: the detrended signal is further processed using a low-pass filter with a cutoff frequency $f_t=1\text{Hz}$ to reduce high-frequency noise. The filter is the one proposed by the pressure sensor's datasheet (paragraph 4.3).

Between successive Transitions

Outside the transition periods, the altitude is considered constant. The constant value is determined as the mean of the detrended signal (*baro_detrend*). To mitigate edge effects, the averaging interval spans 200 samples and is centered around the temporal midpoint between the two transitions.

During Transitions

During transitions, the filtered signal (*baro_detrend_filt*) is utilized. This approach allows for precise tracking of the Center of Mass movements by reducing noise while preserving essential signal characteristics.

Initial Height Alignment

The initial height for the trial is obtained from the stereophotogrammetric signal, which is used as a reference to align the reconstructed barometric signal.

Fig.65 illustrates an example of the first approach, demonstrating how the processed barometric data is used to reconstruct the vertical displacement of the BCoM. The present approach leads to errors, in particular peaks, when the final height perceived in a transition is different from the

mean value in the following period. The following image (Fig.65) highlights the described situation.

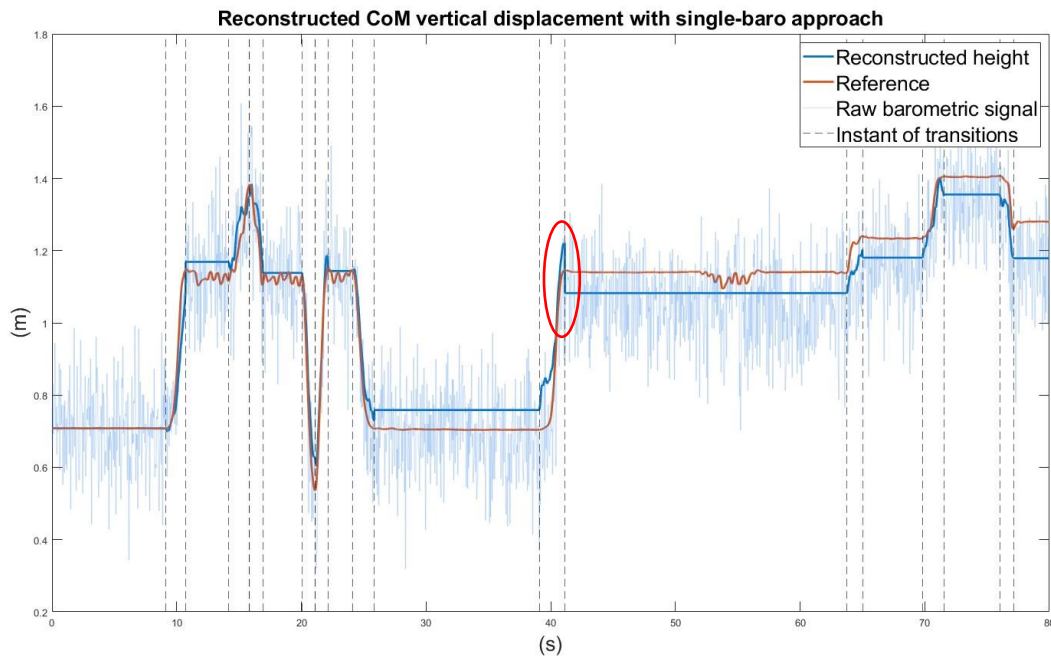


Fig. 65: A comparison between the estimated vertical displacement, reconstructed through the single-baro approach, and the reference, showing the start and end point of transitions. The image highlights a peak that doesn't correspond to a real movement and is due to the fact that the final value reached during the transition does not correspond to the average in the subsequent segment.

Approach 2

This approach tries to correct the presence of peaks in the previous method, leveraging again *baro_detrend* and *baro_detrend_filt* signals, along with the assumption of constant height between two consecutive transitions.

The *baro_detrend_filt* signal is used to estimate the height during a transition. At the end of the transition, the achieved height, denoted as $h_{end\ baro}$, is compared with the average height *avr*, calculated from the *baro_detrend* signal over the interval between the current and the next transition.

Height Comparison and Adjustment

- For increasing transitions (height going up): if $h_{end\ baro}$ is less than *avr*, then $h_{end\ baro}$ is maintained as the constant height until the next transitions. If $h_{end\ baro}$ is higher than *avr*, then *avr* is maintained as the constant height until the next transitions.

- For decreasing transitions (height going down): if $h_{end\ baro}$ is greater than avr , then $h_{end\ baro}$ is maintained as the constant height until the next transitions. If $h_{end\ baro}$ is less than avr , then $h_{end\ baro}$ is maintained as the constant height until the next transitions.

This adjustment ensures that the calculated height at the end of the transition does not exceed the average expected height, thereby preventing unrealistic jumps in the estimated height.

Initial Height Alignment

The initial height for the trial is obtained from the stereophotogrammetric signal, which is used as a reference to align the reconstructed barometric signal.

Fig. 66 illustrates an example of the application of the second approach, demonstrating the effectiveness of the height adjustment mechanism in maintaining realistic height estimations during transitions.

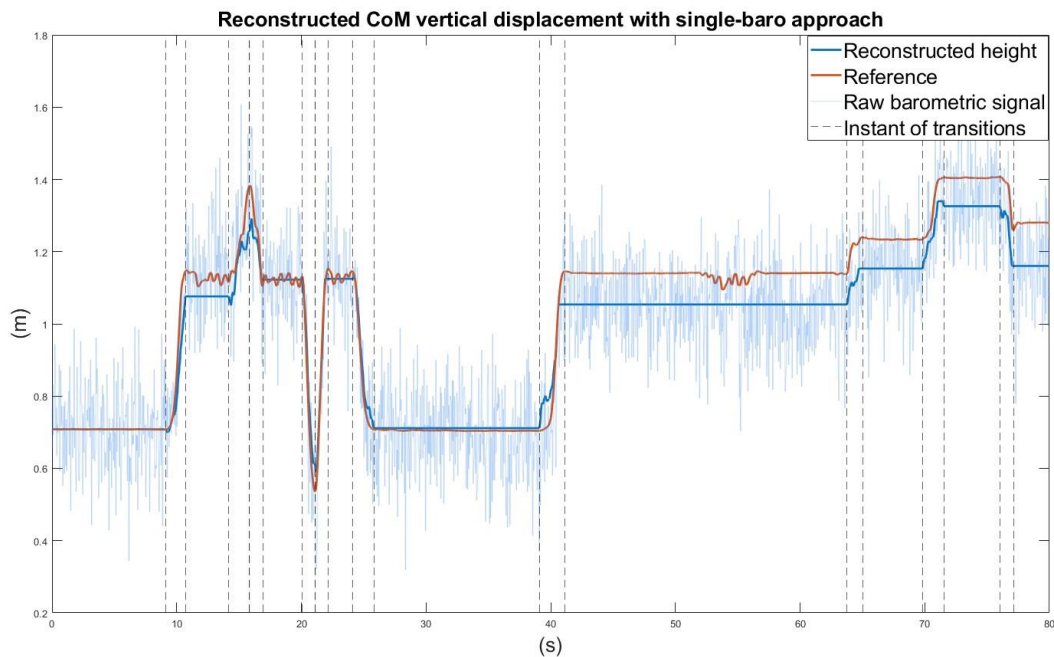


Fig. 66: A comparison between the estimated vertical displacement, reconstructed through the single-baro approach, and the reference, showing the start and end point of transitions.

Approach 3

The third proposed method utilizes two signals:

- 1) *Temperature*: temperature provided by the sensor;
- 2) *baro_detrend_filt*: the raw barometric signal in Pascal is detrended to remove any long-term drift (Matlab function *detrend(x, n)* with $n=2$). The detrended signal is further processed using

a low-pass filter with a cutoff frequency $f_t=1\text{Hz}$ to reduce high-frequency noise. The filter is the one proposed by the pressure sensor's datasheet (paragraph 4.3).

The height of the CoM is considered constant between successive transitions.

During Transition

During transitions, the height is calculated using the barometric formula. Unlike previous methods, the reference pressure P_0 is set to the pressure at the first sample of each transition, rather than the pressure at the start of the trial. This adjustment provides a more accurate and context-specific baseline for height calculation during each transition.

Between successive Transitions

The height at the end of each transition is used as the constant value for the subsequent interval.

Initial Height Alignment

The initial height for the trial is obtained from the stereophotogrammetric signal, which is used as a reference to align the reconstructed barometric signal.

Fig. 67 shows an example of the application of this third approach, highlighting the process and effectiveness of using the raw barometric signal and the adjusted reference pressure for accurate height estimation during transitions.

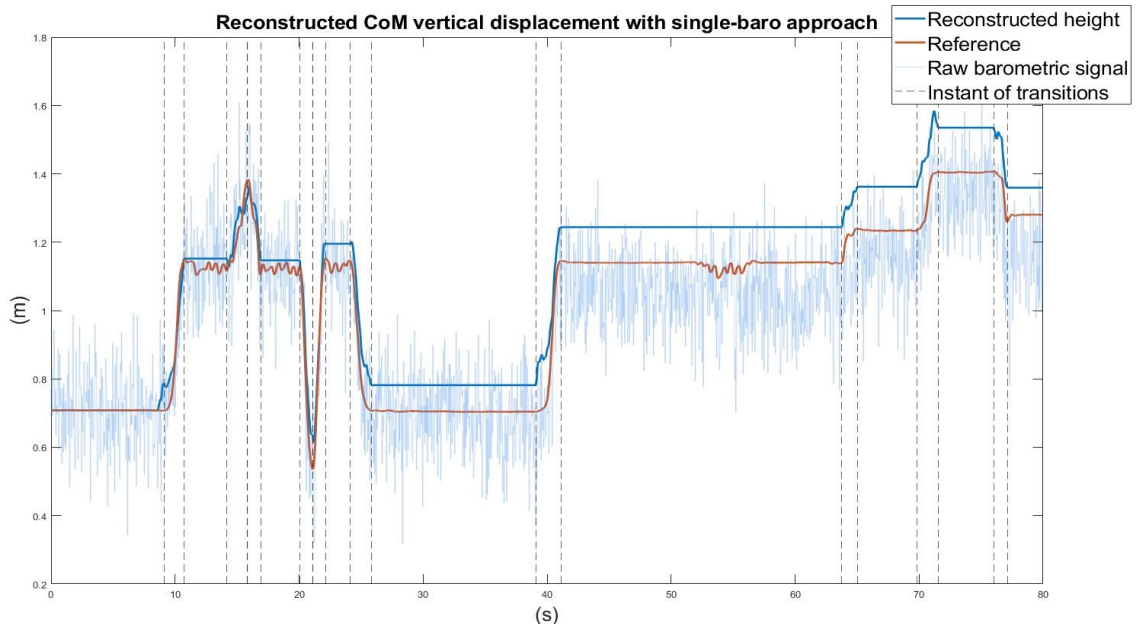


Figure 67 comparison between the estimated vertical displacement, reconstructed through the single-baro approach, and the reference, showing the start and end points of transitions

4.5.2 Dual-baro approach

The approach that utilizes the dual sensor setup with the differential signal, which allows the elimination of the common interference of the two signals and the determination of the pelvis displacement relative to the foot, is not further analyzed in this work. This is because the preference is to develop an algorithm that uses a single sensor, allowing for the direct measurement of pelvis displacement relative to the floor.

4.5.3 IMU-based approach

The trajectory reconstruction algorithm based on the IMU positioned on the pelvis exploits the vertical component of acceleration, a_z . To properly utilize the acceleration data, the Madgwick filter [12] (paragraph 2.2.2.1) is applied to the inertial data obtained from the sensor output.

At the beginning of the trial, the subject is seated in static conditions, which allows for the calculation of the initial orientation of the sensor using the accelerometer as an inclinometer, according to the method proposed by Valenti et al. [42]. The resulting quaternion represents the orientation from the global frame to the local frame of reference. It is necessary to apply the operation of complex conjugation to this quaternion and use the result to initialize the Madgwick filter [19], which then provides the orientation of the local system relative to the global frame.

Using the Madgwick filter, the orientation of the sensor throughout the trial is obtained, allowing for the removal of the gravity component from the acceleration data to acquire the proper acceleration of the sensor. Theoretically, by integrating the vertical component of acceleration, a_z , twice, the displacement along the z-axis can be determined (67,68).

$$v_z(t) = v_0 + \int_{t_0}^{t_1} a_z(t) dt \quad (67)$$

$$z(t) = z_0 + \int_{t_0}^{t_1} v_z(t) dt \quad (68)$$

However, this estimation is affected by drift. It is crucial to recognize that the acceleration cannot be integrated over the entire duration of the trial but only within limited integration intervals where the initial conditions are well-defined. Therefore, the integration intervals correspond to the transition periods $[t_0-t_1]$, where t_0 is the instant of the beginning of the transition and t_1 is the instant of the end of the transition (manually labeled or automatically detected with method based

on derivatives). The conditions for applying double integration are that the subject starts from rest and, after the transition, returns to rest. Within these integration intervals, the following conditions hold:

- $v_z^{t0} = 0 \text{ m/s}$ e $v_z^{t1} = 0 \text{ m/s}$: velocity is zero at both the beginning and end of the integration process. This feature allows for the imposition of both initial and final integration conditions.
- $a_{x,y,z}^{mean} = 0 \text{ m}^2/\text{s}$: As a consequence of the first condition, the mean value of acceleration is null.

The integration is performed using the method proposed by Zok et al. [5], known as Double and Reverse Integration (DRI), which consists of three distinct phases:

(a) Direct Integration: The original signal undergoes double integration with appropriate initial conditions, resulting in a function $d(t)$.

(b) Reverse Integration: The original signal is double integrated inversely in time, treating final conditions as 'initial' conditions, yielding a function $r(t)$.

(c) Weighting: A time-dependent weight function, $w(t)$, ranging from 0 to 1, is employed to balance the combined effects of the two integrated curves. Consequently, the final integrated signal is expressed as (69):

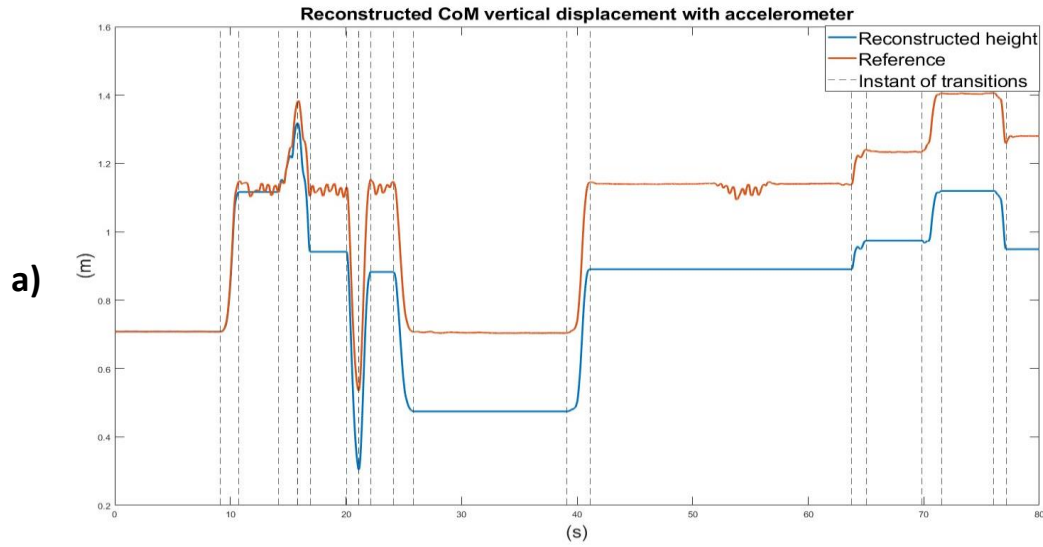
$$DRI(t) = r(t)\omega(t) + d(t)(1 - \omega(t)) \quad (69)$$

This proposed method enables the calculation of velocity, v_{DRI} , from the accelerations through the DRI method. The vertical displacement, $z(t)$, is obtained using the following formula (70):

$$z(t) = \int_{t0}^{t1} v_{DRI}(t) dt \quad (70)$$

The trajectory reconstruction algorithm assumes that the height remains constant between successive transitions. During the transitions, displacement is obtained from the accelerometer using the described method (Fig. 68). Therefore, the integration intervals correspond to the start and end instants of the transition.

The height reached at the end of the transition is then used as a constant value for the next interval, resulting in errors that accumulate over time.



Unlike algorithms based solely on barometric data, the selection of transition points significantly influences the displacement estimation made through the accelerometer. Specifically, a better choice of these points, always in the proximity of the transition, can lead to a considerably improved reconstruction (Fig. 69).

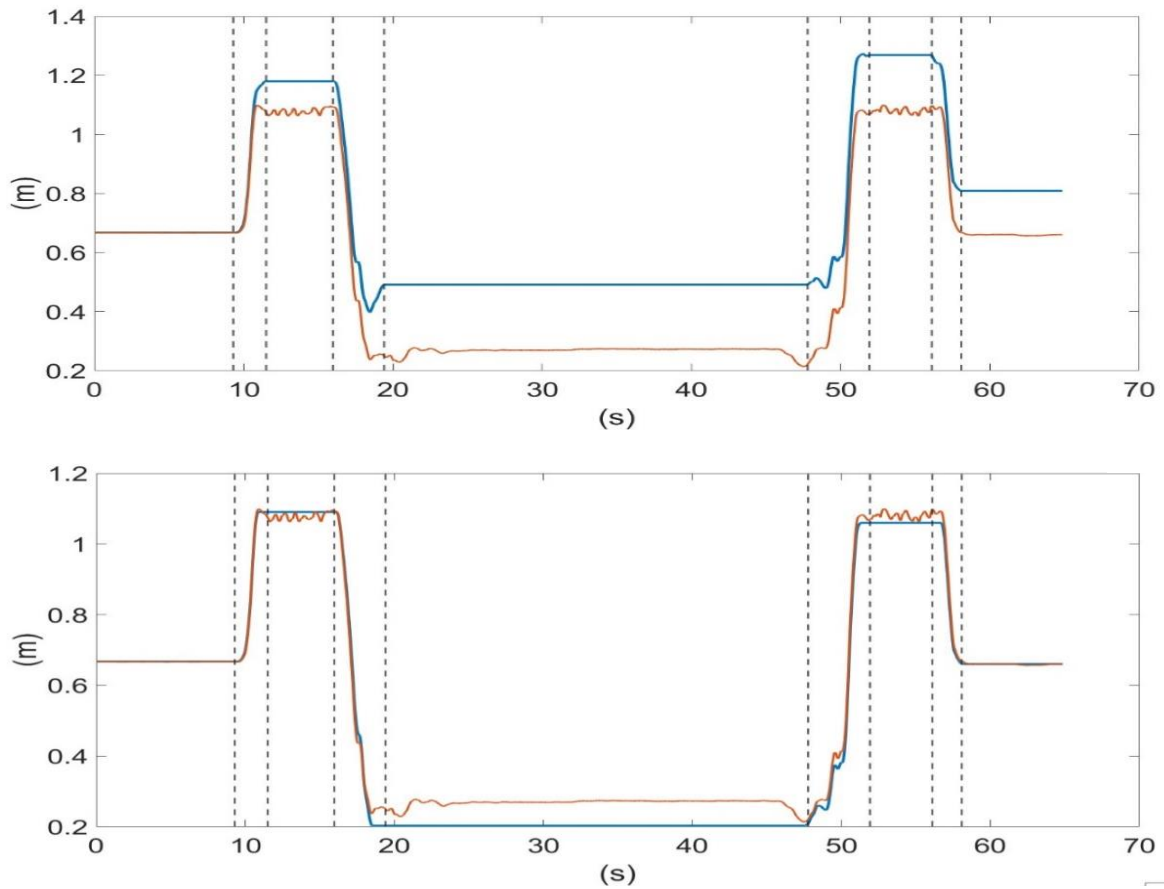


Fig.69: The figure shows the reconstruction of the vertical displacement using the single accelerometer setup. Specifically, image a) contains the accelerometric data integrated twice at the automatically identified transition instants, while image b) contains the accelerometric data integrated twice at the manually identified transition instants. Improving the accuracy of the start and end transition instants significantly

4.5.3 Sensor fusion approach

As detailed in Section 2.3.2, sensor fusion algorithms enable the integration of data from various sensors to enhance the performance beyond what is achievable with individual sensors. In this study, sensor fusion involves combining data from a barometer and an accelerometer. Two sensor fusion methods are evaluated: the Sabatini filter and the Kalman filter.

Both filters depend on parameters that must be optimized. These parameters were fine-tuned through data tuning, using a validation set comprising five subjects, each undergoing two trials. The test set consisted of the remaining 15 subjects, also with two trials each.

The parameter optimization was conducted using the grid search method, a well-established technique for hyperparameter tuning in machine learning models. This method systematically explores multiple combinations of model parameters to identify the optimal set. It involves defining a parameter grid that outlines all possible parameter combinations to be tested and (b) defining an appropriate method for evaluating model performance for each combination.

The model was trained on the validation set to select the optimal parameter values and subsequently evaluated on the test set to assess performance.

The height reconstruction algorithms employing the Kalman filter and the Sabatini filter respectively integrate data from both the barometer and the accelerometer to estimate height during transitions. Between successive transitions, the height is maintained constant at the value achieved at the end of the previous transition.

4.5.4.1 Kalman filter

The implemented Kalman filter [34] employs state variables including altitude h and vertical speed v (71,72):

$$h_{new} = h_{old} + v * \Delta t \quad (71)$$

$$v_{new} = v_{old} + a * \Delta t \quad (72)$$

The prediction phase is represented by the following equations (73):

$$x_{new} = A * x_{old} + B * u \quad (73)$$

$$\mathbf{A} = \begin{bmatrix} 1 & \Delta t \\ 0 & 1 \end{bmatrix}$$

$$\mathbf{B} = \begin{bmatrix} 0.5\Delta t^2 \\ \Delta t \end{bmatrix}$$

u : acceleration measured by the accelerometer.

The measurement model incorporates the barometer measurement z_{baro} , with the measurement matrix $\mathbf{H} = [1 \ 0]$, as only the altitude is directly measured.

The filter initialization includes an estimate of the initial state, the covariance matrix, and the process and measurement noise parameters. The equations for the prediction and update phases are consistent with those detailed in Section 2.3.2. During the prediction phase, the state model and control input (proper acceleration, a_z) are used to predict the current state. Subsequently, barometer measurements are utilized in the update phase of the Kalman filter to refine the estimated state.

The process noise covariance Q and measurement noise covariance R represent the uncertainties associated with the process and measurement models, respectively. Proper determination of these values is crucial, as inappropriate choices can degrade filter performance. R reflects the uncertainty or variance in sensor measurements, which can be estimated through trial measurements. Q , on the other hand, is less deterministic and includes $Q1$, that represents the variance of the noise associated with position, and $Q2$, that represents the variance of the noise associated with velocity. Assuming uncorrelated process noises for position and velocity (74):

$$Q = \begin{bmatrix} Q1^2 & 0 \\ 0 & Q2 \end{bmatrix} \quad (74)$$

The tuning was executed for both Q and R , with the following values for the grid search:

$$Q1 = [0.1:0.1:2];$$

$$Q2 = [1:1:20];$$

$$R = [0.001:0.1:2].$$

Performance evaluation involved analyzing the average absolute error (cm) of the perceived height difference in each transition ($h_{end-transition} - h_{begin-transition}$), using the Kalman filter-based height reconstruction relative to the gold standard ($stereo_{end-transition} -$

$stereo_{begin-transition})$.

The final parameters were:

$$Q = \begin{bmatrix} 5^2 & 0 \\ 0 & 12 \end{bmatrix}$$

$$R = 0.001$$

The mean error for the validation set was 4.94 ± 0.62 cm, and the test set achieved a mean error of 4.55 ± 0.47 cm.

The following image (Fig.70) illustrates an example of height reconstruction using the Kalman filter.

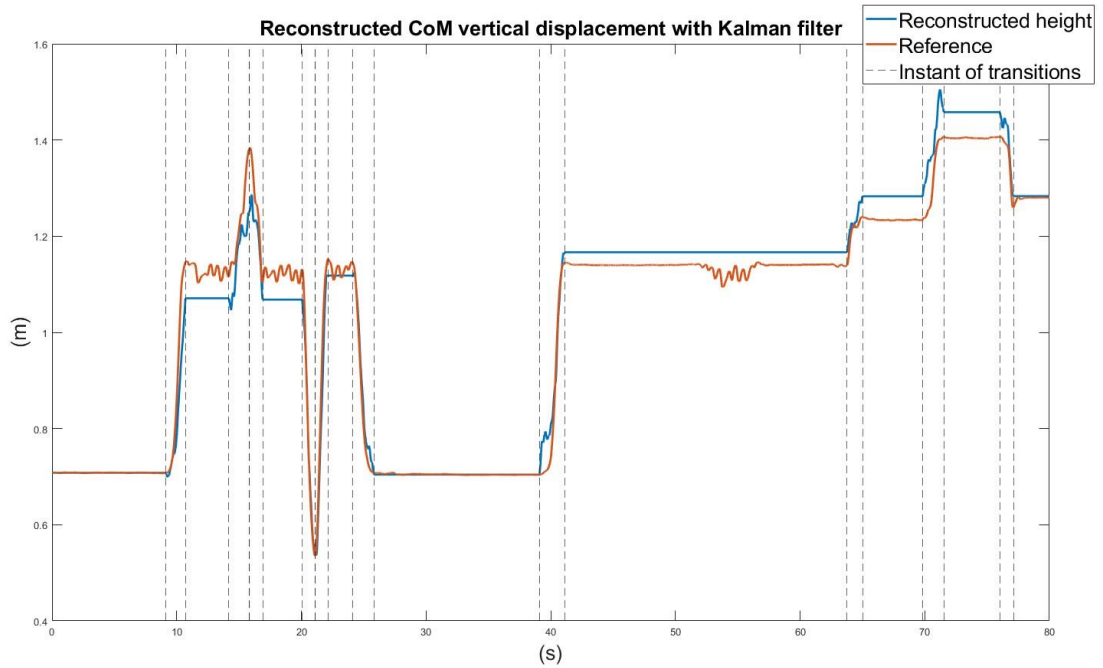


Fig. 70: A comparison between the estimated vertical displacement, reconstructed through the Kalman filter, and the reference, showing the start and end point of transitions.

4.5.4.2 Improved Kalman filter (Sabatini filter)

In the formula presented by Sabatini et al. [30], as cited in Section 2.3.2, σ_w and σ_v represent the weights assigned to the displacement data obtained from the accelerometer and the barometer, respectively, for sensor fusion.

Specifically, σ_w denotes the standard deviation of the acceleration noise $\ddot{x}_{a k}$, and σ_v denotes the noise of the reconstructed height from the barometer $x_{p k}$. These weights provide a measure

of the importance of the two data sources in the final displacement result: the lower the weight, the more significant the source is in the final result.

Performance was evaluated by analyzing the mean absolute error (cm) of the reconstructed height using the Sabatini filter across all trials, with reference to the gold standard.

Parameter tuning was performed for both σ_w and σ_v using the following grid search values:

$$\sigma_w = [0.001:1:5].$$

$$\sigma_v = [1:1:50].$$

The optimal parameters were set to $\sigma_w=0.001$ and $\sigma_v=50$.

The mean error obtained for the validation set was 14.27 ± 1.37 cm, while the test set achieved a mean error of 21.88 ± 0.38 cm.

The following image (Fig.71) illustrates an example of height reconstruction using the Kalman filter.

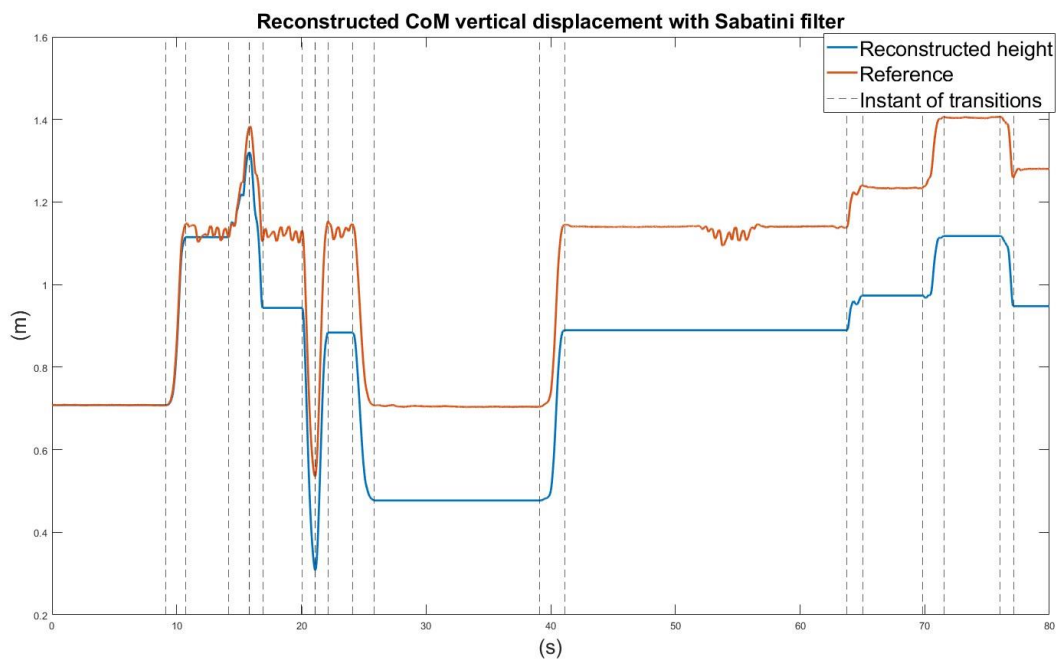


Fig. 71: A comparison between the estimated vertical displacement, reconstructed through the Sabatini filter, and the reference, showing the start and end point of transitions.

4.5.5 Performance evaluation

The reconstruction of the vertical displacement of the CoM through the 6 previously detailed methods (approaches with barometer, approach with accelerometer and sensor fusion via Kalman filter and Sabatini filter) is evaluated against the reference signal, which is the

stereophotogrammetric signal of the pelvis.

The proposed pipeline consists of a sequence of two steps executed in cascade: the detection of transitions and the actual reconstruction of the vertical displacement. Both blocks are necessary to achieve the final goal.

Each block is evaluated separately to analyze the reconstruction of the BCoM without and with the influence of errors present in the transition detection block. Therefore, the height reconstruction is evaluated both by providing the algorithm with manually labelled transitions and by executing the complete pipeline, with the true positive automatic transitions. In the last case, if the transitions are not detected (false negatives) using the derivative method, the reconstruction of CoM displacement is interrupted and resumes at the first subsequently detected transition. If the height reconstruction is interrupted, when it resumes, the initial height value is provided by the barometric signal filtered with a low-pass filter (Fig.72).

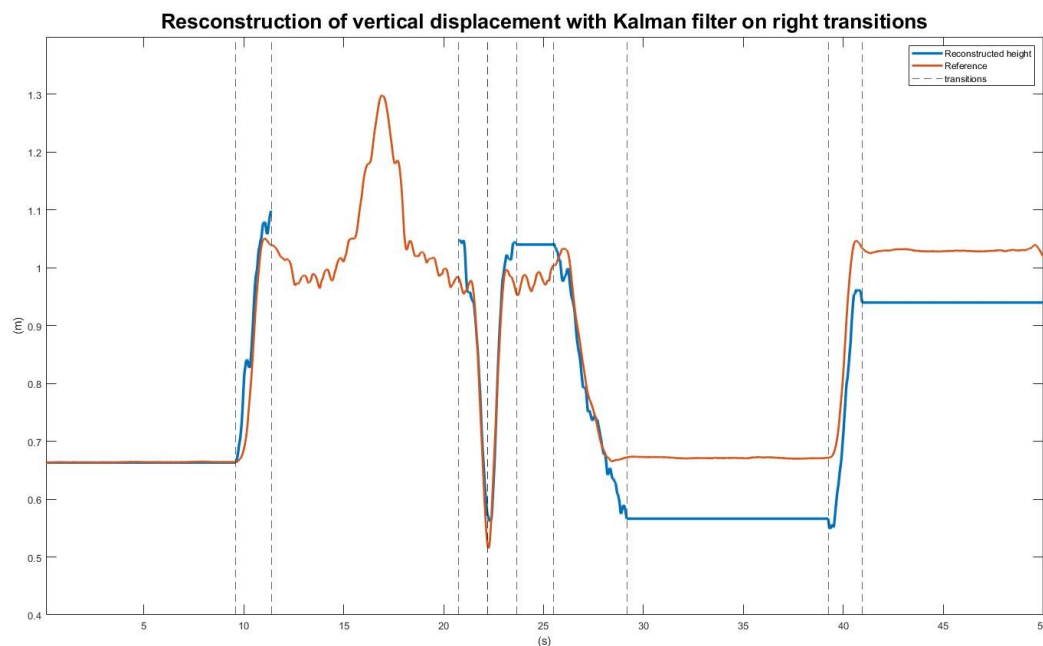


Fig.72: The figure illustrates an example of vertical displacement reconstruction of the CoM using the complete pipeline, specifically through the application of a Kalman filter. The reconstruction is conducted on true positive (TP) transitions, and is interrupted if the transitions are not identified. Upon resumption, the initial value of the signal is derived from the barometric signal filtered with a low-pass filter.

The following performances are calculated for the reconstruction of vertical tracking for both the automatically executed pipeline and the pipeline with manually identified transitions.

If \hat{y} is the reconstructed signal, y is the reference signal, and n is the number of observations

(length of the signals), the vertical displacement reconstructed along each trial is evaluated in terms of (75,76):

$$1) \text{ Root Mean Square (RMSE)} = \sqrt{\frac{\sum_{i=1}^n \|y(i) - \hat{y}(i)\|^2}{n}} \quad (75)$$

$$2) \text{ Mean error} = \frac{\sum_{i=1}^n y(i) - \hat{y}(i)}{n} \quad (76)$$

3) *Correlation coefficient*: it is a statistical measure that describes the strength and direction of the relationship between two variables. It ranges from -1 to 1, where 1 indicates a perfect positive correlation, -1 indicates a perfect negative correlation, and 0 indicates no correlation. The Pearson correlation coefficient measures the linear relationship between two continuous variables. It assumes that both variables are normally distributed and have a linear relationship.

The Spearman correlation coefficient, on the other hand, is a non-parametric measure that assesses how well the relationship between two variables can be described using a monotonic function. It does not assume a linear relationship or normally distributed data, making it suitable for ordinal data or non-linear relationships.

The correlation is evaluated through the Pearson or Spearman coefficient, whether the correlation is linear or not respectively.

Errors in the reconstruction of the vertical displacement of the BCoM can be attributed to the accumulation of errors occurring during the height reconstruction at transitions. Therefore, increasing/decreasing height reconstructed during transitions is also evaluated against the gold standard.

For a given transition, h_{final_stereo} and h_{start_stereo} are the heights of the stereophotogrammetric signal at the beginning and end of the transition, while $h_{final_reconstructed}$ and $h_{start_reconstructed}$ are the final and initial heights of the reconstructed vertical displacement of CoM. The performance is evaluated as follows (77,78,79):

$$\Delta_{reference} = h_{final_stereo} - h_{start_stereo}$$

$$\Delta_{reconstructed} = h_{final_reconstructed} - h_{start_reconstructed}$$

$$1) \text{ Absolute deviation} = \|\Delta_{reference} - \Delta_{reconstructed}\| \quad (77)$$

$$2) \text{ Mean error} = \Delta_{reference} - \Delta_{reconstructed} \quad (78)$$

$$3) \text{ Percentage error} = \frac{\| \Delta_{reference} - \Delta_{reconstructed} \|}{\Delta_{reference}} \quad (79)$$

The mentioned values are specifically calculated for each type of transition (StS, StS slow, Laying, Step, Squat).

4.6 Testing procedure

A statistical analysis was conducted on both the detection of transitions, evaluating the proposed method of derivatives, and height reconstruction.

The statistical analysis needs to be performed on an error distribution. The first step is to determine whether the error distributions are normal or not. This is done using the Shapiro-Wilk test, which helps to establish whether a sample of data comes from a normally distributed population or if it significantly deviates from such a distribution. The test operates under the null hypothesis that the data are normally distributed. If the null hypothesis is rejected, a non-parametric analysis can be performed; otherwise, a parametric analysis is appropriate.

For parametric analysis, the ANOVA test can be used to identify statistically significant differences, whereas for non-parametric analysis, the Kruskal-Wallis test is applied. The null hypothesis in the ANOVA test is that all group means are equal (assuming a normal distribution and homogeneous variances), while in the Kruskal-Wallis test, it is that all group distributions are identical, without making specific assumptions about the data distribution.

For both ANOVA and Kruskal-Wallis analysis, the evaluation parameter is p , and the significance level, α , is set at 0.05 in this work:

- $p \leq 0.05$, if the p -value is less than or equal to the chosen significance level, the null hypothesis can be rejected. This indicates sufficient evidence to support that at least one group has a significantly different distribution from the others.
- $p > 0.05$, if the p -value is greater than the significance level, there is insufficient evidence to reject the null hypothesis. Therefore, it cannot be concluded that there are significant differences between the groups.

In statistical analysis, in the case of multiple comparisons, post hoc correction is necessary, which arises when multiple statistical tests are conducted on the same dataset. This approach is crucial to avoid increasing the likelihood of Type I errors, which occur when the null hypothesis is wrongly rejected. When multiple tests are conducted, even using a standard significance level of

0.05 for each test, the overall probability of obtaining at least one significant result by chance increases with the number of tests.

To manage this risk, post hoc corrections adjust the significance level or the p-values to maintain an acceptable Type I error rate across all tests.

In this study, the Bonferroni Correction was chosen as the post hoc correction method, where the significance level (α) is divided by the total number of tests conducted.

4.6.1 Detection of transitions

The accuracy of the transitions identified using the derivatives method is evaluated through precision, sensitivity, and F1 score. These three values are calculated for each subject and each trial (Trial 1 and Trial 2). Statistical analysis is performed on the F1 score, considering the following divisions:

- Division by test type, evaluating whether there are significantly different error distributions between two groups, Test 1 and Test 2. Each group is characterized by 20 F1 score values, one for each subject.
- Division by subject, evaluating whether there are significantly different error distributions among the 20 subjects. Each group is characterized by two F1 score values.

4.6.2 Tracking of the vertical trajectory of CoM

The tracking of the vertical displacement of the CoM is evaluated both by providing the algorithm with manually labeled transitions and by executing the complete pipeline. For each type of evaluation, performance is calculated for the reconstruction of the trajectory throughout the trial (in terms of RMSE, mean error, and correlation coefficient calculated for each subject and each trial) and for the perceived height difference in each transition, divided by transition type (StS, slow StS, Laying, step, and squat). The following statistical analysis are conducted for both the automatically executed pipeline and the pipeline with manually identified transitions.

Reconstruction of the trajectory throughout the trial

Statistical analysis is performed by evaluating the distribution of RMSE according to the following divisions:

- 1) Fixed one of the six proposed methods (3 approaches with the barometer, accelerometer, sensor fusion with Kalman filter, and sensor fusion with Sabatini filter), classification according to the test type: evaluating whether there are significantly different error distributions between two groups, Test 1 and Test 2. Each group is characterized by 20 RMSE values, one for each subject.
- 2) Fixed one of the six proposed methods (3 approaches with the barometer, accelerometer, sensor fusion with Kalman filter, and sensor fusion with Sabatini filter), classification according to the subject: evaluating whether there are significantly different error distributions between twenty groups, i.e. subjects. Each group is characterized by 2 RMSE values, one for each test (Test 1 and Test 2).
- 3) Classification according to the method: evaluating whether there are significantly different error distributions between the six proposed reconstruction methods (six groups), 3 approaches with the barometer, accelerometer, sensor fusion with Kalman filter, and sensor fusion with Sabatini filter. Each group is characterized by 40 RMSE values, two for each subject (Test 1 and Test 2).

Height Difference During Classified Transitions

For each type of transition, StS, StS slow, laying, step, and squat, the perceived height difference with the proposed algorithm is evaluated against the actual elevation or lowering provided by the stereophotogrammetric signal.

For each subject, the values of absolute deviation, mean error, and percentage error are provided for StS, StS slow, laying, step, and squat manually labeled or automatically detected. Statistical analysis is performed on the absolute deviation, evaluating the following division:

- 1) Fixed one of the six proposed methods (3 approaches with the barometer, accelerometer, sensor fusion with Kalman filter, and sensor fusion with Sabatini filter), classification according to the type of transition: evaluating whether there are significantly different error distributions between 5 groups, StS, slow StS, Laying, step, and squat.
- 2) Classification according to the reconstruction method: evaluating whether there are significantly different error distributions between 6 groups (3 approaches with the barometer, accelerometer, sensor fusion with Kalman filter, and sensor fusion with

Sabatini filter), on the absolute deviation for the transitions StS, slow StS, Laying, step, and squat. Each group is characterized by a different number of errors in case of automatic pipeline and pipeline with manual transitions, respectively a total of 705 and 874 transitions.

5. Results

5.1 Detection of transitions

The proposed method for transitions detection, based on the first derivative of the barometric signal (converted to altitude), is compared with the manual labeling of the stereophotogrammetric signal, used as reference. Precision, sensitivity, and F1-score are calculated for each subject and each test (Test 1 and Test 2). The following table (Tab. 9) shows the (mean values \pm standard deviation) % of precision, sensitivity, and F1 score for all subjects during Test 1, Test 2 and overall. The (average values \pm standard deviation) % F1-score, sensitivity and precision calculated over both Test 1 and Test 2 are reported for each subject as a bar diagram (Fig.72).

<i>(%)</i>	<i>Precision</i>	<i>Sensitivity</i>	<i>F1 score</i>
<i>Test 1</i>	97.28 \pm 4.05	99.68 \pm 1.39	98.42 \pm 2.13
<i>Test 2</i>	98.28 \pm 2.76	69.96 \pm 8.23	81.48 \pm 6.21
<i>Test 1 and Test 2</i>	97.78 \pm 3.46	84.82 \pm 16.14	89.95 \pm 9.73

Tab.9: Evaluation of detection of transitions through the method based on derivatives with (mean values \pm standard deviations) % of precision, sensitivity, and F1 score calculated for all subjects, both separated by Test 1 and Test 2 and combined.

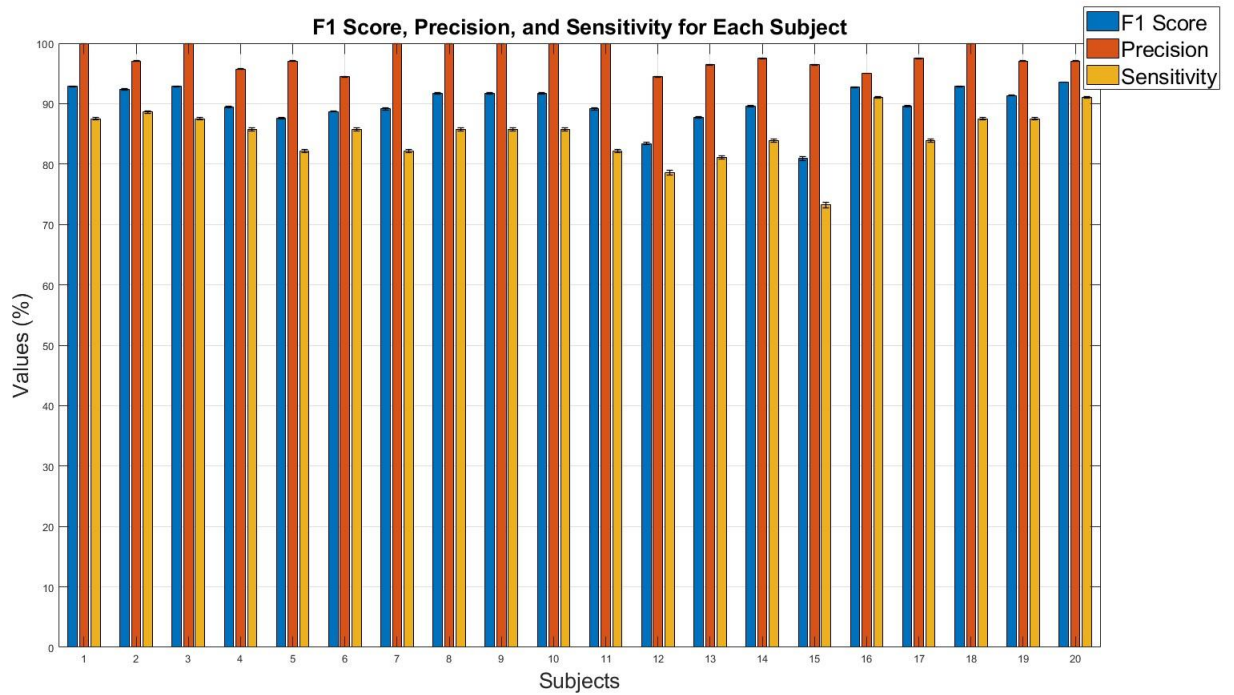


Fig. 72: Bar diagram to summarize the transition detection with (average values \pm standard deviations) % between Test 1 and Test 2 for F1 score, sensitivity and precision for each subject.

The correctly identified transitions, for which both the start and end points are detected, are classified based on their type (for Test 1: StS, StS slow, laying, and for Test 2: StS, squat, and step) and quantified by (mean values \pm standard deviations) % of sensitivity for each type of transition (Tab. 10).

(%)	<i>Sensitivity</i>
<i>Sit to Stand</i>	99.06 ± 4.37
<i>Sit to Stand (slow)</i>	98.75 ± 5.59
<i>Laying</i>	100 ± 0.00
<i>Step</i>	60.00 ± 13.68
<i>Squat</i>	55.63 ± 33.56

Tab.10: Evaluation of correctly identified transitions divided by transitions type.

A transition is correctly identified when both the start and end points are true positive, thus the temporal accuracy is evaluated in terms of delay, calculated between centroids of transitions, and the 10-90% range to assess the overall duration. Since the temporal performance are calculated by subtracting the value obtained by the proposed method from the reference value, a negative delay indicates that the barometric signal is delayed with respect to the stereo label, while a positive value indicates an advance in the barometric signal compared to stereophotogrammetry. Similarly, a negative error between transition durations indicates that the method overestimated the real duration for that transition. Table (Tab. 11) shows the (mean values \pm standard deviations) *ms* of delay and range 10-90% calculated for all subjects, both separated by Test 1 and Test 2 and combined. The scatter plot (Fig.73) highlights the actual versus predicted values of range 10-90% for transitions duration.

<i>(ms)</i>	<i>Delay</i>	<i>Range 10-90%</i>
<i>Test 1</i>	-11 ± 9	-35 ± 440
<i>Test 2</i>	-13 ± 6	-440 ± 120
<i>Test 1 and Test 2</i>	-12 ± 7	-240 ± 380

Tab.11: Temporal accuracy of correctly identified transitions assessed with (mean values \pm standard deviations) *ms* of delay and range 10-90% calculated for all subjects, both separated by Test 1 and Test 2 and combined.

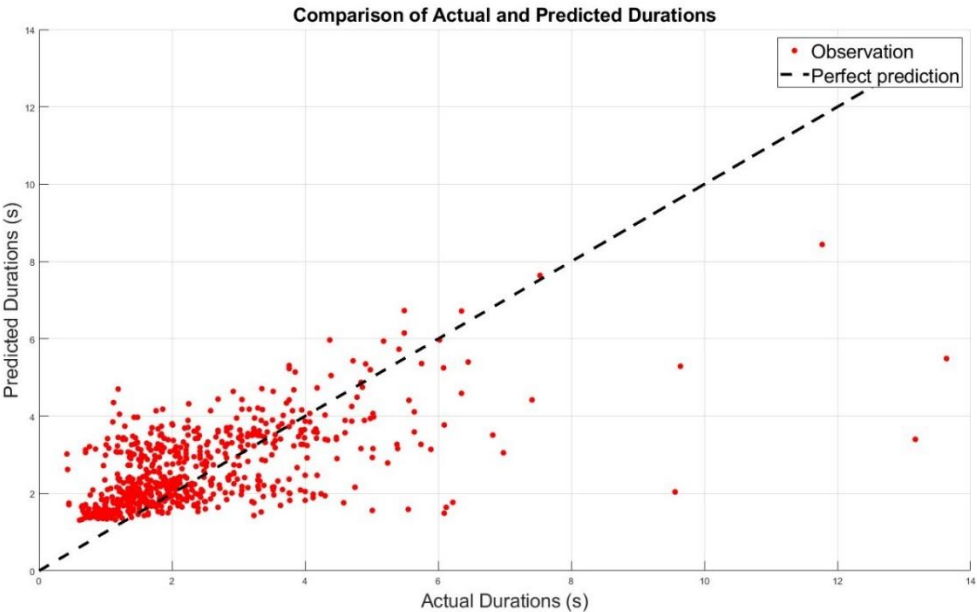


Fig. 72: Scatter plot of the predicted durations estimated by the first derivative method and the actual durations of transitions, to access and evaluate the correctness.

5.2 Tracking of the vertical trajectory of the CoM

Manually labeled transition

To evaluate the reconstruction of the vertical displacement of the CoM, which is based on two cascading steps (detection of transitions and the actual reconstruction of height using a single barometer, a single accelerometer or sensor fusion), the influence of these two is evaluated separately. Below are the results of the reconstruction of the vertical displacement obtained by providing manually labeled transition instances.

Specifically, for each method, the (mean value \pm standard deviation) of RMSE, mean error, and correlation coefficient across 20 subjects are reported for Test 1 and Test 2 separately and then considered together (Tab.12, Tab.13, Tab.14, Tab.15, Tab.16, Tab.17).

Kalman filter

	<i>RMSE (cm)</i>	<i>Mean error (cm)</i>	<i>Correlation coefficient</i>
<i>Test 1</i>	18 \pm 11	6 \pm 18	0.96 \pm 0.03
<i>Test 2</i>	12 \pm 6	5 \pm 1	0.92 \pm 0.04
<i>Test 1 and Test 2</i>	15 \pm 9	5 \pm 14	0.94 \pm 0.04

Tab.12: Reconstruction of CoM vertical displacement with Kalman filter evaluated with (mean values \pm standard deviations) cm of RMSE, mean error, and correlation coefficient across 20 subjects reported for Test 1 and Test 2 separately and then considered together.

Barometer (approach 1)

	<i>RMSE (cm)</i>	<i>Mean error (cm)</i>	<i>Correlation coefficient</i>
<i>Test 1</i>	11 \pm 4	7 \pm 5	0.97 \pm 0.01
<i>Test 2</i>	10 \pm 4	8 \pm 5	0.94 \pm 0.02
<i>Test 1 and Test 2</i>	11 \pm 4	7 \pm 5	0.96 \pm 0.02

Tab.13: Reconstruction of CoM vertical displacement with barometer (approach 1) evaluated with (mean values \pm standard deviations) cm of RMSE, mean error, and correlation coefficient across 20 subjects reported for Test 1 and Test 2 separately and then considered together.

Barometer (approach 2)

	<i>RMSE (cm)</i>	<i>Mean error (cm)</i>	<i>Correlation coefficient</i>
<i>Test 1</i>	9 ± 3	7 ± 4	0.98 ± 0.01
<i>Test 2</i>	11 ± 4	8 ± 5	0.93 ± 0.03
<i>Test 1 and Test 2</i>	10 ± 4	7 ± 4	0.96 ± 0.03

Tab.14: Reconstruction of CoM vertical displacement with barometer (approach 2) evaluated with (mean values ± standard deviations) cm of RMSE, mean error, and correlation coefficient across 20 subjects reported for Test 1 and Test 2 separately and then considered together.

Barometer (approach 3)

	<i>RMSE (cm)</i>	<i>Mean error (cm)</i>	<i>Correlation coefficient</i>
<i>Test 1</i>	18 ± 11	5 ± 11	0.96 ± 0.03
<i>Test 2</i>	12 ± 7	5 ± 18	0.92 ± 0.04
<i>Test 1 and Test 2</i>	15 ± 9	5 ± 15	0.94 ± 0.04

Tab.15: Reconstruction of CoM vertical displacement with barometer (approach 3) evaluated with (mean values ± standard deviations) cm of RMSE, mean error, and correlation coefficient across 20 subjects reported for Test 1 and Test 2 separately and then considered together.

Sabatini filter

	<i>RMSE (cm)</i>	<i>Mean error (cm)</i>	<i>Correlation coefficient</i>
<i>Test 1</i>	35 ± 23	1 ± 36	0.85 ± 0.11
<i>Test 2</i>	28 ± 17	-7 ± 28	0.76 ± 0.22
<i>Test 1 and Test 2</i>	31 ± 20	-3 ± 32	0.80 ± 0.18

Tab.16: Reconstruction of CoM vertical displacement with Sabatini filter evaluated with (mean values ± standard deviations) cm of RMSE, mean error, and correlation coefficient across 20 subjects reported for Test 1 and Test 2 separately and then considered together.

Accelerometer

	<i>RMSE (cm)</i>	<i>Mean error (cm)</i>	<i>Correlation coefficient</i>
<i>Test 1</i>	35 ± 23	1 ± 37	0.84 ± 0.12
<i>Test 2</i>	28 ± 17	-8 ± 28	0.75 ± 0.22
<i>Test 1 and Test 2</i>	31 ± 20	-4 ± 32	0.80 ± 0.18

Tab.17: Reconstruction of CoM vertical displacement with the accelerometer evaluated with (mean values ± standard deviations) cm of RMSE, mean error, and correlation coefficient across 20 subjects reported for Test 1 and Test 2 separately and then considered together.

The height difference in each transition relative to the actual displacement is evaluated. The results are categorized by type of transition, providing the (mean value ± standard deviation) cm of the absolute deviation, mean error, and percentage error (Tab.18, Tab.19, Tab.20, Tab.21, Tab.22, Tab.23).

Sabatini filter

	<i>StS</i>	<i>StS slow</i>	<i>Laying</i>	<i>Step</i>	<i>Squat</i>
<i>Absolute deviation (cm)</i>	4.5 ± 4.1	4.7 ± 3.8	13 ± 12	6.4 ± 7.5	4.9 ± 5.6
<i>Mean error (cm)</i>	1.9 ± 5.8	1.4 ± 5.9	7.5 ± 16	-0.68 ± 9.9	-0.27 ± 7.5
<i>Percentage error (%)</i>	13 ± 12	14 ± 14	16 ± 14	28 ± 28	12 ± 14

Tab.18: Height differences for each type of transition relative to the actual displacement performed with the Sabatini filter evaluated with the (mean values ± standard deviations) cm of absolute deviation, mean error, and percentage error across 20 subjects.

Kalman filter

	<i>StS</i>	<i>StS slow</i>	<i>Laying</i>	<i>Step</i>	<i>Squat</i>
Absolute deviation (cm)	3.9 ± 2.8	4.1 ± 2.6	4.3 ± 3.5	5.3 ± 4.0	6.9 ± 5.3
Mean error (cm)	2.3 ± 4.2	1.0 ± 4.8	1.1 ± 5.5	4.8 ± 4.6	6.4 ± 5.8
Percentage error (%)	11 ± 8	11 ± 7	5 ± 4	25 ± 18	17 ± 13

Tab.19: Height differences for each type of transition relative to the actual displacement performed with the Kalman filter evaluated with the (mean values ± standard deviations) cm of absolute deviation, mean error, and percentage error across 20 subjects.

Barometer (approach 1)

	<i>StS</i>	<i>StS slow</i>	<i>Laying</i>	<i>Step</i>	<i>Squat</i>
Absolute deviation (cm)	3.5 ± 3.1	4.0 ± 2.9	4.1 ± 4.1	5.5 ± 3.9	7.3 ± 4.7
Mean error (cm)	0.2 ± 4.6	0.7 ± 4.9	-0.20 ± 5.7	4.4 ± 5.1	6.7 ± 5.5
Percentage error (%)	10 ± 8	12 ± 8	5 ± 5	27 ± 19	19 ± 13

Tab.20: Height differences for each type of transition relative to the actual displacement performed with the barometer (approach 1) evaluated with the (mean values ± standard deviations) cm of absolute deviation, mean error, and percentage error across 20 subjects.

Barometer (approach 2)

	<i>StS</i>	<i>StS slow</i>	<i>Laying</i>	<i>Step</i>	<i>Squat</i>
Absolute deviation (cm)	4.8 ± 4.2	5.1 ± 3.5	5.8 ± 4.2	6.6 ± 5.7	9.0 ± 6.5
Mean error (cm)	4.5 ± 4.1	4.3 ± 4.4	5.3 ± 4.9	6.5 ± 5.8	8.7 ± 6.9
Percentage error (%)	14 ± 12	15 ± 10	7 ± 5	31 ± 21	23 ± 15

Tab.21: Height differences for each type of transition relative to the actual displacement performed with the barometer evaluated with the (mean values ± standard deviations) cm of absolute deviation, mean error, and percentage error across 20 subjects.

Barometer (approach 3)

	<i>StS</i>	<i>StS slow</i>	<i>Laying</i>	<i>Step</i>	<i>Squat</i>
<i>Absolute deviation (cm)</i>	3.8 ± 2.8	4.0 ± 2.6	4.3 ± 3.4	5.3 ± 4.0	6.8 ± 5.1
<i>Mean error (cm)</i>	2.2 ± 4.2	1.0 ± 4.8	0.9 ± 5.5	4.8 ± 4.6	6.2 ± 5.8
<i>Percentage error (%)</i>	11 ± 8	11 ± 8	5 ± 4	25 ± 19	17 ± 12

Tab.22: Height differences for each type of transition relative to the actual displacement performed with the barometer (approach 3) evaluated with the (mean values ± standard deviations) cm of absolute deviation, mean error, and percentage error across 20 subjects.

Accelerometer

	<i>StS</i>	<i>StS slow</i>	<i>Laying</i>	<i>Step</i>	<i>Squat</i>
<i>Absolute deviation (cm)</i>	4.5 ± 4.2	4.6 ± 3.7	13 ± 12	6.4 ± 7.5	5.0 ± 5.6
<i>Mean error (cm)</i>	1.9 ± 5.9	1.4 ± 5.7	7.7 ± 16	0.9 ± 9.8	-0.47 ± 7.5
<i>Percentage error (%)</i>	13 ± 13	14 ± 14	16 ± 15	29 ± 28	13 ± 14

Tab.23: Height differences for each type of transition relative to the actual displacement performed with the barometer (approach 2) evaluated with the (mean values ± standard deviations) cm of absolute deviation, mean error, and percentage error across 20 subjects.

Automatic transition

The same results are provided by executing the complete pipeline and supplying the algorithm with the true positive transitions identified using the derivative method. If the transitions are not identified, the height reconstruction is halted. Therefore, the results are based on the reconstructed segments.

The (mean value ± standard deviation) cm of RMSE, mean error, and correlation coefficient across 20 subjects are reported for Test 1 and Test 2 separately and then considered together (Tab.24, Tab.25, Tab.26, Tab.27, Tab.28, Tab.29).

Kalman filter

	<i>RMSE (cm)</i>	<i>Mean error (cm)</i>	<i>Correlation coefficient</i>
Test 1	24 ± 7	0 ± 24	0.93 ± 0.05
Test 2	14 ± 14	9 ± 10	0.93 ± 0.05
Test 1 and Test 2	19 ± 12	5 ± 19	0.93 ± 0.05

Tab.24: Reconstruction of CoM vertical displacement with Kalman filter evaluated with (mean values ± standard deviations) cm of RMSE, mean error, and correlation coefficient across 20 subjects reported for Test 1 and Test 2 separately and then considered together.

Barometer (approach 1)

	<i>RMSE (m)</i>	<i>Mean error (m)</i>	<i>Correlation coefficient</i>
Test 1	9 ± 3	5 ± 4	0.98 ± 0.01
Test 2	8 ± 4	3 ± 4	0.93 ± 0.06
Test 1 and Test 2	9 ± 3	4 ± 4	0.96 ± 0.05

Tab.25: Reconstruction of CoM vertical displacement with barometer (approach 1) evaluated with (mean values ± standard deviations) cm of RMSE, mean error, and correlation coefficient across 20 subjects reported for Test 1 and Test 2 separately and then considered together.

Barometer (approach 2)

	<i>RMSE (cm)</i>	<i>Mean error (cm)</i>	<i>Correlation coefficient</i>
Test 1	9 ± 2	6 ± 4	0.98 ± 0.01
Test 2	6 ± 3	2 ± 3	0.97 ± 0.02
Test 1 and Test 2	8 ± 3	4 ± 4	0.97 ± 0.02

Tab. 26: Reconstruction of CoM vertical displacement with barometer (approach 2) evaluated with (mean values ± standard deviations) cm of RMSE, mean error, and correlation coefficient across 20 subjects reported for Test 1 and Test 2 separately and then considered together.

Barometer (approach 3)

	<i>RMSE (cm)</i>	<i>Mean error (cm)</i>	<i>Correlation coefficient</i>
<i>Test 1</i>	24 ± 13	-1 ± 24	0.93 ± 0.05
<i>Test 2</i>	9 ± 4	0 ± 5	0.93 ± 0.05
<i>Test 1 and Test 2</i>	17 ± 12	0 ± 17	0.93 ± 0.05

Tab. 27: Reconstruction of CoM vertical displacement with barometer (approach 3) evaluated with (mean values ± standard deviations) cm of RMSE, mean error, and correlation coefficient across 20 subjects reported for Test 1 and Test 2 separately and then considered together.

Sabatini filter

	<i>RMSE (cm)</i>	<i>Mean error (cm)</i>	<i>Correlation coefficient</i>
<i>Test 1</i>	39 ± 23	1 ± 38	0.79 ± 0.24
<i>Test 2</i>	27 ± 11	8 ± 15	0.58 ± 0.15
<i>Test 1 and Test 2</i>	33 ± 19	5 ± 28	0.69 ± 0.23

Tab. 28: Reconstruction of CoM vertical displacement with Sabatini filter evaluated with (mean values ± standard deviations) cm of RMSE, mean error, and correlation coefficient across 20 subjects reported for Test 1 and Test 2 separately and then considered together.

Accelerometer

	<i>RMSE (cm)</i>	<i>Mean error (cm)</i>	<i>Correlation coefficient</i>
<i>Test 1</i>	39 ± 23	1 ± 38	0.80 ± 0.15
<i>Test 2</i>	28 ± 11	8 ± 15	0.58 ± 0.24
<i>Test 1 and Test 2</i>	33 ± 19	5 ± 29	0.69 ± 0.22

Tab. 29: Reconstruction of CoM vertical displacement with accelerometer evaluated with (mean values ± standard deviations) cm of RMSE, mean error, and correlation coefficient across 20 subjects reported for Test 1 and Test 2 separately and then considered together.

The height difference in each transition relative to the actual displacement performed is evaluated. The results are categorized by type of transition, providing the (mean value \pm standard deviation) of the absolute deviation, mean error, and percentage error (Tab.30, Tab.31, Tab.32, Tab.33, Tab.34, Tab.35). Below the scatter plots for each method of reconstructing the vertical displacement of the CoM are reported, showing the perceived and expected values of the height difference associated with all automatically identified transitions (Fig. 73, Fig.74, Fig.75, Fig.76, Fig.77, Fig.78).

Sabatini filter

	<i>StS</i>	<i>StS slow</i>	<i>Laying</i>	<i>Step</i>	<i>Squat</i>
<i>Absolute deviation (cm)</i>	5.8 \pm 6.1	14 \pm 10	13 \pm 13	5.2 \pm 8.6	15 \pm 5.6
<i>Mean error (cm)</i>	0.8 \pm 8.4	11 \pm 14	6.3 \pm 17	-0.11 \pm 10	-1.6 \pm 18
<i>Percentage error (%)</i>	17 \pm 19	42 \pm 32	16 \pm 16	26 \pm 33	34 \pm 24

Tab.30: Height differences for each type of transition relative to the actual displacement performed with the Sabatini filter evaluated with the (mean values \pm standard deviations) cm of absolute deviation, mean error, and percentage error across 20 subjects.

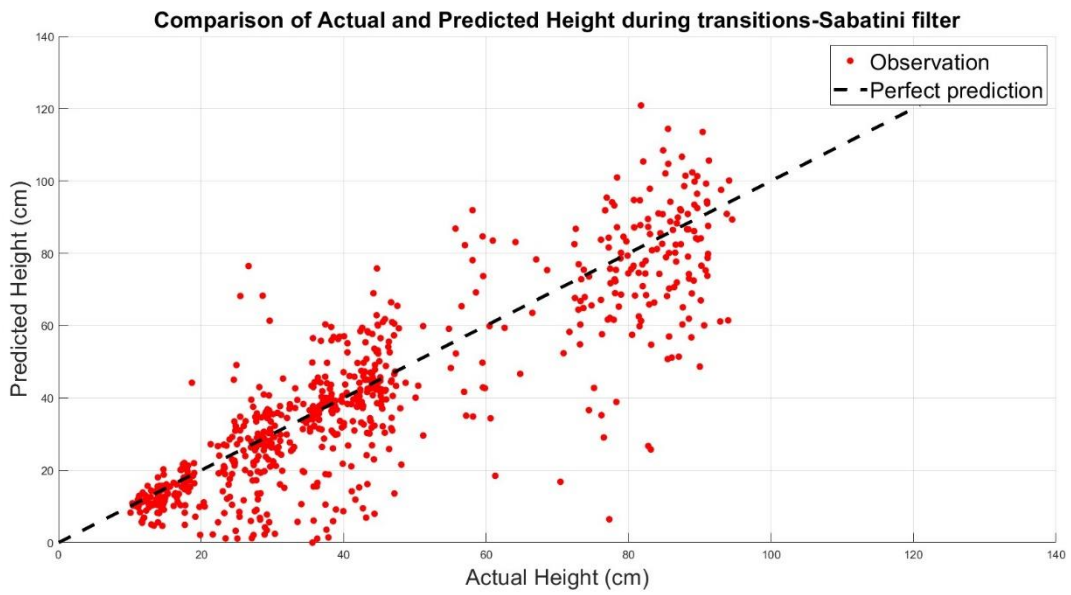


Fig. 73: Plot of the predicted height differences estimated by the Sabatini filter versus the actual height differences provided by the reference system during automatically identified transitions.

Kalman filter

	<i>StS</i>	<i>StS slow</i>	<i>Laying</i>	<i>Step</i>	<i>Squat</i>
<i>Absolute deviation (cm)</i>	3.8 ± 2.8	5.9 ± 4.8	6.4 ± 5.5	4.4 ± 3.6	4.2 ± 3.4
<i>Mean error (cm)</i>	-0.6 ± 4.7	2.4 ± 7.3	0.8 ± 8.4	-1.2 ± 5.6	3.1 ± 4.4
<i>Percentage error (%)</i>	11 ± 9	17 ± 14	8 ± 7	28 ± 23	10 ± 7

Tab.31: Height differences for each type of transition relative to the actual displacement performed with the Kalman filter evaluated with the (mean values \pm standard deviations) cm of absolute deviation, mean error, and percentage error across 20 subjects.

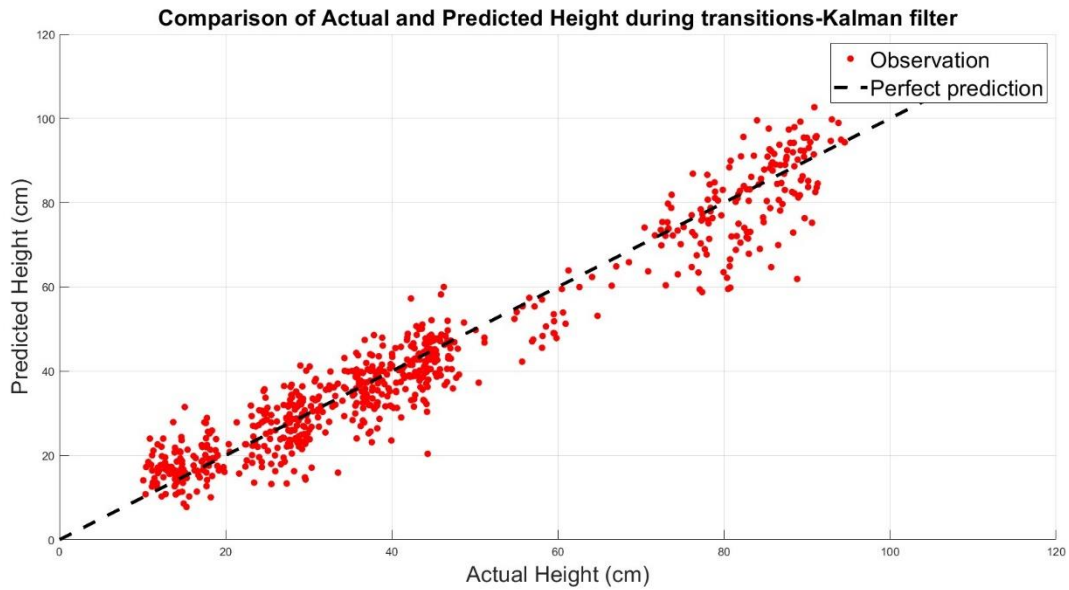


Fig.74: Plot of the predicted height differences estimated by the Kalman filter versus the actual height differences provided by the reference system during automatically identified transitions.

Barometer (approach 1)

	<i>StS</i>	<i>StS slow</i>	<i>Laying</i>	<i>Step</i>	<i>Squat</i>
<i>Absolute deviation (cm)</i>	3.8 ± 2.8	5.9 ± 4.8	6.4 ± 5.5	4.7 ± 4.1	4.1 ± 3.4
<i>Mean error (cm)</i>	-0.6 ± 4.7	2.4 ± 7.3	-0.8 ± 8.5	-0.9 ± 6.1	3.0 ± 4.4
<i>Percentage error (%)</i>	11 ± 9	17 ± 14	8 ± 7	28 ± 24	9 ± 7

Tab.32: Height differences for each type of transition relative to the actual displacement performed with the barometer (approach 1) evaluated with the (mean values \pm standard deviations) cm of absolute deviation, mean error, and percentage error across 20 subjects.

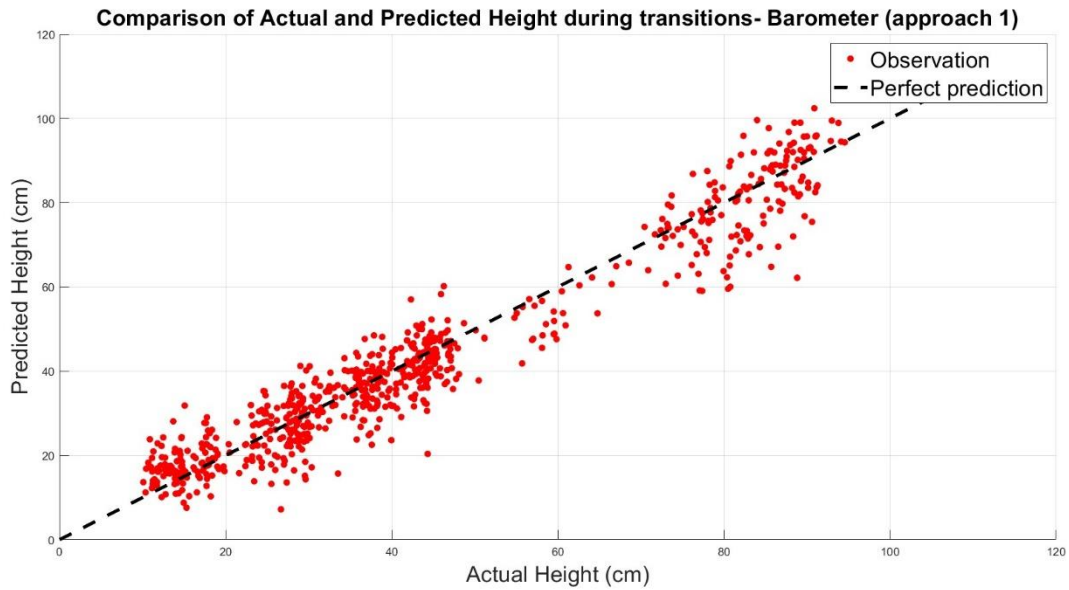


Fig.75: Plot of the predicted height differences estimated by the barometer (approach 1) versus the actual height differences provided by the reference system during automatically identified transitions.

Barometer (approach 2)

	<i>StS</i>	<i>StS slow</i>	<i>Laying</i>	<i>Step</i>	<i>Squat</i>
<i>Absolute deviation (cm)</i>	5.4 ± 5.7	7.1 ± 5.5	7.1 ± 6.3	5.9 ± 7.2	7.5 ± 8.2
<i>Mean error (cm)</i>	4.8 ± 6.2	6.4 ± 6.2	6.0 ± 7.4	4.5 ± 8.2	6.9 ± 8.7
<i>Percentage error (%)</i>	15 ± 14	21 ± 17	8 ± 8	31 ± 31	17 ± 19

Tab.33: Height differences for each type of transition relative to the actual displacement performed with the barometer (approach 2) evaluated with the (mean values ± standard deviations) cm of absolute deviation, mean error, and percentage error across 20 subjects.

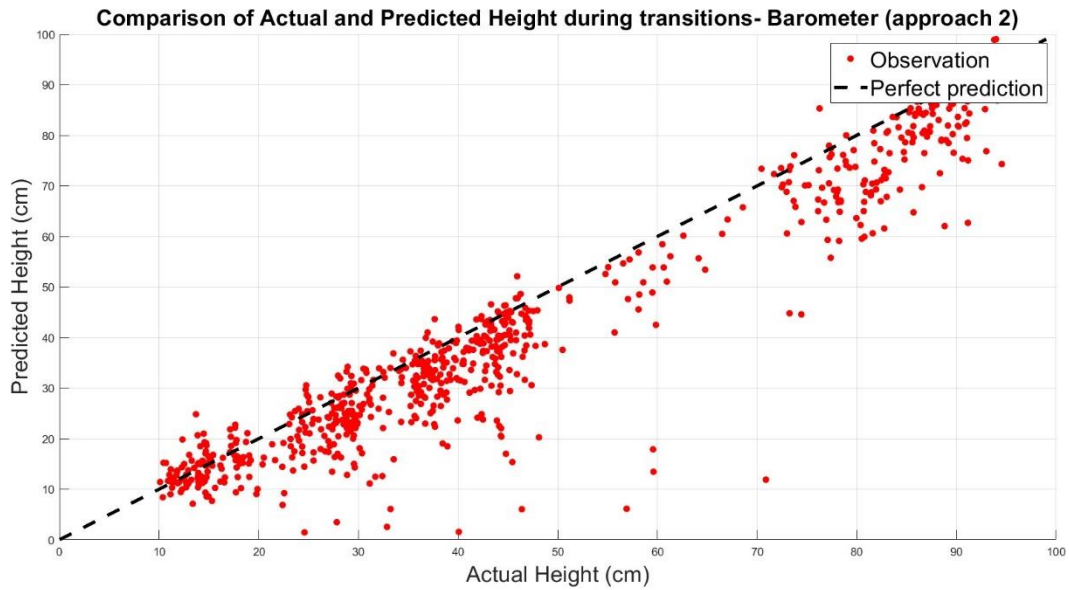


Fig.76: Plot of the predicted height differences estimated by the barometer (approach 2) versus the actual height differences provided by the reference system during automatically identified transitions.

Barometer (approach 3)

	<i>StS</i>	<i>StS slow</i>	<i>Laying</i>	<i>Step</i>	<i>Squat</i>
<i>Absolute deviation (cm)</i>	3.8 ± 2.8	5.9 ± 4.8	6.4 ± 5.5	4.4 ± 3.6	4.2 ± 3.4
<i>Mean error (cm)</i>	-0.6 ± 4.7	2.7 ± 7.3	0.8 ± 8.4	-1.2 ± 5.6	3.1 ± 4.4
<i>Percentage error (%)</i>	11 ± 9	17 ± 14	8 ± 7	27 ± 24	10 ± 7

Tab.34: Height differences for each type of transition relative to the actual displacement performed with the barometer (approach 3) evaluated with the (mean values ± standard deviations) cm of absolute deviation, mean error, and percentage error across 20 subjects.

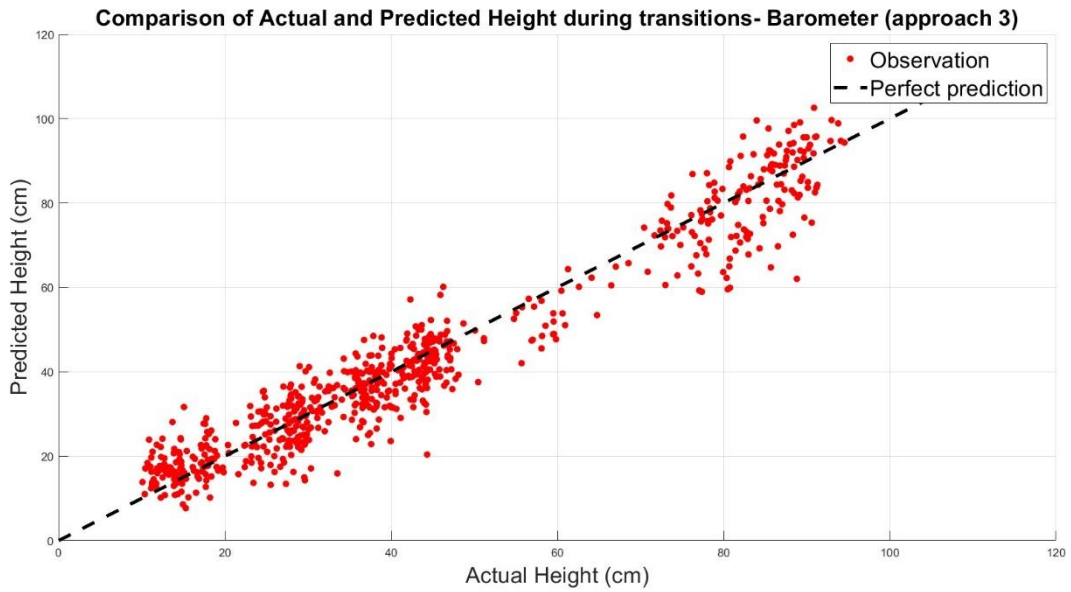


Fig.77: Plot of the predicted height differences estimated by the barometer (approach 3) versus the actual height differences provided by the reference system during automatically identified transitions.

Accelerometer

	<i>StS</i>	<i>StS slow</i>	<i>Laying</i>	<i>Step</i>	<i>Squat</i>
<i>Absolute deviation (cm)</i>	5.7 ± 6.1	14 ± 10	13 ± 13	5.2 ± 8.6	15 ± 9.9
<i>Mean error (cm)</i>	0.6 ± 8.3	11 ± 14	6.0 ± 17	-0.2 ± 10	-1.6 ± 18
<i>Percentage error (%)</i>	17 ± 19	41 ± 32	16 ± 16	26 ± 33	34 ± 24

Tab.35: Height differences for each type of transition relative to the actual displacement performed with the accelerometer

evaluated with the (mean values \pm standard deviations) cm of absolute deviation, mean error, and percentage error across 20 subjects.

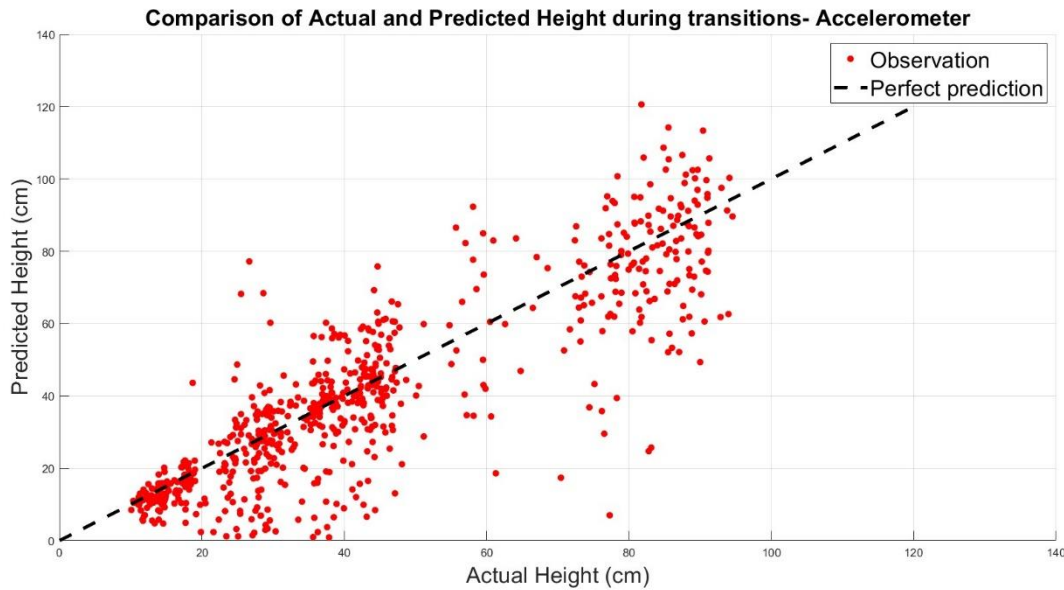


Fig. 78: Plot of the predicted height differences estimated by the accelerometer versus the actual height differences provided by the reference system during automatically identified transitions.

5.3 Testing

5.3.1 Detection of transitions

A statistical analysis was conducted to evaluate the ability of the method to generalize, evaluating the distribution of the F1-score, considering both the division by test (2 groups: Test 1, Test 2) and by subjects (20 groups).

The distributions of the F1 scores are not normal for all the analyses conducted, evaluated through the Shapiro-Wilk test.

Using the Kruskal-Wallis test with a significance level of $\alpha=0.05$, it was found that there is no significant difference when considering the division by subjects (with post hoc correction with the Bonferroni correction).

However, there is a significant difference between Test 1 and Test 2.

5.3.2 Tracking of the vertical trajectory of CoM

Statistical analysis is performed both on the reconstruction of the trajectory throughout the entire trial and on the perceived height differences during the transitions classified by type. The analyses are performed both by providing manually labeled transitions and by executing the complete pipeline.

Manual transitions

Reconstruction of the trajectory throughout the trial

1) The distribution of RMSE error is evaluated for each method (3 approaches with the barometer, accelerometer, sensor fusion with Kalman filter, and sensor fusion with Sabatini filter) individually, assessing the error distribution between Test 1 and Test 2 (Tab.35). The significance level is set at 0.05.

For each method, it is assessed whether the error distribution is normal using the Shapiro-Wilk test (in the following table, in the 'normal distribution' box, **X** indicates a non-normal distribution, while \checkmark a normal distribution).

If the distribution is normal, parametric analysis is performed using the ANOVA test, while otherwise, the Kruskal-Wallis test is used.

In both cases, the p-value is obtained. If $p > 0.05$, there are no significant differences between the error distributions, while if $p < 0.05$, there are significant differences.

It is noted that there are no significant differences ($\alpha=0.05$, $p>0.05$) between the two tests for all the proposed methods.

<i>Method</i>	<i>Normal distribution</i>	<i>Anova test</i>	<i>Kruskar-Wallis test</i>	<i>p-value</i>
<i>Barometer approach 1</i>	X	X	\checkmark	<i>>0.05</i>
<i>Barometer approach 2</i>	\checkmark	\checkmark	X	<i>>0.05</i>
<i>Barometer approach 3</i>	X	X	\checkmark	<i>>0.05</i>

<i>Accelerometer</i>	X	X	✓	>0.05
<i>Kalman filter</i>	X	X	✓	>0.05
<i>Sabatini filter</i>	X	X	✓	>0.05

Tab. 35: Statistical analysis assessing the distribution of RMSE error throughout the trial for each method (3 approaches with the barometer, accelerometer, sensor fusion with Kalman filter, and sensor fusion with Sabatini filter) individually, evaluating the error distribution between Test 1 and Test 2. The significance level is set at 0.05.

2) The distribution of RMSE error is evaluated for each method (3 approaches with the barometer, accelerometer, sensor fusion with Kalman filter, and sensor fusion with Sabatini filter) individually, assessing the error distribution between subjects (Tab.36). The significance level is set at 0.05.

For each method, it is assessed whether the error distribution is normal using the Shapiro-Wilk test (in the following table, in the 'normal distribution' box, **X** indicates a non-normal distribution, while ✓ a normal distribution).

If the distribution is normal, parametric analysis is performed using the ANOVA test, while otherwise, the Kruskal-Wallis test is used.

In both cases, the p-value is obtained. If $p > 0.05$, there are no significant differences between the error distributions, while if $p < 0.05$, there are significant differences. Since multiple analyses are performed, a post hoc correction is necessary. If the correction performed with the Bonferroni method confirms the hypothesis of no significant differences, the symbol ✓ is indicated in the appropriate box in the following table. If the error distributions are significantly different, the group with a different distribution is identified through post hoc correction and is indicated in the table.

It is noted that there are no significant differences ($\alpha=0.05$, $p>0.05$) between the subjects for all the proposed methods.

<i>Method</i>	<i>Normal distribution</i>	<i>Anova test</i>	<i>Kruskar-Wallis test</i>	<i>p-value</i>	<i>Post hoc correction</i>
<i>Barometer approach 1</i>	X	X	✓	>0.05	✓

<i>Barometer approach 2</i>	✓	✓	✗	>0.05	✓
<i>Barometer approach 3</i>	✗	✗	✓	>0.05	✓
<i>Accelerometer</i>	✗	✗	✓	>0.05	✓
<i>Kalman filter</i>	✗	✗	✓	>0.05	✓
<i>Sabatini filter</i>	✗	✗	✓	>0.05	✓

Tab. 36: Statistical analysis assessing the distribution of RMSE error throughout the trial for each method (3 approaches with the barometer, accelerometer, sensor fusion with Kalman filter, and sensor fusion with Sabatini filter) individually, evaluating the error distribution between subjects. The significance level is set at 0.05.

3) The distribution of RMSE error is evaluated between the six proposed method (3 approaches with the barometer, accelerometer, sensor fusion with Kalman filter, and sensor fusion with Sabatini filter), assessing the error distribution between them. The significance level is set at 0.05. The error distribution is non-normal, analyzed using the Shapiro-Wilk test. The Kruskal-Wallis highlights that $p < 0.05$ and there are significant differences between the methods.

Height Difference During Classified Transitions

1) For each method of reconstructing the vertical trajectory of the CoM (three approaches using the barometer, accelerometer, sensor fusion with Kalman filter, and sensor fusion with Sabatini filter), the distribution of the absolute deviation across different types of transitions (StS, slow StS, Laying, step, and squat) is evaluated (Tab.37). Considering the 20 subjects, each method comprises a total of 240 StS transitions, 80 slow StS transitions, 160 laying transitions, 240 steps, and 160 squats.

For every approach, it is assessed whether the error distribution is normal using the Shapiro-Wilk test (in the following table, in the 'normal distribution' box, ✗ indicates a non-normal distribution, while ✓ a normal distribution).

If the distribution is normal, parametric analysis is performed using the ANOVA test, while otherwise, the Kruskal-Wallis test is used.

In both cases, the p-value is obtained. If $p > 0.05$, there are no significant differences between the error distributions, while if $p < 0.05$, there are significant differences.

Since multiple analyses are performed, a post hoc correction is necessary. If the correction performed with the Bonferroni method confirms the hypothesis of no significant differences, the symbol \checkmark is indicated in the appropriate box in the following table. If the error distributions are significantly different, the group with a different distribution is identified through post hoc correction and indicated in the table.

It is noted that there are significant differences ($\alpha=0.05$, $p<0.05$) for all methods.

<i>Method</i>	<i>Normal distribution</i>	<i>Anova test</i>	<i>Kruskar-Wallis test</i>	<i>p-value</i>	<i>Post hoc correction</i>
<i>Barometer approach 1</i>	X	X	\checkmark	< 0.05	Significant difference with the squat transition
<i>Barometer approach 2</i>	X	X	\checkmark	< 0.05	Significant difference with the squat transition
<i>Barometer approach 3</i>	X	X	\checkmark	< 0.05	Significant difference with the squat transition
<i>Accelerometer</i>	X	X	\checkmark	< 0.05	Significant difference with the step transition
<i>Kalman filter</i>	X	X	\checkmark	< 0.05	Significant difference with the squat transition
<i>Sabatini filter</i>	X	X	\checkmark	< 0.05	Significant difference with the step transition

Tab.37: Each method of reconstructing the vertical trajectory of the CoM (three approaches using the barometer, accelerometer, sensor fusion with Kalman filter, and sensor fusion with Sabatini filter) is evaluated to analyze the distribution of the absolute deviation across different types of transitions (StS, slow StS, Laying, step, and squat).

2) The distribution of absolute deviations for the 874 transitions performed by each of the 20 subjects is evaluated across various methods of reconstructing the vertical trajectory (three approaches using the barometer, accelerometer, sensor fusion with Kalman filter, and sensor fusion with Sabatini filter). The error distribution, assessed using the Shapiro-Wilk test, is non-normal. Consequently, a non-parametric analysis is conducted using the Kruskal-Wallis test, revealing a significant difference ($\alpha=0.05$, $p<0.05$). Post hoc correction highlights that the method referred to as 'Barometer (approach 2)' has a significantly different error distribution compared to the other methods.

Automatic transitions

Reconstruction of the trajectory throughout the trial

1) The distribution of RMSE error is evaluated for each method (3 approaches with the barometer, accelerometer, sensor fusion with Kalman filter, and sensor fusion with Sabatini filter) individually, assessing the error distribution between Test 1 and Test 2 (Fig.38). The significance level is set at 0.05.

For each method, it is assessed whether the error distribution is normal using the Shapiro-Wilk test (in the following table, in the 'normal distribution' box, **X** indicates a non-normal distribution, while \checkmark a normal distribution).

If the distribution is normal, parametric analysis is performed using the ANOVA test, while otherwise, the Kruskal-Wallis test is used.

In both cases, the p-value is obtained. If $p > 0.05$, there are no significant differences between the error distributions, while if $p < 0.05$, there are significant differences.

It is noted that there are no significant differences ($\alpha=0.05$, $p>0.05$) between the two tests for all the proposed methods.

<i>Method</i>	<i>Normal distribution</i>	<i>Anova test</i>	<i>Kruskar-Wallis test</i>	<i>p-value</i>
<i>Barometer approach 1</i>	\checkmark	\checkmark	X	<i>>0.05</i>
<i>Barometer approach 2</i>	\checkmark	\checkmark	X	<i>>0.05</i>

<i>Barometer approach 3</i>	X	X	✓	>0.05
<i>Accelerometer</i>	X	X	✓	>0.05
<i>Kalman filter</i>	X	X	✓	>0.05
<i>Sabatini filter</i>	X	X	✓	>0.05

Tab. 38: Statistical analysis assessing the distribution of RMSE error throughout the trial for each method (3 approaches with the barometer, accelerometer, sensor fusion with Kalman filter, and sensor fusion with Sabatini filter) individually, evaluating the error distribution between Test 1 and Test 2. The significance level is set at 0.05.

2) The distribution of RMSE error is evaluated for each method (3 approaches with the barometer, accelerometer, sensor fusion with Kalman filter, and sensor fusion with Sabatini filter) individually, assessing the error distribution between subjects (Fig.39). The significance level is set at 0.05.

For each method, it is assessed whether the error distribution is normal using the Shapiro-Wilk test (in the following table, in the 'normal distribution' box, **X** indicates a non-normal distribution, while ✓ a normal distribution).

If the distribution is normal, parametric analysis is performed using the ANOVA test, while otherwise, the Kruskal-Wallis test is used.

In both cases, the p-value is obtained. If $p > 0.05$, there are no significant differences between the error distributions, while if $p < 0.05$, there are significant differences. Since multiple analyses are performed, a post hoc correction is necessary. If the correction performed with the Bonferroni method confirms the hypothesis of no significant differences, the symbol ✓ is indicated in the appropriate box in the following table. If the error distributions are significantly different, the group with a different distribution is identified through post hoc correction and indicated in the table.

It is noted that there are no significant differences ($\alpha=0.05$, $p>0.05$) between the subjects for all the proposed methods.

<i>Method</i>	<i>Normal distribution</i>	<i>Anova test</i>	<i>Kruskar-Wallis test</i>	<i>p-value</i>	<i>Post hoc correction</i>
<i>Barometer approach 1</i>	✓	✓	✗	<i>>0.05</i>	✓
<i>Barometer approach 2</i>	✓	✓	✗	<i>>0.05</i>	✓
<i>Barometer approach 3</i>	✗	✗	✓	<i>>0.05</i>	✓
<i>Accelerometer</i>	✗	✗	✓	<i>>0.05</i>	✓
<i>Kalman filter</i>	✗	✗	✓	<i>>0.05</i>	✓
<i>Sabatini filter</i>	✗	✗	✓	<i>>0.05</i>	✓

Tab.39: Statistical analysis assessing the distribution of RMSE error throughout the trial for each method (3 approaches with the barometer, accelerometer, sensor fusion with Kalman filter, and sensor fusion with Sabatini filter) individually, evaluating the error distribution between subjects. The significance level is set at 0.05.

3) The distribution of RMSE error is evaluated between the six proposed method (3 approaches with the barometer, accelerometer, sensor fusion with Kalman filter, and sensor fusion with Sabatini filter), assessing the error distribution between them. The significance level is set at 0.05. The error distribution is non-normal, analyzed using the Shapiro-Wilk test. The Kruskal-Wallis highlights that $p > 0.05$ and there are significant differences between the methods.

Height Difference During Classified Transitions

1) For each method of reconstructing the vertical trajectory of the CoM (three approaches using the barometer, accelerometer, sensor fusion with Kalman filter, and sensor fusion with Sabatini filter), the distribution of the absolute deviation across different types of transitions (StS, slow StS, Laying, step, and squat) is evaluated (Fig.40). Considering the 20 subjects, the dataset comprises a total of 238 StS transitions, 76 slow StS transitions, 158 laying transitions, 144 steps, and 89 squats correctly recognized.

For every approach, it is assessed whether the error distribution is normal using the Shapiro-Wilk test (in the following table, in the 'normal distribution' box, ✗ indicates a non-normal distribution,

while \checkmark a normal distribution).

If the distribution is normal, parametric analysis is performed using the ANOVA test, while otherwise, the Kruskal-Wallis test is used.

In both cases, the p-value is obtained. If $p > 0.05$, there are no significant differences between the error distributions, while if $p < 0.05$, there are significant differences.

Since multiple analyses are performed, a post hoc correction is necessary. If the correction performed with the Bonferroni method confirms the hypothesis of no significant differences, the symbol \checkmark is indicated in the appropriate box in the following table. If the error distributions are significantly different, the group with a different distribution is identified through post hoc correction and indicated in the table.

It is noted that there are significant differences ($\alpha=0.05$, $p<0.05$) for all methods.

<i>Method</i>	<i>Normal distribution</i>	<i>Anova test</i>	<i>Kruskar-Wallis test</i>	<i>p-value</i>	<i>Post hoc correction</i>
<i>Barometer approach 1</i>	X	X	\checkmark	< 0.05	Significant difference the StS slow and laying transitions with StS
<i>Barometer approach 2</i>	X	X	\checkmark	< 0.05	Significant difference the StS transition and step transitions with the others
<i>Barometer approach 3</i>	X	X	\checkmark	< 0.05	Significant difference the StS transition with StS slow and laying
<i>Accelerometer</i>	X	X	\checkmark	< 0.05	Significant difference the StS transition and step transitions with the others

<i>Kalman filter</i>	X	X	✓	< 0.05	Significant difference the StS transition with StS slow and laying
<i>Sabatini filter</i>	X	X	✓	< 0.05	Significant difference the StS transition and step transitions with the others

Tab.40: Each method of reconstructing the vertical trajectory of the CoM (three approaches using the barometer, accelerometer, sensor fusion with Kalman filter, and sensor fusion with Sabatini filter) is evaluated to analyze the distribution of the absolute deviation across different types of transitions (StS, slow StS, Laying, step, and squat).

2) The distribution of absolute deviations for the 705 transitions performed by the 20 subjects is evaluated across various methods of reconstructing the vertical trajectory (three approaches using the barometer, accelerometer, sensor fusion with Kalman filter, and sensor fusion with Sabatini filter). The error distribution, assessed using the Shapiro-Wilk test, is non-normal. Consequently, a non-parametric analysis is conducted using the Kruskal-Wallis test, revealing a non-significant difference ($\alpha=0.05$, $p>0.05$). Post hoc correction highlights that the method hasn't a significantly different error distribution between them.

6. Discussion

The present study aims to propose and validate a novel method for reconstructing the vertical displacement of the Center of Mass using barometric sensors integrated into the INDIP wearable system, which includes an inertial measurement unit.

Twenty healthy subjects performed two trials of daily activities in a controlled laboratory environment, including Sit-to-Stand (StS), lying on a mattress, squatting, and step climbing. The stereophotogrammetric system was employed as the gold standard.

The proposed algorithm hypothesizes that the height of the CoM remains constant except during transitions, where it increases or decreases. Transitions were identified using the derivative method by calculating the first derivative of the barometric signal. During transitions, vertical displacement was tracked using four approaches: barometer-only data, accelerometer-only data, and two sensor fusion approaches, using data from both sensors.

6.1 Method based on derivative

Detection of transitions

Firstly, the method for detecting transitions is evaluated against the transitions manually labeled by the stereophotogrammetric signal. The detection performance is assessed in terms of precision, sensitivity, and F1 score (Table 9). Additionally, the sensitivity of transition detection is calculated and reported separately for each type of movement, including Sit-to-Stand (StS), slow Sit-to-Stand (StS slow), lying down, stair climbing, and squatting. This detailed analysis helps determine whether the proposed method performs better for specific types of transitions or maintains consistent performance across different movements (Table 10). Statistical analysis was conducted to evaluate the distribution of F1 score values, examining the method's ability to generalize across subjects and tests.

The results show an average F1 score of 90%. Notably, Test 1, which included only StS, StS slow, and lying down, achieved a higher F1 score of 98% compared to Test 2, which also included stair climbing and squatting, achieving an F1 score of 81%. The significant difference between tests is confirmed by the statistical analysis.

When calculating sensitivity according to the type of transition, it is observed that StS, slow StS, and lying transitions show detection rates of 99% for the first two and 100% for lying down. In contrast, the performance decreases for stair and squat transitions, with sensitivities of 60% and

56%, respectively (Table 10). Sensitivity, which is penalized by false negatives, is very high for Test 1, at 100%, but decreases to 70% for Test 2. Precision remains high for both tests, around 97%, indicating that the proposed method identifies few false positives despite the tests.

It can therefore be concluded that the method's effectiveness is constrained by the type of transitions, as confirmed by the statistical analysis. However, it is robust regardless of the mode of movement, including both slow and comfortable speed Sit-to-Stand transitions.

It performs better for transitions involving larger vertical displacements, such as StS and lying down. The vertical displacements associated with step execution are around 15 cm, a value similar to the amplitude noise in the barometric signal. Regarding squats, despite the significant vertical displacement, they are detected with a low percentage because, being rapid movements, the barometric signal processing through a moving average dampens the amplitude of the movement, penalizing its detection.

The threshold values present in the derivative method (such as the peak of the derivative and the minimum height difference to consider a segment as a transition) were chosen by tuning the data, evaluating sensitivity and precision. The choice of threshold values aimed to optimize both scores. Indeed, a high number of missed events would indicate that, according to the proposed algorithm and with a view to exporting the method to a home environment, the subject moves less than reality, presupposing poor motor skills.

Conversely, a high number of extra events would suggest that the subject moves more than reality, presupposing good motor skills. Overestimating transitions could lead to the satisfaction of a rehabilitation path, while underestimating transitions could result in its intensification.

Temporal correctness

The temporal accuracy of the correctly identified transitions is evaluated in terms of delay and duration (Table 11). Analyzing the mean delay and duration of the transitions identified using the derivative method, it is noted that these values are negative. Since they are calculated by subtracting the reconstructed values from the reference ones, it is inferred that the automatic transitions are detected with a delay and exhibit a longer duration compared to the gold standard.

6.2 Tracking of the vertical trajectory of the CoM

The reconstruction of the vertical displacement of the Center of Mass is evaluated using both manually labeled transitions and automatically detected transitions. In the case of automatically detected transitions, the reconstruction process is halted if any transitions are not detected. Errors are assessed using Root Mean Square Error (RMSE), mean error, and correlation coefficient, calculated over the entire reconstructed trial.

Furthermore, for each type of movement (StS, StS slow, lying down, steps, and squatting), the mean absolute error, mean error, and percentage error in height elevation/reduction during transitions are reported.

Statistical analysis was conducted to assess the generalization capability of each method, independent of test, subject, and transition type. Additionally, the performance was evaluated in terms of RMSE distributions to identify any significant differences between the methods.

Manually labelled transitions

The performances (Tab.12, Tab.13, Tab.14, Tab.15, Tab.16, Tab.17) highlight that the reconstruction using the barometer provides the best outcomes, with an average RMSE of (10 ± 4) cm and a correlation coefficient of (0.96 ± 0.03) . The accelerometer yields the poorest performance, with an RMSE of (31 ± 20) cm and a correlation of (0.80 ± 0.18) . The Kalman filter, which combines barometric and accelerometric information, offers intermediate results with an RMSE of (15 ± 9) cm and a correlation coefficient of (0.94 ± 0.04) . The Sabatini filter, also a sensor fusion technique, provides performance very similar to that of the accelerometer. This implies that in the sensor fusion process, the weights are initialized in such a way that the accelerometer is favoured over the barometer.

Regarding the performance related to the Δh executed during a transition (Tab.18, Tab.19, Tab.20, Tab.21, Tab.22, Tab.23), the methods showed almost similar values. The highest percentage error is associated with the execution of a step.

The statistical analysis revealed that each method of CoM displacement reconstruction is consistent regardless of the subject and the trial. However, the distributions of absolute deviations associated with the transitions vary depending on the type of transition.

Finally, evaluating the RMSE distributions between the methods reveals that they are significantly different.

Automatic transitions

The performances (Tab.24, Tab.25, Tab.26, Tab.27, Tab.28, Tab.29) highlight that the reconstruction using the barometer provides the best outcomes, with an average RMSE of (8 ± 3) cm and a correlation coefficient of (0.97 ± 0.02) . The accelerometer yields the poorest performance, with an RMSE of (33 ± 19) cm and a correlation of (0.80 ± 0.18) . The Kalman filter, which combines barometric and accelerometric information, offers intermediate results with an RMSE of (19 ± 12) cm and a correlation coefficient of (0.93 ± 0.05) . The Sabatini filter, also a sensor fusion technique, provides performance very similar to that of the accelerometer. This implies that in the sensor fusion process, the weights are initialized in such a way that the accelerometer is favoured over the barometer.

The results show that the use of a single barometer provides the best height reconstruction. This outcome was unexpected and could be attributed to the specific implementation of the initial part of the pipeline, which relies heavily on the barometric signal's morphology to detect transitions. Additionally, the sensor fusion methods could be further enhanced. The integration of accelerometer data, after gravity removal, is not optimal because the intervals for double integration to obtain the vertical displacement are determined based on the barometric signal. Consequently, the conditions applied to the integration may not be accurate. Specifically, the reconstruction using the accelerometer could be improved by incorporating the accelerometric signal to detect transition instances more accurately.

It is noted that when providing the algorithm with automatic transitions, the average percentage error between StS and StS slow diverges and the StS slow has a higher error. This could be caused by the temporal accuracy of the identified transitions with the derivative method.

The average RMSE values corroborate the results obtained by Sabatini et al. in their work, where they reported an RMSE range of 5 to 68 cm for the tests conducted. Particularly noteworthy in Sabatini's study is the squatting test, which is also included in this thesis. In Sabatini's work, this test demonstrated an average RMSE of 50 cm. These values are confirmed and improved with the same filter implemented in this study, as the average RMSE obtained is 31 cm.

The statistical analysis revealed that each method of CoM displacement reconstruction is consistent regardless of the subject and the trial. However, the distributions of absolute deviations associated with the transitions vary depending on the type of transition. Finally, evaluating the RMSE distributions between the methods reveals that they are significantly different.

7. Conclusion

The study aimed to develop and validate a method for tracking the vertical trajectory of a subject performing daily activities in a controlled environment. The objective is to adapt this method for everyday living environments, allowing for long-term recordings to gather information on subjects' motor abilities.

To this aim, the wearable multi-sensor INDIP system, which includes an IMU, was integrated with the BMP390 barometer from Bosch at both the hardware and firmware levels. This integration overcomes the limitations of using a single IMU for vertical displacement reconstruction, providing a direct measurement of height.

The study proposes an innovative use of the barometer, typically an altimeter in avionics, to detect small height variations.

Twenty healthy subjects were involved in the study, performing two tests simulating daily activities such as sit-to-stand (StS), lying on a mattress, ascending and descending steps, and performing squats. The stereophotogrammetric system was used as a reference.

The proposed pipeline is based on two steps. First, transitions are identified, which are intervals where the height of the CoM increases or decreases. Outside these intervals, the height is assumed to be constant. During transitions, height is reconstructed using various methods: single barometer, single accelerometer, or sensor fusion approaches that combine both data sources.

The results show an average F1 score of 90% for detecting transitions. The method works best for StS and lying down, while further investigations are needed to identify the execution of steps and squatting.

The implemented methods allow for accurate estimation of vertical displacement, matching and improving upon the results obtained by Sabatini et al., who reported RMSE values ranging from 5 to 68 cm.

The integration of the barometric data in the sensor fusion approach using a Kalman filter enhances the performance compared to the double integration of the accelerometer's vertical component, achieving average RMSE values of 19 cm and 33 cm, respectively.

The limitations of the proposed study include the restricted number of participants and the fact that all subjects were healthy individuals. Additionally, although daily activities were simulated, the testing environment was overly controlled.

Therefore, it is necessary to evaluate the method in real-world conditions and with subjects with different motor conditions.

In conclusion, the integration of the barometer and IMU yielded good results in accurately measuring height changes. This advancement offers significant potential for biomechanical analysis and energy consumption assessment, enhancing the understanding and evaluation of human movement in real-world settings.

Future works

The work developed in this study can open numerous avenues, both for enhancing the proposed algorithms and for leveraging the collected data to propose new methods.

The implemented method relies heavily on the barometric signal. Specifically, the detection of transitions is based solely on the barometric signal. Despite the good performance achieved, transition detection could be improved by integrating the accelerometer signal, which would be specifically processed to enhance the detection of transition moments. These points correspond to the instances of double integration of the accelerometer. This approach would result in more accurate reconstruction provided by the accelerometer, thereby improving the sensor fusion. As highlighted in paragraph 4.5.3, enhancing the accuracy of the start and end points of transitions leads to a significant improvement in the vertical displacement reconstruction using the accelerometer.

Furthermore, the proposed method could be applied in everyday living environments with prolonged recordings. In such cases, it would be interesting to assess the performance of the barometer in a noisier, uncontrolled setting compared to the laboratory environment. In the absence of the stereophotogrammetric system, a new reference system would be necessary.

In this study, a single sensor setup was chosen for the development of the algorithm, prioritizing this over the development of a method that utilizes both barometers positioned on the subjects (one on the pelvis and one on the foot). While the dual sensor setup does not provide a direct measurement of the vertical displacement of the pelvis relative to the floor, it could still be explored for extracting other parameters. This approach effectively allows for the removal of common noise and drift.

Finally, the INDIP system could integrate the barometer internally, ensuring that the sensor setup remains compact and non-intrusive for the subjects. Additionally, it would be beneficial to evaluate the performance of other pressure sensors, given that the BMP390 was released in 2019. This assessment could lead to the incorporation of more advanced sensors that offer improved performance and further minimize the system's size and weight.

References

- [1] khan academy, "What is the center of mass? Learn the definition of center of mass and learn how to calculate it."
- [2] I. Kingma, H. M. Toussaint, D. A. C. M. Commissaris, M. J. M. Hoozemans, and M. J. Ober, "OPTIMIZING THE DETERMINATION OF THE BODY CENTER OF MASS," 1995.
- [3] M. Germanotta, I. Mileti, I. Conforti, Z. Del Prete, I. Aprile, and E. Palermo, "Estimation of human center of mass position through the inertial sensors-based methods in postural tasks: An accuracy evaluation," *Sensors (Switzerland)*, vol. 21, no. 2, pp. 1–17, Jan. 2021, doi: 10.3390/s21020601.
- [4] R. Rossanigo *et al.*, "Base of Support, Step Length and Stride Width Estimation during Walking Using an Inertial and Infrared Wearable System," *Sensors*, vol. 23, no. 8, Apr. 2023, doi: 10.3390/s23083921.
- [5] M. Zok, C. Mazzà, and U. Della Croce, "Total body centre of mass displacement estimated using ground reactions during transitory motor tasks: Application to step ascent," *Med Eng Phys*, vol. 26, no. 9 SPEC.ISS., pp. 791–798, 2004, doi: 10.1016/j.medengphy.2004.07.005.
- [6] F. Masse, R. Gonzenbach, A. Paraschiv-Ionescu, A. R. Luft, and K. Aminian, "Wearable barometric pressure sensor to improve postural transition recognition of mobility-impaired stroke patients," *IEEE Transactions on Neural Systems and Rehabilitation Engineering*, vol. 24, no. 11, pp. 1210–1217, Nov. 2016, doi: 10.1109/TNSRE.2016.2532844.
- [7] H. P. Nguyen *et al.*, "Auto detection and segmentation of physical activities during a Timed-Up-and-Go (TUG) task in healthy older adults using multiple inertial sensors," *J Neuroeng Rehabil*, vol. 12, no. 1, Apr. 2015, doi: 10.1186/s12984-015-0026-4.
- [8] Massé F, Gonzenbach R, Paraschiv-Ionescu A, Luft AR, and Aminian K, "Detection of postural transitions using trunk-worn inertial and barometric pressure sensor: application to stroke patients."
- [9] N. Oliveira, F. Carvalho, J. Laíns, D. Rasteiro, and L. Roseiro, "Development of a Biomechanical Device for Parameter Quantification Associated with the Sit-to-Stand Movement," *Sensors*, vol. 23, no. 4, Feb. 2023, doi: 10.3390/s23041837.
- [10] R. W. Bohannon, "Daily sit-to-stands performed by adults: a systematic review."
- [11] A. Cappozzo, U. Della Croce, A. Leardini, and L. Chiari, "Human movement analysis using stereophotogrammetry. Part 1: Theoretical background," *Gait and Posture*, vol. 21, no. 2. Elsevier Ireland Ltd, pp. 186–196, 2005. doi: 10.1016/j.gaitpost.2004.01.010.
- [12] L. Chiari, U. Della Croce, A. Leardini, and A. Cappozzo, "Human movement analysis using stereophotogrammetry. Part 2: Instrumental errors," *Gait and Posture*, vol. 21, no. 2. Elsevier Ireland Ltd, pp. 197–211, 2005. doi: 10.1016/j.gaitpost.2004.04.004.
- [13] M. Sonobe and Y. Inoue, "Center of Mass Estimation Using a Force Platform and Inertial Sensors for Balance Evaluation in Quiet Standing," *Sensors*, vol. 23, no. 10, May 2023, doi: 10.3390/s23104933.

- [14] L. Needham, M. Evans, D. P. Cosker, and S. L. Colyer, "Can markerless pose estimation algorithms estimate 3d mass centre positions and velocities during linear sprinting activities?," *Sensors*, vol. 21, no. 8, Apr. 2021, doi: 10.3390/s21082889.
- [15] W. W. T. Lam, Y. M. Tang, and K. N. K. Fong, "A systematic review of the applications of markerless motion capture (MMC) technology for clinical measurement in rehabilitation," *Journal of NeuroEngineering and Rehabilitation*, vol. 20, no. 1. BioMed Central Ltd, Dec. 01, 2023. doi: 10.1186/s12984-023-01186-9.
- [16] C. H. Lee and T. L. Sun, "Evaluation of postural stability based on a force plate and inertial sensor during static balance measurements," *J Physiol Anthropol*, vol. 37, no. 1, Feb. 2018, doi: 10.1186/s40101-018-0187-5.
- [17] M. Fusca, F. Negrini, P. Perego, L. Magoni, F. Molteni, and G. Andreoni, "Validation of a wearable IMU system for gait analysis: Protocol and application to a new system," *Applied Sciences (Switzerland)*, vol. 8, no. 7, Jul. 2018, doi: 10.3390/app8071167.
- [18] S. Cardarelli *et al.*, "Single IMU Displacement and Orientation Estimation of Human Center of Mass: A Magnetometer-Free Approach," *IEEE Trans Instrum Meas*, vol. 69, no. 8, pp. 5629–5639, Aug. 2020, doi: 10.1109/TIM.2019.2962295.
- [19] S. O. H. Madgwick, "An efficient orientation filter for inertial and inertial/magnetic sensor arrays," 2010.
- [20] A. Manivannan, W. C. B. Chin, A. Barrat, and R. Bouffanais, "On the challenges and potential of using barometric sensors to track human activity," *Sensors (Switzerland)*, vol. 20, no. 23. MDPI AG, pp. 1–36, Dec. 01, 2020. doi: 10.3390/s20236786.
- [21] D. E. Bolanakis, "MEMS Barometers Toward Vertical Position Detection: Background Theory, System Prototyping, and Measurement Analysis," *Synthesis Lectures on Mechanical Engineering*, vol. 1, no. 1, pp. 1–145, May 2017, doi: 10.2200/s00769ed1v01y201704mec003.
- [22] F. Massé, R. R. Gonzenbach, A. Arami, A. Paraschiv-Ionescu, A. R. Luft, and K. Aminian, "Improving activity recognition using a wearable barometric pressure sensor in mobility-impaired stroke patients," *J Neuroeng Rehabil*, vol. 12, no. 1, Aug. 2015, doi: 10.1186/s12984-015-0060-2.
- [23] A. Moncada-Torres, K. Leuenberger, R. Gonzenbach, A. Luft, and R. Gassert, "Activity classification based on inertial and barometric pressure sensors at different anatomical locations," *Physiol Meas*, vol. 35, no. 7, pp. 1245–1263, 2014, doi: 10.1088/0967-3334/35/7/1245.
- [24] IEEE Sensors Council and Institute of Electrical and Electronics Engineers, *INERTIAL 2018 : the 5th IEEE International Symposium on Inertial Sensors & Systems : 2018 symposium proceedings : Mar 26-28, Lake Como, Italy - Grand Hotel Imperial*.
- [25] J. Makma, D. Thanapatay, T. Isshiki, J. Chinrungrueng, and S. Thiemjarus, "Enhancing accelerometer-based human activity recognition with relative barometric pressure signal," in *ECTI-CON 2021 - 2021 18th International Conference on Electrical Engineering/Electronics, Computer, Telecommunications and Information Technology: Smart Electrical System and Technology, Proceedings*, Institute of Electrical and Electronics Engineers Inc., May 2021, pp. 529–532. doi: 10.1109/ECTI-CON51831.2021.9454927.

- [26] A. Ejupi, M. Brodie, S. R. Lord, J. Annegarn, S. J. Redmond, and K. Delbaere, "Wavelet-Based Sit-To-Stand Detection and Assessment of Fall Risk in Older People Using a Wearable Pendant Device," *IEEE Trans Biomed Eng*, vol. 64, no. 7, pp. 1602–1607, Jul. 2017, doi: 10.1109/TBME.2016.2614230.
- [27] Y. Sun, F. P-W Lo, S. Thiemjarus, and B. Lo, *Wearable Fall Detection System Using Barometric Pressure Sensors and Machine Learning*.
- [28] P. Pierleoni *et al.*, "A Wearable Fall Detector for Elderly People Based on AHRS and Barometric Sensor," *IEEE Sens J*, vol. 16, no. 17, pp. 6733–6744, Sep. 2016, doi: 10.1109/JSEN.2016.2585667.
- [29] M. J. Böttinger *et al.*, "'TiC-TUG': technology in clinical practice using the instrumented timed up and go test-a scoping review," *Aging clinical and experimental research*, vol. 36, no. 1. p. 100, Dec. 01, 2024. doi: 10.1007/s40520-024-02733-7.
- [30] A. M. Sabatini and V. Genovese, "A sensor fusion method for tracking vertical velocity and height based on inertial and barometric altimeter measurements," *Sensors (Switzerland)*, vol. 14, no. 8, pp. 13324–13347, Jul. 2014, doi: 10.3390/s140813324.
- [31] B. Yu, L. Chen, and M. Fatin Fatihur Rahman, "Design of Multi-sensor Fusion Positioning and Navigation Method Based on Federated Kalman Filter for Low-Speed Rotorcraft of Atmospheric Detection," in *Journal of Physics: Conference Series*, Institute of Physics, 2023. doi: 10.1088/1742-6596/2428/1/012031.
- [32] V. Sokolovic, G. Dikic, and R. Stancic, "Integration of INS, GPS, magnetometer and barometer for improving accuracy navigation of the vehicle," *Def Sci J*, vol. 63, no. 5, pp. 451–455, 2013, doi: 10.14429/dsj.63.4534.
- [33] Institute of Electrical and Electronics Engineers and American Society of Mechanical Engineers, *Conference proceedings: 10th IEEE/ASME International Conference on Mechatronic and Embedded Systems and Applications: September 10-12, 2014, Hotel Duchi della Rovere, Senigallia, Ancona, Italy*.
- [34] G. Welch and G. Bishop, "An Introduction to the Kalman Filter." [Online]. Available: <http://www.cs.unc.edu/~gb>
- [35] "MTw_Awinda_User_Manual".
- [36] "This is information on a product in full production," 2019. [Online]. Available: www.st.com
- [37] "muse_v3_user_manual_v1.6".
- [38] "This is information on a product in full production," 2019. [Online]. Available: www.st.com
- [39] "Modifications reserved |Data subject to change without notice | Printed in Germany BMP390L-Datasheet Digital pressure sensor," 2020.
- [40] F. Salis *et al.*, "A wearable multi-sensor system for real world gait analysis," in *Proceedings of the Annual International Conference of the IEEE Engineering in Medicine and Biology Society, EMBS*, Institute of Electrical and Electronics Engineers Inc., 2021, pp. 7020–7023. doi: 10.1109/EMBC46164.2021.9630392.
- [41] G. Shieh, "Optimal sample sizes for the design of reliability studies: Power consideration," *Behav Res Methods*, vol. 46, no. 3, pp. 772–785, 2014, doi: 10.3758/s13428-013-0396-0.

- [42] R. G. Valenti, I. Dryanovski, and J. Xiao, "Keeping a good attitude: A quaternion-based orientation filter for IMUs and MARGs," *Sensors (Switzerland)*, vol. 15, no. 8, pp. 19302–19330, Aug. 2015, doi: 10.3390/s150819302.
- [43] "https://stayfitwithanand.medium.com/base-of-support-bos-in-physiotherapy-724af2646cae."
- [44] "https://www.workoutsprograms.com/exercises/assisted-sit-to-stand."
- [45] B. K. Shukla, H. Jain, S. Singh, V. Vijay, S. K. Yadav, and D. J. Hewson, "Development of an Instrumented Chair to Identify the Phases of the Sit-to-Stand Movement," in *IFMBE Proceedings*, Springer Science and Business Media Deutschland GmbH, 2021, pp. 382–390. doi: 10.1007/978-3-030-64610-3_44.
- [46] "https://neurotoolkit.com/tug/."
- [47] V. Richard, "Multi-body optimization method for the estimation of joint kinematics: prospects of improvement." [Online]. Available: <https://www.researchgate.net/publication/307866702>
- [48] S. L. Colyer, M. Evans, D. P. Cosker, and A. I. T. Salo, "A Review of the Evolution of Vision-Based Motion Analysis and the Integration of Advanced Computer Vision Methods Towards Developing a Markerless System," *Sports Medicine - Open*, vol. 4, no. 1. Springer, Dec. 01, 2018. doi: 10.1186/s40798-018-0139-y.
- [49] M. Y. H. O. K. H. Takeshi Yamaguchi, "Kinematics of center of mass and center of pressure predict friction requirement at shoe–floor interface during walking," *Gait Posture*, vol. 38, no. 2, pp. 209–214, 2013.
- [50] "https://impararelafisica.altervista.org/legge-delle-velocita-di-un-oscillatore-armonico/."
- [51] "https://www.leveldevelopments.com/2020/10/what-are-inclinometers/mems-accelerometer/."
- [52] "https://pic-microcontroller.com/st-has-mems-gyro-for-more-than/."
- [53] A. O. R. N. A. S. B. D. P. S. Kumar, "Design and Simulation of MEMS Silicon Piezoresistive Pressure Sensor for Barometric Applications," *Engineering, Physics*, 2014.
- [54] N. N. Ahmadzadeh Khosroshahi, J. Karamdel, and N. Ahmadzadeh khosroshahi, "Simulation and Analysis different Mems Pressure Sensor uses Comsol Multiphysics 5.2," 2016. [Online]. Available: <https://www.researchgate.net/publication/309549391>